UNIVERSITY OF CYPRUS

DEPARTMENT OF MECHANICAL
AND MANUFACTURING ENGINEERING

CONTINUOUS STRUCTURAL HEALTH MONITORING UNDER VARYING ENVIRONMENTAL AND OPERATIONAL CONDITIONS USING WAVELET TRANSFORM MODULUS MAXIMA DECAY LINES SIMILARITY

ANDREAS TJIRKALLIS

A Dissertation submitted to the University of Cyprus in partial fulfillment
of the requirements for the degree of Doctor of Philosophy

December, 2013

VALIDATION PAGE

Doctoral Candidate: Andreas Tjirkallis

Doctoral Thesis Title: Continuous Structural Health Monitoring under Varying Environmental and Operational Conditions using Wavelet Transform Modulus Maxima Decay Lines Similarity

The present Doctoral Dissertation was submitted in partial fulfilment of the requirements for the degree of Doctor of Philosophy at the Department of Mechanical and Manufacturing Engineering and was approved on the 2^{nd} of December 2013 by the members of the Examination Committee.

Examination Committe:

Research supervisor: Dr. Andreas Kyprianou .....

Other Members:
Dr. Loucas S. Louca (Chairman) .....
Dr. Luis Eduardo Mujica
Professor Panos Papanastasiou
Professor Charalambos Doumanides

DECLARATION OF DOCTORAL CANDIDATE

The present doctoral dissertation was submitted in partial fulfillment of the requirements for the degree of Doctor of Philosophy of the University of Cyprus. It is a product of original work of my own, unless otherwise mentioned through references, notes, or any other statements.

Andreas Tjirkallis

.....

CONTINUOUS STRUCTURAL HEALTH MONITORING UNDER VARYING ENVIRONMENTAL AND OPERATIONAL CONDITIONS USING WAVELET TRANSFORM MODULUS MAXIMA DECAY LINES SIMILARITY

Andreas Tjirkallis
University of Cyprus, 2013

Over the last three decades, there have been increasing demands to develop and deploy Structural Health Monitoring system for engineering structures. However, in reality, structures are subjected to varying environmental and operational conditions, which cause significant changes in their properties, and thus need to be accounted for in the monitoring system. A number of methods exist in the literature using base line model data to remove the effects of environmental and operational conditions, referred to as $normalization$. A novel Structural Health Monitoring methodology under varying environmental and operational conditions is proposed in this thesis. The methodology is based on the similarity between maxima decay lines of the continuous wavelet transform scalogram of the structural responses obtained under different operational and environmental conditions. This similarity is measured using the magnitude of the Normalized Cross Correlation (NCC). If a decision about damage existence cannot be made from the similarity between the Wavelet Transform Modulus Maxima (WTMM) decay lines, a method based on the Difference of the Pointwise Summation of Similar WTMM decay lines, abbreviated by $DSSD$, is proposed. This enables the identification of changes in the WTMM decay lines due to the presence of damage, to changes due to different force realisation and/or varying operational conditions. The effectiveness of the proposed methodology is demonstrated using both a simulated 3-DOF system and an experimental cantilever beam. Environmental conditions are changed by varying the temperature, and operational conditions by changing the colour of the excitation force, between pink and white, as well as by changing their realisations. The proposed

methodology is made robust, able to be used under any operating and environmental conditions, recording simultaneously the time responses at a large number of points along the length of the structure under consideration, using image acquisition and processing.

Andreas Tjirkallis – University of Cyprus, 2013

ΣΥΝΕΧΗΣ ΠΑΡΑΚΟΛΟΥΘΗΣΗ ΤΗΣ ΛΕΙΤΟΥΡΓΙΚΗΣ ΚΑΤΑΣΤΑΣΗΣ ΣΥΣΤΗΜΑΤΩΝ ΠΟΥ ΥΠΟΚΕΙΝΤΑΙ ΣΕ ΜΕΤΑΒΑΛΛΟΜΕΝΕΣ ΠΕΡΙΒΑΛΛΟΝΤΙΚΕΣ ΚΑΙ ΛΕΙΤΟΥΡΓΙΚΕΣ ΣΥΝΘΗΚΕΣ, ΜΕΤΡΩΝΤΑΣ ΤΗΝ ΟΜΟΙΟΤΗΤΑ ΤΩΝ ΓΡΑΜΜΩΝ ΠΟΥ ΦΕΡΟΥΝ ΤΑ ΜΕΓΙΣΤΑ ΤΟΥ ΣΥΝΕΧΟΥΣ ΜΕΤΑΣΧΗΜΑΤΙΣΜΟΥ ΚΥΜΑΤΙΔΙΩΝ

Ανδρέας Τζιρκαλλής
Πανεπιστήμιο Κύπρου, 2013

Κατά τη διάρκεια των τελευταίων τριών δεκαετιών, έχουν αυξηθεί οι απαιτήσεις για την ανάπτυξη και χρήση συστημάτων παρακολούθησης ομαλής λειτουργίας διαφόρων μηχανολογικών συστημάτων και κατασκευών. Στην πραγματικότητα όμως, οι περιβαλλοντικές και συνθήκες λειτουργίας τους αλλάζουν συνεχώς. Τέτοιες αλλαγές προκαλούν σημαντικές αλλαγές στις ιδιότητές τους, και συνεπώς πρέπει να λαμβάνονται υπόψη. Στη βιβλιογραφία αναφέρονται διάφοροι μέθοδοι, που χρησιμοποιήθηκαν σε συστήματα παρακολούθησης, αφαίρεσης της επίδρασης στην κανονική λειτουργία που προκαλούν οι περιβαλλοντικές και λειτουργικές μεταβολές.. Η διατριβή αυτή αφενός προτείνει μια νέα μεθοδολογία αφαίρεσης των ανωτέρων επιδράσεων και αφετέρου την χρησιμοποιεί για να αναπτύξει ένα σύστημα παρακολούθησης της ομαλής λειτουργίας μηχανολογικών κατασκευών. Η μεθοδολογία βασίζεται στην ομοιότητα των γραμμών που φέρουν τα μέγιστα του συνεχούς μετασχηματισμού κυματιδίων (WTMM). Αυτή η ομοιότητα μετριέται χρησιμοποιώντας το μέτρο της κανονικοποιημένης συσχέτισης (NCC). Εάν μια απόφαση σχετικά με την ύπαρξη αστοχίας δεν δύναται να ληφθεί απευθείας με τη χρήση της ομοιότητας των γραμμών που φέρουν τα μέγιστα συνεχούς μετασχηματισμού κυματιδίων, προτείνεται η χρήση μιας μεθόδου βασισμένη στη διαφορά μεταξύ των σημειακών αθροισμάτων μεταξύ δύο γραμμών που φέρουν τα μέγιστα του συνεχούς μετασχηματισμού κυματιδίων, που αναφέρεται σε συντομία ως (DSSD). Αυτό επιτρέπει τον προσδιορισμό των αλλαγών στις γραμμές που φέρουν τα μέγιστα συνεχούς μετασχηματισμού κυματιδίων λόγω παρουσίας αστοχιών σε σχέση με τις αλλαγές που οφείλονται στη μεταβολή των περιβαλλοντικών ή/και λειτουργικών συνθηκών. Η αποτελεσματικότητα της προτεινόμενης μεθοδολογίας αναδεικνύεται χρησιμοποιώντας διέγερσης. Με την καταγραφή και επεξεργασία εικόνων, διαδικασία η οποία επιτρέπει την καταγραφή της μετατόπισης της κατασκευής σε μεγάλο αριθμό σημείων κατά μήκους της κατασκευής, η μεθοδολογία αποδεικνύεται εύχρηστη και κατάλληλη για χρήση κάτω από οποιεσδήποτε λειτουργικές και περιβαλλοντικές συνθήκες.

ACKNOWLEDGEMENTS

The author would like to express his gratitude to the Department of Mechanical and Manufacturing Engineering of the University of Cyprus and in particular to the following people :

Dr. Andreas Kyprianou, for the great amount of time, advice, support, patient guidance and supervision throughout all these years I have been working on this research. Dr. Kyprianou, was not only a patient mentor, but also a friend.

Professor Charalambos Doumanides, for his encouragement and advice to begin and keep going on with this research leading to a PhD thesis.

Mr. George Vessiaris, for his assistance in setting up the experimental part of this research.

I would also like to thank my wife Marina, and my two kids George and Antigoni, for their patience and support, as well as my parents for their support and encouragement.

TABLE OF CONTENTS

LIST OF TABLES

LIST OF FIGURES

Abbreviations

$ARMA$	AutoRegressive Moving Average
$ARIMA$	AutoRegressive Integrated Moving Average
CWT	Continuous Wavelet Transform
DIS	Damage Identification Similarity
DLL	Decay Line Length
DOF	Degree Of Freedom
DPS	Damage Possibility Similarity
$DSSD$	Difference of Pointwise Summation of Similar WTMM decay lines
FRF	Frequency Response Function
FPS	Frames Per Second
HE	Holder Exponent
NCC	Normalize Cross Correlation
NDE	Non Destructive Evaluation
NPC	Non-linear Principal Components
ODS	Operating Deflection Shape
PCA	Principal Component Analysis
PSD	Power Spectrum Density
SDS	Successive WTMM Decay line Similarity
SHM	Structural Health Monitoring
$SLDV$	Laser Doppler Vibrometer
$STFT$	Short Time Fourier Transform
STV	Similarity Threshold Value
WT	Wavelet Transform
$WTMM$	Wavelet Transform Modulus Maxima

Chapter 1

Introduction

Many vibrating structures need frequent monitoring in order to identify the presence of damages/cracks, which above a certain level may present a serious threat to their performance. Structural Health Monitoring (SHM) methods allowing the early detection and localisation of damages have been intensively investigated over the last three decades. A crack in a structure introduces local flexibilities and changes its dynamic characteristics. Thus the existence, location and size of a crack can be determined from the change of structural dynamic characteristics [1].

Over the last three decades, there have been increasing demands to develop and deploy Damage Detection monitoring systems for engineering structures operating under hazardous conditions. Thus as stated in [2], for long-term SHM of aging aircraft, civil structures after natural disasters, and mechanical systems under fatigue loading, a non-destructive method is required that can perform quick, accurate and on-site damage inspection of structures. There is a wide variety of Non-Destructive Evaluation (NDE) techniques presently in use, including ultrasonic methods, radiography, dye penetration and eddy current sensing, details of which can be found in [3]. However, in order to provide rapid inspection of large structures with minimal interruption of operations, researchers focus on the development of dynamic based methods for rapid global inspection of large structural systems [1, 2].

In reality, structures are subjected to changing environmental and operational factors, such as temperature and moisture, which cause significant changes in its properties. Changes in natural frequency up to 10 % from environmental or operational variations have been reported in [4]. This implies that changes from environmental effects can be larger than

changes due to significant damage [5]. The removal of the effects of environmental conditions on damage detection algorithms is called *normalization* and it is discussed in [5, 6]. Cross et al. in [7, 8], proposed a new normalization method that is based on cointegration, a concept taken from the field of econometrics. This work relies on the premise that environmental and operational conditions caused structural responses to be non-stationary. This non-stationarity can be eliminated from the responses through cointegration.

Wavelet Analysis, via Continuous Wavelet Transform (CWT), Wavelet Transform Modulus Maxima (WTMM) and their decay lines, is used to process the time responses at specific locations along the structure under consideration. Continuous Wavelet Transform (CWT) allows a very precise analysis of the regularity properties of a signal, determining the points on a signal or on its derivatives that display abrupt changes. Douka et al. in [9], used CWT to determine the location and size of the crack in a beam using the fundamental mode of vibration, while Gentile and Messina in [10], used it to detect damage location and crack size from clean and noisy data. However, as CWT contains a vast amount of redundant information, Wavelet Transform Modulus Maxima (WTMM), which are maxima points of the normalized scalogram representing the wavelet coefficients with respect to time and scale are used to compress the information significantly [11]. Mallat and Hwang in [12], suggested a method for detecting singularities in a signal by examining the evolution of the WTMM across the scales, whereas Hasse and Widjakusuma [13], suggested that these WTMM might be useful for monitoring structural response due to progressively developing damage. These WTMM are large magnitude components, which are present at time points where significant changes in the signal occur. Jumps or singularities in the signal can thus be identified by the presence of WTMM at specific time points in the wavelet map [14]. Wavelet analysis has recently been used to facilitate cointegration in detecting damage detection under varying environmental conditions [15].

In this thesis WTMM decay lines were used to devise a novel SHM method capable of detecting structural damage under varying environmental and/or operational conditions, without the need to measure or know the exact excitation force. The proposed Damage Detection methodology is capable to identify the increasing order / severity of damage in a structure. This enables the setting up of a crack order acceptable limit, called the damage tolerance limit, before the structure under consideration can be classified as dangerous and thus required to be taken out of operation, in order to be repaired or replaced. The

methodology is made robust, able to be used under any operating and environmental conditions, and to record simultaneously the time responses at a large number of points along a structure, by using time response signal measurements acquired using images from a High Speed Camera instead of accelerometers or piezoelectric materials. In addition changes in the environmental conditions might also affect the normal operation of sensors attached on the structure.

1.1 Research Hypothesis

In order to provide an effective SHM methodology, capable to detect the existence of damage under varying environmental and/or operating conditions, use of the similarity of the WTMM decay lines, between successive time ranges of the time response signal is proposed, to eliminate the effects of varying environmental and operational conditions. The research hypothesis is that the change in the WTMM decay lines of a dynamic time response is different due to damage, than due to varying environmental or operational conditions or changes in force realisation.

1.2 Thesis Objectives

The objectives that should be achieved in order to enable the development of an autonomous, effective and robust, continuous monitoring system, which will be able to detect the existence of damage in structures operating under varying environmental and/or operational conditions, without the need to measure or know the exact excitation force are:

(a) the design and development of an efficient and reliable data analysis procedure based on Wavelet Transform Modulus Maxima decay line similarity, capable of rejecting environmental and/or operational variability imposed on the structure under consideration.

(b) the development of a method of quantifying the changes in Wavelet Transform Modulus Maxima decay line between time ranges due to varying enviromental conditions, changes in forcing conditions and/or force realisation and damage.

(c) the empedding of the developed method in a Damage Detection Methodology.

(d) the testing and verification of the effectiveness of the proposed methodology using both a simulated and an experimental system.

1.3 Thesis Overview

This dissertation is organised in eight chapters. The research activities accomplished in developing the proposed continuous damage detection methodology which will be able to detect the existence of damage in structures under varying environmental and/or operating conditions, without the need to measure or know the exact excitation force, are described in this thesis, which is overviewed in this section.

Chapter 2 discusses the literature on Damage classification and Structural Health Monitoring (SHM) methodology, as well as the effects of varying enviromental and operational conditions. The relevant literature on vibration testing as well as a description of a typical experimental procedure is provided. Modal and signal based damage detection methods are also described briefly in this chapter.

$Normalization$ techniques used to eliminate the effects of non-stationarity without using base line models, have motivated the investigation of the effectiveness of Wavelet analysis via Wavelet Transform Modulus Maxima (WTMM) decay lines as a feature extraction technique. This motivation is presented in Chapter 3. In this chapter, the mathematical theory of Fourier Transform, Continuous Wavelet Transform (CWT) and WTMM decay lines is also presented. Besides, in an attempt to investigate further, claims in the literature [7, 8], that environmental and operational conditions caused structural responses to be non-stationary, a motivational example using an AutoRegressive Moving Average (ARMA) and an AutoRegressive Integrated Moving Average (ARIMA) model, which introduces non-stationarity into the time response signals is investigated as well. The optical measurements and image processing procedures, as well as the Wavelet Transform edge detection method employed in obtaining the time response measurements of the experimental procedure are discussed in chapter 4.

Chapter 5 contains an overview of WTMM decay line similarity as a feature extracted in damage identification. The mathematical theory of Normalized Cross Correlation (NCC) and its application in determining the similarity between WTMM decay lines between successive time ranges is presented, while its effectiveness is demonstrated on the ARMA and ARIMA model motivational example. The principle of the Difference of the Pointwise Summation of Similar WTMM decay lines, abbreviated by $DSSD$, to compute the distance between the maximum in length WTMM decay line in different time ranges with a reference

one in cases where a decision about damage existence cannot be made from the similarity between the WTMM decay lines directly, is also provided in this chapter. In addition it is explained how similarity in WTMM decay lines and the $DSSD$ principle are employed in a proposed Damage Detection Methodology, which enables the detection of the presence of damage from the time response signal of vibrating structures, while at the same time distinguishing the changes in the time response due to damage existence to changes due to environmental and/or operational variability.

The effectiveness of the proposed methodology is demonstrated using both a simulated 3-DOF system and an experimental cantilever beam, the results of which are illustrated in Chapters 6 and 7 respectively. Conclusions and further research work are provided in Chapter 8.

Chapter 2

Damage Classification, Structural Health Monitoring and Vibration Testing

Here damage classification and Structural Health Monitoring (SHM) methodology are discussed. The relevant literature on vibration testing as well as a description of a typical experimental procedure is provided. Emphasis is given on the literature concerning the effects of environmental and operational variability in Structural Health Monitoring. Modal and signal based damage detection methods are also described briefly.

2.1 Damage Classification

Damage can be defined as changes introduced into a system that adversely affects its current or future performance. Damage is not meaningful without a comparison between two different states of the system, one of which is assumed to represent the initial, and often undamaged, state. This principle is used in the study of damage identification in structural and mechanical systems. Therefore, the definition of damage will be limited to changes to the material and/or geometric properties of these systems, including changes to the boundary conditions and system connectivity, which adversely affect the current or future performance of these systems [16].

A crack in a structure introduces local flexibilities and changes the dynamic characteristics of the structure. Thus the existence, location as well as the size of a crack can be determined from the change of the dynamic characteristics of the structure as stated in [1, 17].

In terms of length-scales, all damage begins at the material level. Such damage is referred to as a defect or flaw and is present to some degree in all materials. Under appropriate loading scenarios, the defects or flaws grow and coalesce at various rates to cause component and then system-level damage. The term damage does not necessarily imply a total loss of system functionality, but rather that the system is no longer operating in its optimal manner. As the damage grows, it will reach a point where it affects the system operation to a point that is no longer acceptable to the user. This point is referred to as failure. In terms of time-scales, damage can accumulate incrementally over long periods of time such as that associated with fatigue or corrosion. On relatively shorter time-scales, damage can also result from scheduled discrete events such as aircraft landings and from unscheduled discrete events such as natural phenomena hazards like earthquakes.

2.2 Structural Health Monitoring

Structural Health Monitoring (SHM) is an automated monitoring practice that seeks to assess the healthy state of a system. It is the process of implementing a damage identification strategy for aerospace, civil and mechanical engineering structures. In this aspect, damage is defined as changes to the material and/or geometric properties of these systems, including changes to the boundary conditions and system connectivity, which adversely affect the performance of the system.

Qualitative and non-continuous methods have long been used to evaluate structures for their capacity to serve their intended purpose. Since the beginning of the 19^{th} century, railroad wheel-tappers have used the sound of a hammer striking the train wheel to evaluate if damage was present [16]. In rotating machinery, vibration monitoring has been used for decades as a performance evaluation technique [18]. Over the last thirty years, there have been increasing demands to develop and deploy SHM systems on various aerospace, civil and mechanical systems. These demands are driven by the tremendous economical and life-safety benefits that such technologies have the potential to provide.

In certain conditions, the use of classical vibration testing methods is either very difficult or impossible, for example when a structure is tested under hazardous conditions, such as operating under atmospheric, hydrologic and geologic phenomena that have the potential to

effect the structure and its activities, or operating at elevated temperatures. Thus for long-term SHM of aging aircraft, civil structures after natural disasters, and mechanical systems under fatigue loading, a non-destructive method is required that can perform quick, accurate and on-site damage inspection of structures [2].

There is a wide variety of Non-Destructive Evaluation (NDE) techniques presently in use, including ultrasonic methods, radiography, dye penetration and eddy current sensing [3]. However, using such conventional NDE techniques to inspect large structures is a costly and time-consuming process. To provide rapid inspection of large structures with minimal interruption of operations, global on-site inspection methods are needed. Thus researchers focus on the development of dynamic based methods for rapid global inspection of large structural systems [1, 2].

SHM Research can be categorized into four levels: (1) detecting the existence of damages, (2) finding the position/location of damage, (3) estimating the extent of damage, and (4) predicting the remaining fatigue life [1].

Furthermore, SHM can be categorized into Destructive and Non-Destructive Methods, whereas Non-Destructive Evaluation (NDE) of structures can be performed using two groups of techniques, called global and local. The SHM Damage Detection categories are summarised in figure 1.

The technique in the group $local$ can provide details about damage in a small area during each measurement. However, this requires long and expensive inspection time, as well as a skilled technician. These methods include ultrasonic methods, magnetic flux leakage inspection, radiography, dye penetration and eddy current sensing [19]. It should also be noted that these conventional NDE techniques usually require the structure under examination to be out of service during the damage inspection procedure.

The technique in the group $global$ contain methods that can provide faster inspection of large structures compared to the $local$ techniques. The dynamic-based methods are global techniques, divided into four groups: (1) spatial-domain methods, where damage locations are detected and found using changes of mass, damping and stiffness matrices, (2) modal-domain methods, where damage is detected by changes in natural frequencies (eigenvalues), modal damping ratios, and mode shapes (eigenvectors), (3) time-domain methods, where damage is detected by the change of the relationship between input and output time signals,

and (4) frequency-domain methods, where damage is detected using changes in frequency response functions (FRFs).

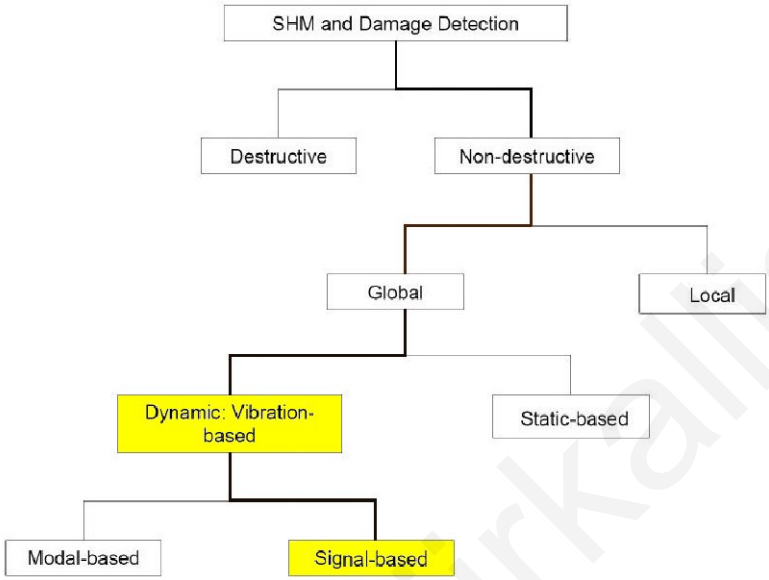

Figure 1: SHM-Damage Detection Categories

2.3 Effects of Environmental and Operational Variability in Structural Health Monitoring

As stated in the introduction, in real life, structures are subjected to varying enviromental and operational conditions, such as temperature and moisture, which cause significant changes in their properties, and thus have to be taken into consideration or eliminated in an effective Structural Health Monitoring System. The removal of the effects of environmental conditions is referred to as $normalization$ and occurs in the context of: (a) availability of information that characterizes the environmental or operational conditions, usually through measurements of relevant variables such as temperature and excitation levels, (b) non-availability of measurements relating to environmental or operational conditions, and (c) defining and extracting damage detecting features that are insensitive to operational and environmental conditions but sensitive to damage. Under (a) and (b) damage detection algorithms based their outcome on comparisons between features characterizing the behavior of an undamaged structure in varying environmental and operational conditions and similar features extracted from structures, possibly damaged, operating in similar conditions. Features that characterize the behavior of an undamaged structure in varying environmental

and operational conditions are known in the literature as base line models simply because they capture the relationship between the environmental and operational variability and the variability of the behavior of the undamaged structure. Base line models are not necessary for damage detection algorithms operating under situation (c).

A review on the effects of environmental and operational conditions on the dynamics of structures is given in [5], where an outline of the normalization methodologies that had been developed up to 2007 is also given. In particular, it discusses regression analysis, subspace-based identification methodologies and novelty detection as methodologies implemented under situation (a), singular value decomposition, auto-associative neural network and factor analysis under situation (b), and novelty detection and Lamb wave propagation under situation (c). Further detailed technical analysis related to the above methodologies can be found both in [5] and the references therein.

Subsequently, a factor analysis based methodology of removing the effects of temperature variations has been developed in the context of situation (a) [20]. The damage detection was based on the following extracted features: eigenproperties computed using a stochastic subspace identification methodology and peak indicators on the Fourier transforms of modal filters. In [21] removal of monitored temperature effect on damage detection is demonstrated that it employs as a damage detection indicator the difference between the actual frequency response function values at various locations of the structure under study and the values obtained by interpolating the frequency response functions at the same locations. This difference is called interpolation error and it is hypothesized that the probability distribution of this error is drastically changed only by the presence of damage. This led to a statistical hypothesis test on the error's mean value which for simulated low noise level rejects the effects of temperature variations.

In context of normalization under situation (b), it was proposed in [22], as an extension of earlier work on associative neural network [5], to use unsupervised support vector machines to extract non-linear principal components, NPCs, of coefficients of fitted autoregressive with exogenous inputs models, AR-ARX, of a structure subjected to excitation at different levels. The NPCs establish the correlations between the coefficients of the fitted models and the variations of the operational conditions which were assumed unmeasured. The same methodology has also been applied to normalize impedance measurements [23]. A different approach on novelty detection and data normalization that mimics the process

of the immune system that discriminates between self and non self cells was investigated in [24].

An alternative way of establishing data normalization by using multivariate autoregressive base line model on embedded delay vectors was proposed in [25]. The damage detection was implemented through a hypothesis test that was testing the predictive ability of the model. For the univariate embedding it was demonstrated that operational and environmental variations which do not induce non-linearities since their effect on the geometry that the trajectories create in the system's state space are significant.

A reference-free damage detection methodology, i.e. a methodology that does not depend on previously obtained base line data has been proposed in [26] and extended further in [27, 28]. This new methodology exploits the interaction of Lamb waves both with cracks and piezoelectric sensors that are strategically positioned on plates that contain cracks. This technique has also been exploited to develop a reference-free methodology of crack detection using impedance measurements [29].

2.4 Vibration Testing

Vibration tests are widely performed as part of the design and development procedure of almost all engineering structures. In practice modal tests are employed to identify natural frequencies, damping ratios and modeshapes of structures [30]. In order to be able to measure the signals of the responses and excitation forces of a vibrating structure, suitable transducers (i.e. accelerometers, force transducers and strain gauges), attached to the structure, are required.

In a typical experimental procedure, a Cantilever beam is forced to vibrate under an external force applied from an electrodynamic exciter, as can be seen in the schematic of figure 2. A Load Cell is used to measure the excitation force, whereas the accelerometers are used to measure the acceleration (response) of the beam at the two points that are attached.

However, the attachment of transducers on a structure under investigation may not always be desirable, while in some cases it can be impossible. For example, the structure under consideration might be rotating at high speeds, or operating under hazardous conditions and/or at elevated temperatures. It is also extremely difficult if not impossible to use transducers when the structure under investigation is of small scale (i.e. a size of a few

millimeters), or when the time responses at a number of points (i.e at 20 different positions) along the structure are required to be measured simultaneously.

To avoid this problem a number of non-contact measuring devices such as resonant ultrasound [31], microwave and radar interferometry [32, 33] or optical devices such as laser displacement probes and laser doppler vibrometers [34, 35] are used. However, these devices provide single location measurements, while in the case of the laser doppler vibrometer automatic sequential measurement using a scanning facility is achieved. This has the disadvantage of limiting the measurements to the number of channels of the measurement system. In this thesis, optical measurement is used as an alternative technique that can provide global measurements.

Optical measurements, but on celluloid films, have been used, as early as the 1930's, in the automotive industry in collecting the trajectories of a number of locations on cars. However, over the last two decades, digital high-speed video system has become an affordable and a more powerful measurement tool, enabling global simultaneous measurements. This technique has been used by Patsias and Staszweski in [36] as a measurement technique in detecting damages in a cantilever beam, while Helfrick et al. in [37], used a pair of digital cameras along with a stroboscope to make full-field measurements of the displacement of rotating blades. More on optical measurements can be found in section 4.3.

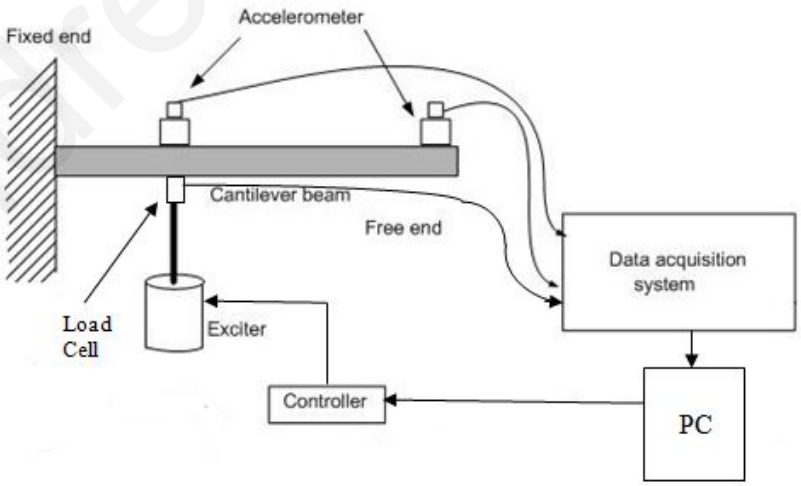

Figure 2: Schematic of a typical cantilever beam vibrating under the application of an external force with a typical acquisition system

2.5 Modal-based damage detection methods

An important step in SHM is the choice of the appropriate feature for damage detection purposes. The most widely used features in the literature are either modal-based or signal-based, which as illustrated in figure 1 belong to the global, vibration-based category. Mode shape and Operational Deflection Shape analysis are briefly explained in this section.

2.5.1 Mode Shape Analysis

The technique used for obtaining mode shapes from measured data is called modal analysis. Modes are inherent properties of a structure, determined by the material properties (mass, damping, and stiffness), as well as by the boundary conditions of the structure. A non-symmetric structure with N degrees of freedom will have N corresponding mode shapes. Each mode shape is an independent and normalized displacement pattern which may be amplified and superimposed to create a resultant displacement pattern. Each mode is defined by a natural resonant frequency, modal damping, and a mode shape. Thus if either the material properties or the boundary conditions of a structure change, its modes change.

Modal analysis relies on two important assumptions: linearity and time invariance of the structure. Modal parameter knowledge can serve various purposes such as structural modification [38], assessment of structural integrity and reliability [39], and Structural Health Monitoring [40]. Most of the early work on mode shape analysis considers the Modal Assurance Criterion (MAC) to compare measured and possibly damaged modes, with undamaged or numerical ones, which are used as a baseline reference [41].

Modal parameters can be obtained either theoretically or experimentally. In theoretical modal analysis, the structural matrices (stiffness **K**, mass **M** and damping **C** matrices) are considered as known, resulting in an eigenvalue problem. In experimental modal analysis, the system response is exploited, and modal analysis identification techniques are applied for the computation of the modal parameters. More details about experimental modal analysis can be found in [30].

Mode shape changes are found to be quite sensitive to damage, especially when higher modes are considered, and thus can be used to provide damage identification information. The problem associated with mode shape monitoring is the need of sufficient spatial measurement resolution, which complicate the experimental procedures, requiring simultaneous

measurements of a large number of accelerometers which must be attached all over the structure that is to be monitored. However, the required measurement resolution can be achieved through the use of either a Scanning Laser Doppler Vibrometer (SLDV) or a High Speed Camera. The drawback with the use of SLDV is its high cost and the relatively complex setting up of the device for accurately vibration responses, whereas a High Speed Camera offers a more economical method, based on the new technological improvements and with an easier to set up procedure.

2.5.2 Operational Deflection Shape (ODS)

Operational Deflection Shape (ODS) testing is a technique that can be applied to examine the operating behavior of a structure that is the actual behavior of an object subject to vibration under real operating forces, without having to measure these forces. It can be considered as a natural way in determining the vibration pattern of structures under given operating conditions. A shape is the motion of one point relative to all others. Motion is a vector quantity, thus it has location and direction associated with it. This is also called a Degree of Freedom (DOF).

An ODS is the summation of all the mode shapes of a vibrating structure and can be defined as any forced motion of two or more points on a structure [42]. It can be defined from any forced motion, either at a moment in time, or at a specific frequency. Hence, an ODS can be obtained from different types of time domain responses, be they random, impulsive, or sinusoidal.

The use of ODS to detect damage is extensively investigated over the last few years. It has been employed to predict damage locations in beams and plates [43, 44]. It should be emphasized that ODS cannot be used directly to detect damage locations, thus Pai and Young proposed in [43], a boundary effect detection method for pinpointing locations of damages in beam-like structures, whereas Maio et al. in [44], developed a perturbation function algorithm to predict damage locations. However, the ODS of both intact and damaged structures should be measured in these algorithms, thus requiring baseline data to be recorded and stored for these SHM methods.

2.6 Signal-based damage detection methods

In an attempt to obtain more sensitive damage features that can capture more information from the measured signal-based responses of structures, researchers have proposed over the last three decades, different types of signal-based models. Signal-based analysis can be classified into time or frequency domain analysis.

An example of frequency domain analysis is the use of frequency-wavenumber analysis, employed in Lamb wave SHM, details of which can be found in [45], as well as the use of frequency domain nonlinear Autoregressive models with eXogenous inputs (ARX). Haroon and Adams in [46], used ARX models to identify damage in mechanical systems by capturing the nonlinear nature of the damages.

Autoregressive Moving Average (ARMA) and Autoregressive Integrated Moving Average (ARIMA) models are examples of time-domain techniques. In ARMA modeling, response time histories of structural response are fit and the coefficients and residual errors are can be considered as features, sensitive to damage [47, 48].

Time series models rely on the fact that the values of the acquired response of a structure at any time can be predicted based on a linear combination of its values at a previous time and some random errors. As stated in [49], the analogy behind using time series models for vibration-based damage identification of structures is based on the fact that if a time series model is fitted to vibration response of the structure under investigation, the obtained coefficients and properties of the model can capture the dynamic characteristics of the structure. Any deviation from the obtained model can thus be a sign of change or damage in the structure. Different types of damage features based on time series models have been extracted in order to capture the deviations in the time series models. Fasel et al. in [50], used a combination of Autoregressive (AR) and ARX models in order to extract damage features. Sohn et al. in [51, 52] used a combination of AR-ARX models to extract damage features for damage detection in a patrol boat, obtaining three sets of strain measurement time responses from different operational conditions of the patrol boat. Two of the strain measurements had been obtained under the same intact state of the boat whereas the third set under a damaged state of the boat. A data normalization process was initially performed on the three sets of data, and each of the three sets of normalized strain time responses were divided to two sets of data with equal sizes. The data in the first half of one of the intact data sets was used to

construct an AR-ARX model for the intact condition of the boat. Any deviation from this model can be used as a sign of damage in the boat. The resulting AR-ARX model was then used to predict the data in the second half of the three different data sets. Variances of the residual prediction errors from the different data sets were used as the damage features, and a threshold was determined based on the variance values in the healthy set of data. It was observed that most of the calculated variance values for the third/damaged set of data fell above the critical threshold line, indicating that the constructed model based on the intact state of the structure cannot be used to accurately predict the data set coming from a damage condition of the boat. Sohn and Farrar in [53], used a similar approach to identify damages in an 8 DOF mass-spring system. The acceleration on all the masses was recorded under different levels of random excitations induced by a shaker. Damage was introduced into the system by adding a bumper between two masses, and the presented approach successfully identified the location that the bumper has been installed in the system.

Wavelet Transform can also be used as a time-domain analysis technique. Hou et al. in [54], presented a study on damage identification using wavelet-based approaches. An application of the method in damage detection is presented using both data from a simple mass-spring model simulated under harmonic loading and actual acceleration data obtained from a building during an earthquake event. Robertson et al. in [14], presented a method where the induced nonlinearity in the system due to the presence of damage is used in damage identification. Wavelet Transform was used to determine Holder exponent values as the damage features. This method proved capable in identifying damages that introduces discontinuities in the acceleration responses of dynamic systems.

It should be noted that Wavelet Analysis, the details of which in the context of varying environmental and operational conditions, is provided in the following chapter, has been extensively used for damage detection over the last two decades [54, 55, 56].

Chapter 3

Wavelet theory in the context of varying environmental and operational conditions

One of the novelties proposed in this thesis is the use of WTMM decay lines as features for damage detection in varying environmental and/or operational conditions. The aim of this chapter is to present the mathematical theory of CWT and explain how WTMM decay lines are defined.

3.1 Introductory remarks

In the introduction and in section 2.2 it has been discussed that SHM is an automated monitoring practice that seeks to assess the healthy state of a structure by obtaining useful measurements during its operation. However, as stated in the introduction, in real life, structures are subjected to changing environmental and operational conditions, such as temperature and moisture, which cause significant changes in their properties that could easily mask the effects caused by damage. As a consequence the effects of environmental and/or operational variability must be accounted for in a continuous damage identification method.

A raw measurement is unlikely to be directly useful for damage identification, as these measurements contain too much redundant information difficult to be interpreted. To circumvent this, raw measurements are processed in order to extract features that pertain to the structural condition and assist algorithms in decision making with regards to this condition.

Over the years a number of feature extraction techniques that are based on vibration measurement have been developed, [51, 57]. These techniques were reviewed and discussed thoroughly in section 2.2.

The removal of the effects of varying environmental and/or operational conditions on damage detection algorithm, known as $normalization$ can occur in three categories, as discussed in section 2.3. One of these algorithms, is the extraction of damage detecting features that are insensitive to operational and environmental conditions but sensitive to damage without the need of base line models. In this dissertation, WTMM decay lines are used as features to be extracted from the time response signals of vibrating systems, in an attempt to normalize the acquired signals and thus determine the healthy state of the system.

3.2 Motivation

In the literature, it has been shown, that both the introduction of damage, resulting in changes in the physical parameters of a structure and varying environmental and/or operational conditions induce non-stationarity in the time response signals of vibrating structures. It should be noticed that the statistics of non-stationary time series change with time.

Attempts have been made to eliminate the effects of non-stationarity without using base line models, using techniques such as Principal Component Analysis [58] and cointegration [7, 8, 15]. These $normalization$ techniques motivated the investigation of the effectiveness of Wavelet Analysis via WTMM decay lines as a feature extraction technique, in determining the healthy state of a structure operating under varying environmental and/or operational conditions.

As discussed in [57], cointegration has been developed in the context of nonstationary signals that can be modelled by a unit root process. However, cointegration requires a training set of data from the normal condition of the intact structure. The Johansen procedure [59], was used to linearly combine the extracted features with the aim of creating a stationary residual, eliminating the trends due to environmental and/or operational variability. As stated in [7], if a linear combination of the training data is stationary, the common trends shared by the extracted features, such as induced trends by temperature and operational variability can be eliminated and any other abnormal change, such as the introduction of damage in the structure, should then cause the combination residual to become non-stationary. Thus the stationary residual created from the cointegration procedure can be used as a damage-sensitive feature that is independent of the varying environmental and operational conditions.

In this dissertation, a novel SHM method is proposed, using the similarity of Wavelet Transform Modulus Maxima (WTMM) decay lines. WTMM decay line is considered as a promising and effective feature extraction technique, in eliminating the effects of varying environmental and/or operational variability, and thus enable the identification of damage under real life operating conditions.

In the following sections, the concepts and mathematical background of Continuous Wavelet Transform (CWT), Wavelet Transform Modulus Maxima (WTMM) and their decay lines are presented and discussed. In addition, their application in detecting singularities in signals employed in Structural Health Monitoring processes is presented.

A motivational example that gives the first assessment on how non-stationarity affects WTMM decay lines is also presented. This example is an ARIMA model and it has been chosen because it transforms a stationary time series, generated by a corresponding ARMA model, into non-stationary time series in the simplest possible way.

3.3 The theory of Continuous Wavelet Transform

Wavelet Analysis has been used in the literature over the last three decades in the analysis of data in various domains such as mathematics [60] and science [61], as well as in detecting edges in images [41]. A historical overview of wavelet analysis can be found in [62, 63].

Continuous Wavelet Transform (CWT), appeared in the 1980's, when Grossman and Morlet [64], defined wavelets in the context of quantum physics. It was developed in order to mitigate the limitations that the Fourier Transform faces when it is used to analyse transient local features in a signal. For completeness sake a brief description of the Fourier Transform is given in the following subsection.

3.3.1 Fourier Transform

The Fourier Transform of a time domain signal $x(t)$ is defined by,

$$X(\omega) = \int_{-\infty}^{+\infty} x(t) e^{-j\omega t} dt \tag{1}$$

where ω is the circular frequency in rad/s, j the imaginary unit defined by $j = \sqrt{-1}$, t the time and e the exponential.

$X(\omega)$ is a complex valued representation of $x(t)$ in the frequency domain. At each ω, the norm of $X(\omega)$, $|X(\omega)|$ gives the amplitude of a sinusoid of frequency ω in $x(t)$ whereas the phase gives its phase difference.

The inverse Fourier Transform is defined by,

$$x(t) = \frac{1}{2\pi} \int_{-\infty}^{+\infty} X(\omega) e^{j\omega t} d\omega \tag{2}$$

where it expresses the original time domain signal as a weighted by $X(\omega)$ superposition of cosinusoidal functions $e^{j\omega t}$.

Since the support of each $e^{j\omega t}$ extends from $-\infty$ to $+\infty$ the Fourier Transform is unable to capture features occuring over a finite time period. Historically this had led to the development of the Short-Time Fourier Transform (STFT), which for a signal $x(t)$ is defined by,

$$X(\tau, \omega) = \int_{-\infty}^{+\infty} x(t) w(t-\tau) e^{-j\omega t} dt \tag{3}$$

where $w(t)$ is a window function defined on an interval $-T \leq t \leq 0$. This ensures localization in time. Invoking Parseval's identity $X(\tau, \omega)$ can also be expressed as,

$$X(\tau, \omega) = e^{-j\omega t} \frac{1}{2\pi} \int_{-\infty}^{+\infty} X(\omega) W(v-\omega) e^{-jvt} dv \tag{4}$$

where $W(v)$ is the Fourier Transform of w, $e^{-j\omega t}$ is the modulation obtained due to translation of W by ω. Now if W is well localised in frequency and w in time, $X(\tau, \omega)$ is a local time frequency analysis of $x(t)$. It can be shown that this yields constant resolution.

Equation 3 may be interpreted as a Fourier spectrum of a signal seen through a sliding window $w(t-\tau)$. If a symmetric window $w(t)$ is chosen then τ identifies the center position of the shifted window $w(t-\tau)$. The weighted signal $f(t) \cdot w(t-\tau)$ trends to zero outside a surrounding of τ. Thus τ indicates the approximate time for which the Fourier spectrum of $f(t) \cdot w(t-\tau)$ is valid. The arrangement of spectras corresponding to a linear grid of τ values yield a STFT spectogram.

The time and frequency resolution of a STFT depends on the support of the window. Narrow window gives good time resolution, but poor frequency resolution, whereas wide window gives good frequency resolution, but poor time resolution. Selecting a too wide window results in the smoothening of the signal under consideration, loosing information contained in its features with rapid variations. Thus, an appropriate window should be

chosen. It should be noted that the chosen window remains unchanged during the analysis. This means that the time and frequency resolutions remain constant during the analysis. The Continuous Wavelet Transform of which the mathematical theory is described in the next section was developed as an alternative to STFT, to overcome the problem of constant resolution.

3.3.2 Continuous Wavelet Transform

The theory of CWT is a well developed and established method of performing multiscale signal analysis [11, 65, 66]. It achieves that by introducing scale in the analysis through the length of the interval over which an analysing function $\psi(t)$, called the mother wavelet, is non-zero. This is similar to the way Fourier transform introduces frequency, ω, in signal analysis through the harmonic functions $e^{i\omega t}$.

The CWT is defined by,

$$Wf(s,u) = \frac{1}{\sqrt{|s|}} \int_{-\infty}^{+\infty} f(t)\psi^*(\frac{t-u}{s})dt \tag{5}$$

where $\psi(t)$ is the mother wavelet, $*$ denotes the complex conjugate, s is the scale parameter and u the translation parameter.

Given that $f(t)$ and $\psi(t)$ belong to the Hilbert space $L^2(R)$, i.e. the space containing the finite energy signals, the CWT is the inner product between $f(t)$ and $\psi_{s,u} = \psi(\frac{t-u}{s})$ and thereby can be denoted by $Wf(s,u) = \langle f(t), \psi_{s,u} \rangle$. The modulus of these products also known as wavelet coefficients, can be plotted over the plane $s \times u$ from where, multiscale features of the analysing signal can be either inferred or further studied.

Typical CWT scalograms using both real and complex gaussian wavelets, of a stationary sine wave are illustrated in figure 3, where the dark areas are areas of high correlation between the sine wave and the scaled version of the real wavelet. In figure 3 (b), where a real wavelet is used, dark bands appear in areas of high correlation separated by white bands, due to a phase mixing problem that is typical with periodic signals. This phase mixing problem in the analysis of periodic signals is avoided by using complex wavelets as in figure 3 (c), which can take into consideration both the amplitude and the phase of the signal.

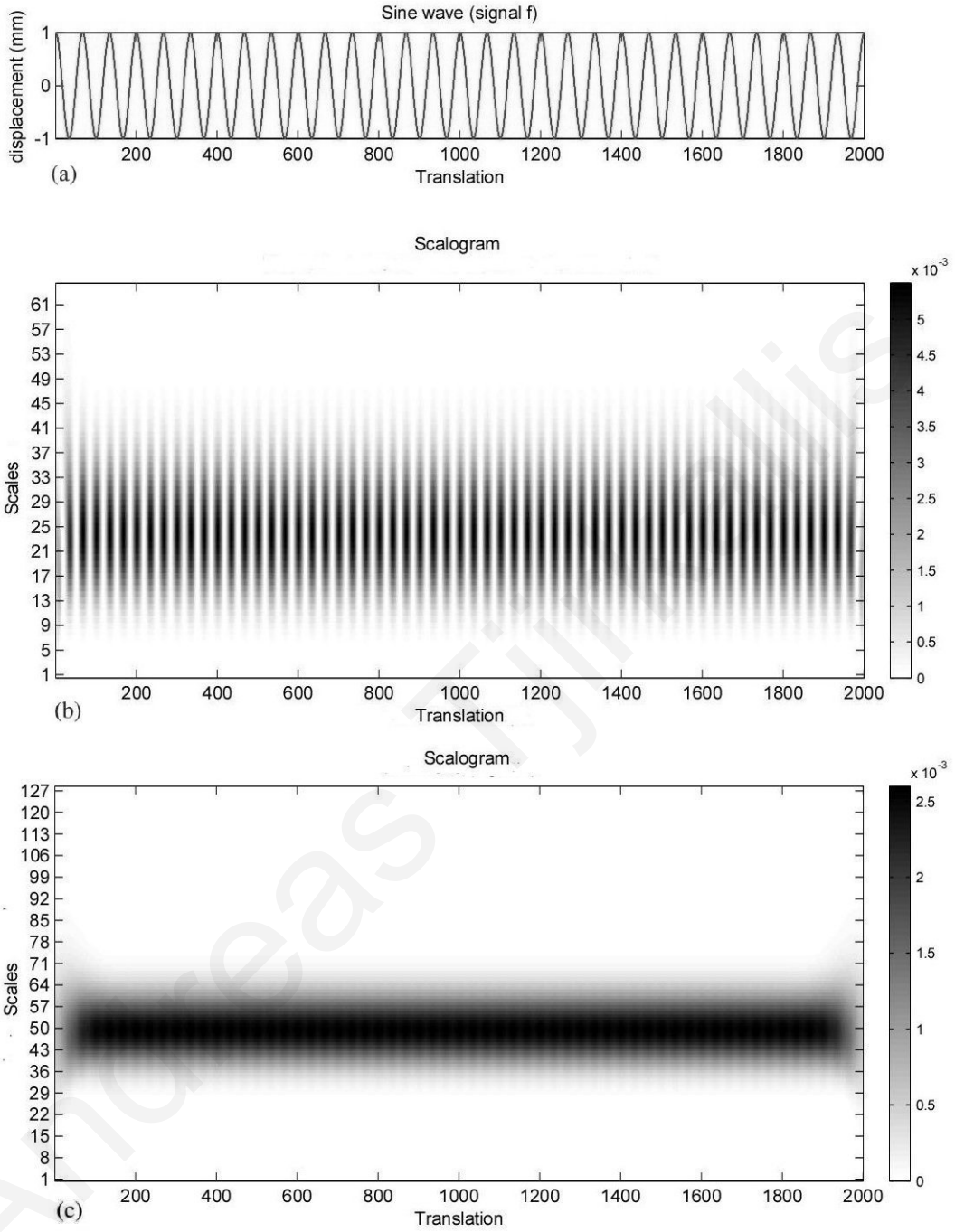

Figure 3: (a) Time response of periodic sine wave, (b) CWT scalogram of the sine wave signal using real 1^{st} order derivative of the gaussian function wavelet and (c) CWT scalogram of the sine wave signal using complex 4^{th} order derivative of the gaussian function wavelet.

The CWT provides a very redundant, but also very finely detailed, description of a signal in terms of both translation and scale. As mentioned in [67], CWTs are particularly helpful in tackling problems involving signal identification and detection of hidden transients.

A wavelet is a waveform of effectively limited duration with an average value of zero, used to analyse a given function or signal at a specified scale. This function plays the role of the window of the STFT, but it has both position and scale. The wavelet can be translated to various positions of the signal, whereas its scale can be adjusted as can be seen in figures 4 and 5 respectively.

Figure 4: Time translation of a given scale of a wavelet

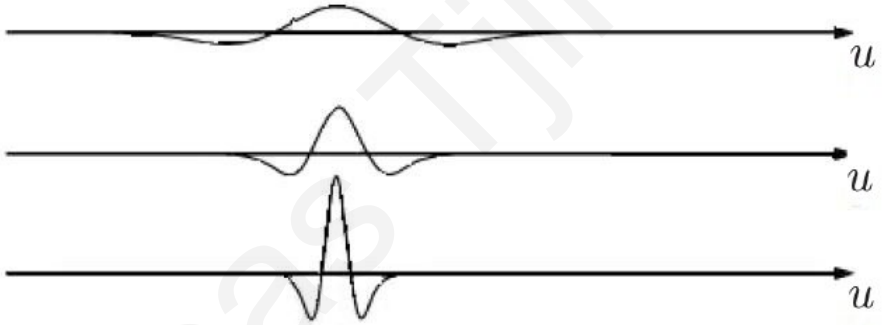

Figure 5: Scale variation of a wavelet at a specified position

A number of different types of wavelet families, such as Daubechies, Gaussian, Haar, Morlet and Symmlet exist, whose qualities vary according to a number of criteria such as: the support of the mother wavelets, the symmetry, the number of vanishing moments and the regularity. The real wavelets constructed from the first and second order derivatives of the Gaussian function can be seen in figure 6, whereas the complex gaussian wavelet of the fourth order derivative can be seen in figure 7. These were generated in Matlab ® [68].

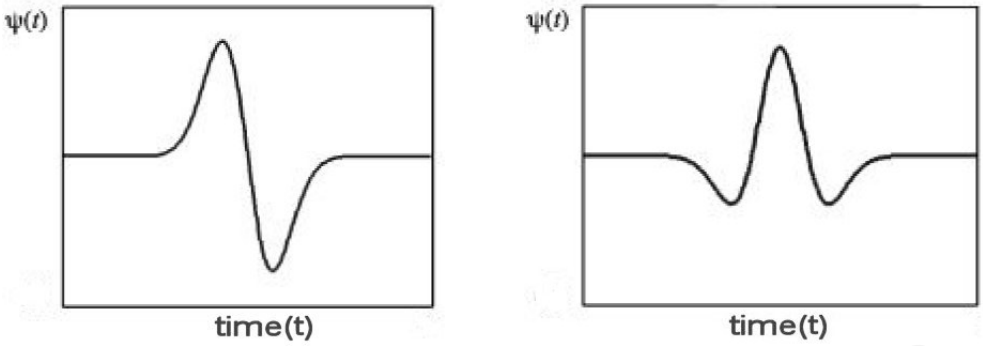

(a) Gaussian 1^{st} order derivative wavelet

(b) Gaussian 2^{nd} order derivative (Mexican hat) wavelet

Figure 6: Waveforms of real gaussian (a) 1^{st} order and (b) 2^{nd} order derivative mother wavelets.

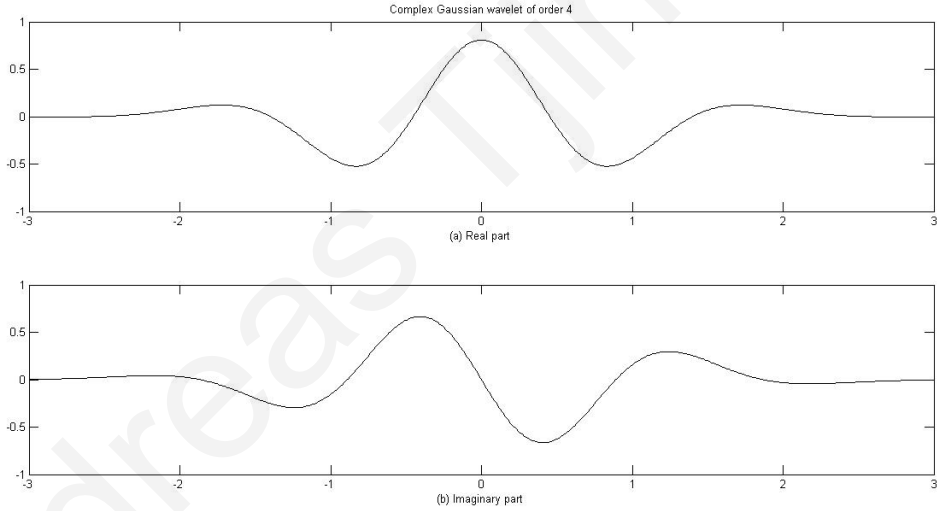

Figure 7: Waveforms of complex gaussian of 4^{th} order derivative (a) real part and (b) imaginary part.

3.4 Lipschitz / Holder Exponent analysis

An important damage-sensitive feature that can be used to detect the presence of damage from dynamic time response signals is the Lipshitz or Holder Exponent.

The Holder Exponent (HE) provides a measure of a signal's regularity, that is, a measure of the number of continuous derivatives that the signal possesses [14]. Thus the HE can be considered as a tool that specifies the order that a function is differentiable. Taking

the derivative of a function decreases its regularity by 1 and integrating increases it by 1. Therefore, if a signal $f(t)$ is differentiable at $t = 0$, it has a Holder exponent of 1, whereas if the signal is discontinuous but bounded in the neighbourhood of $t = 0$, as is a step function, then the exponent is 0.

Measuring the regularity of a signal in time can be used to detect points in the signal that are discontinuous, and are considered as singularities, since bounded discontinuities have Holder exponent of 0. The Holder exponent can be used for global or local regularity of functions.

The HE value can be obtained either through the use of the Fourier Transform or of the Wavelet Transform. However, through the Fourier Transform, only the minimum global regularity of the function can be obtained, whereas through wavelets the Holder regularity both over time intervals and at specific points in time can be obtained. Thus in order to be used effectively in SHM, the HE is obtained through Wavelet Analysis.

It should be pointed out that the ability of a wavelet to suppress a polynomial depends on a mathematical characteristic of the wavelet called its number of vanishing moments. This can be used to measure the local regularity of a signal. A wavelet $\psi(t)$ has p vanishing moments if:

$$\int_{-\infty}^{+\infty} t^k \psi(t) dt = 0 \tag{6}$$

with $0 \leq k \leq p$.

The local regularity of mother wavelets is important as it can be chosen to be equal to the local regularity of the signal to be analysed. More on vanishing moments can be found in [11].

The point-wise Holder regularity of the signal under consideration is determined by calculating the decay of the scalogram at specific points in time across all scales. The Holder exponent that gives the local regularity of a function $f(t)$ approximated locally at point t_0 by a polynomial of the form :

$$f(t) = c_0 + c_1(t - t_0) + ... + c_k(t - t_0)^k + A|t - t_0|^\alpha = P_k(t - t_0) + A|t - t_0|^\alpha \tag{7}$$

where P_k is a polynomial of order k and A a constant coefficient, can be defined as [14] :

$$|f(t) - P_k(t - t_0)| \leq A|t - t_0|^\alpha \tag{8}$$

where the term associated with exponent α can be considered as the residual that remains after fitting a polynomial of order k to the signal, or as the part of the signal that does not

fit into a $k+1$ term approximation. A higher value of α indicates a better regularity or a smoother function.

In order to detect singularities, a wavelet transform that has p vanishing moments must be used, so that is able to ignore polynomial up to order k as given by equation 6.

Transformation of equation 8 using a wavelet with at least k vanishing moments then provides a method for extracting the values of the HE in time by,

$$|Wf(s,u)| \leq Cs^{\alpha} \tag{9}$$

The regularity of the function can be determined by the relationship between the wavelet transform of the function and the error between the polynomial and the function, as the wavelet transform of the polynomial is zero.

The Holder exponent obtained by using the magnitude of the modulus of the wavelet transform, can be calculated at a specific point in time by calculating the slope of the logarithmic of the modulus at that time against the logarithmic of the scale vector. Thus the Holder exponent in the time-domain, is obtained mathematically by taking the logarithmic of both sides of equation 9, from which the gradient α is obtained.

$$log|Wf(s,u)| = log(C) + \alpha log(s) \tag{10}$$

$$\alpha = \frac{log|Wf(s,u)| + log(C)}{log(s)} \tag{11}$$

where, C is due to the offset that can be ignored, thus equation 11 can be simplified as follows:

$$\alpha = \frac{log|Wf(s,u)|}{log(s)} \tag{12}$$

The gradient α as given by equation 12 is the decay of the wavelet modulus across its scales. The Holder exponent is the negative of the slope. The process is repeated for each time point of the wavelet modulus, thus obtaining the HE for all points in time.

CWT is particularly suitable in calculating the Holder exponent, since the HE of a function $f(t)$ at a position u governs the decay of the wavelet coefficients $Wf(s,u)$ across the scales. This variability provides a finer time resolution than the Fourier transform, which is helpful in detecting the point in time that a sudden change - indicating the presence of a singularity - occurs in the signal considered. Wavelets are tuned according to the signals that are being considered, as the order of the wavelet limits the degree of regularity that can be measured in a signal.

For detecting discontinuities in a signal the Holder exponent against time is plotted, and the presence of a distinct downward jump in the plotting indicates the existence of a discontinuity, as can be seen in figure 9 (b) in the sinusoidal wave example. As stated above, a discontinuous point should have a Holder exponent value of zero, but due to resolution limitations of the wavelet transform slightly different values can be seen. Thus a discontinuity in the signal is present at the point in time where the Holder exponent changes from positive values towards zero, or below.

Singularity detection in SHM using the Holder Exponent has been proposed by Hambaba and Huff in [69], Peng et al. in [70], Nguyen et. al in [71], Hong at al. in [72], Robertson et al. [14] and Tjirkallis and Kyprianou in [73].

The effectiveness of both the CWT and the Holder (Lipschitz) exponent in detecting singularities present in time response signals is demonstrated in section 3.6 where the CWT and the HE of a sinusoidal signal in which a singularity has been artificially added in a specific time location is investigated. However it has been observed that the Holder Exponent analysis cannot be used to identify and distinguish singularities that are due to the presence of damage to that due to varying enviromental and/or operational conditions. This creates the need for a methodology of identifying singularities that are due to the variation of environmental or operating conditions. The research endeavors to achieve this had brought to light the possibility that the information about the changes in the singularities incurred due to the above events is carried by the WTMM decay lines. Therefore, one can use a methodology that is relied only on the WTMM decay lines in order to detect the changes in the vibration responses due to changes in environmental and operational conditions. As will be shown in Chapter 5, this methodology is based on Wavelet Transform Modulus Maxima (WTMM) decay line similarity. Results of the usage of the Holder Exponent with the sine wave example with and without the artificial singularity, with the ARMA/ARIMA model as well as with the simulation 3 DOF system based on the principle of the absolute difference of the Holder Exponent between successive time ranges as described by Tjirkallis and Kyprianou in [73], is presented in Appendix C.

Before going on to present the sine wave example, a discussion of the choice of the most appropriate mother wavelet, $\psi(t)$, that enables the identification of singularities in a signal, is presented in the following section.

3.5 Choosing the Appropriate Wavelet

As pointed out in section 3.3.2, a number of different types of wavelet families exist. A fundamental aspect in using Wavelet Transform, is the selection of the appropriate wavelet function, known as the mother wavelet, for each application under consideration in order to obtain effective and optimum results.

When choosing the appropriate mother wavelet for Structural Health Monitoring (SHM) applications, it is important to consider the ability of the chosen wavelet in identifying the existence of singularities in a signal. It can be observed from the literature, that no unique wavelet can be recommended for all SHM applications, and that some mother wavelets might be better used in certain situations than others. For example Ogaja and Rizos in [74], suggested that Haar wavelet is an efficient preprocessing technique for deformation monitoring. Yan et al. demonstrated in [75], that most wavelet functions apart from the Morlet wavelets, were able to detect effectively unbalance forces in flexible rotors based on the vibration responses by combining Wavelet Transform and Artificial Neural Networks.

Hong at al. showed in [72], that the wavelet function that gives the best results of using the Holder exponent with wavelet transform was the second derivative of the Gaussian function, the so-called Mexican Hat. Besides, Mallat stated in [11], that wavelets which are the derivatives of Gaussians are used to guarantee that all maxima lines propagate up to the finest scales and that the chaining together of maxima into maxima lines is also a procedure for removing false modulus maxima arising from numerical errors in regions where the wavelet transform is close to zero. It was observed that an appropriate mother wavelet $\psi(t)$, that enables the identification of singularities in a signal, is the first order derivative of the Gaussian function.

In this dissertation a number of wavelet functions (1st order derivative of the Gaussian, 2nd order derivative of the Gaussian [Mexican Hat], Morlet and Haar) have been tested in obtaining the decay of the WTMM from the CWT of time response signals, and it was observed that the most appropriate mother wavelet, is the first order derivative of the Gaussian function, and thus was the one used in the proposed SHM method, details of which are given in chapter 5.

3.6 Effectiveness of CWT and HE in singularity identification using a sine wave example

A typical sine wave signal with a frequency of 30 Hz and an amplitude of 1 mm, is generated using Matlab ® [68], where at the time location of 0.8 second (at time point 800), an artificial singularity is introduced. The time response and its corresponding CWT scalogram using both real and complex gaussian wavelets, of the signal without the presence of a singularity is shown in figure 3 of section 3.3.2, whereas with the presence of an artificial singularity is shown in figure 9.

The Holder Exponent based on CWT as described in section 3.4, is also obtained for both signals and is displayed in figure 8.

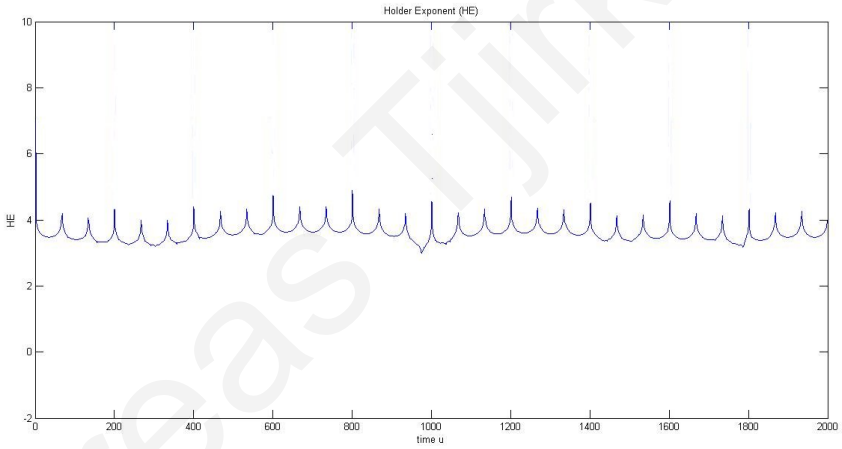

(a) HE of Sine wave signal - NO singularity

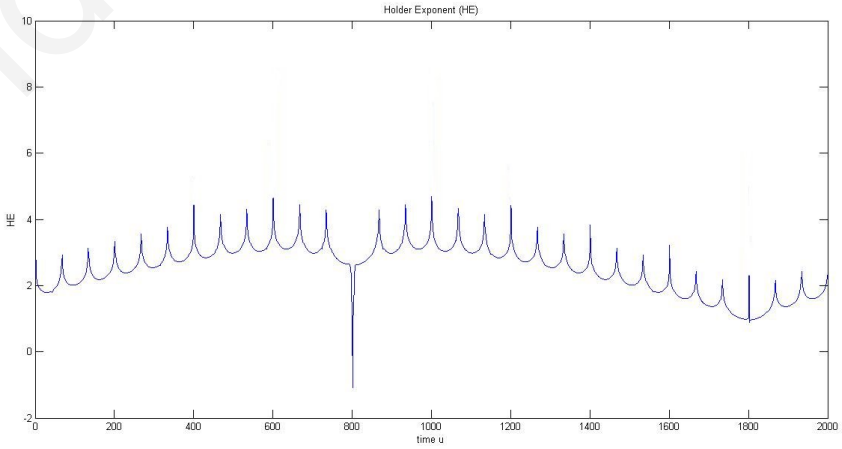

(b) HE of Sine wave signal - singularity

Figure 8: Wavelet Transform Holder Exponent of the Sine wave signal (a) without any singularity and (b) with singularity at time point 800.

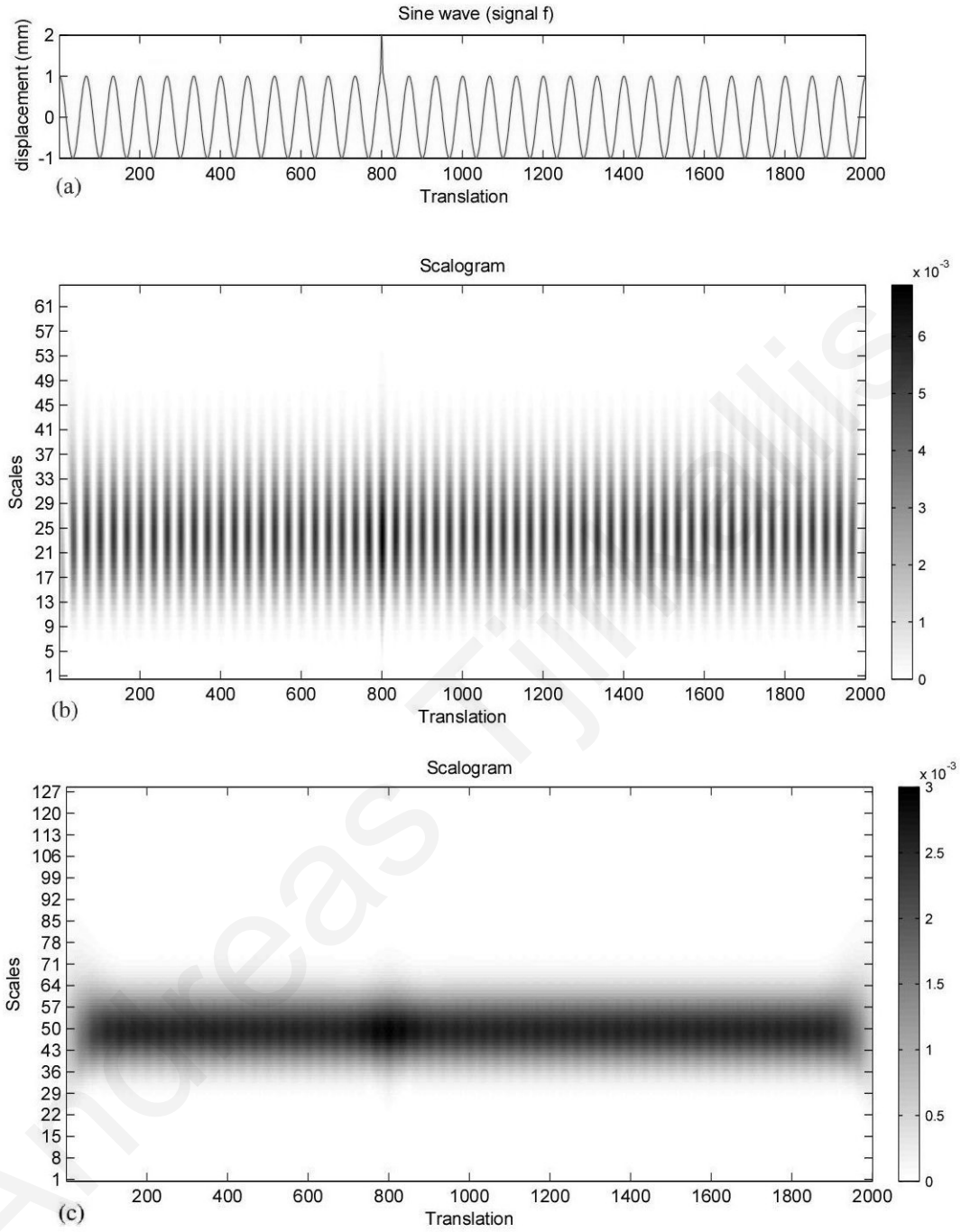

Figure 9: (a) Time response of periodic sine wave with artificial singularity at time point 800, (b) CWT scalogram of the sine wave signal using real 1^{st} order derivative of the gaussian function wavelet and (c) CWT scalogram of the sine wave signal using complex 4^{th} order derivative of the gaussian function wavelet, showing the presence and location of the artificial singularity

From the plots of the CWT scalogram between the sine wave signal without any singularity and with singularity present and especially from that of the Holder Exponent, shown in figures 3, 9 and 8 respectively, it is obvious that the introduction of a singularity in a signal, can be identified. In the first case it is identified by the change in the scalogram darkness, indicating changes in the Coefficient values, which is more obvious in the lower scales, and in the second case, by a sudden drop in the HE signal. However, as it would be pointed out later on, it is almost impossible to identify the occurrence of a singularity in a signal that is due to the presence of damage, to the one which is due to varying environmental and/or operational variability, which are unavoidable in real life operations. Thus a Damage Detection Methodology is necessary to be implemented in order to identify the presence of singularities in signals and hence the presence of damage in a vibrating structure under consideration, while at the same time eliminating the effects on the singularities due to changes in environmental and/or operational conditions. However, before presenting the proposed Damage Detection Methodology in chapter 5, the proposed extraction feature used in damage identification in this dissertation, the WTMM decay lines of the time response signal of a vibrating structure is presented in the following section.

3.7 Wavelet Transform Modulus Maxima (WTMM) and their decay lines

Wavelet Ridges are the maxima points of the normalized scalogram representing the wavelet coefficients with respect to time and scale [11, 76]. Hasse and Widjakusuma in [13], mentioned that fundamental information about structural dynamics is contained in the ridges or maxima lines of the CWT. A *Wavelet Transform Modulus Maxima* (WTMM) line is any connected curve *s(u)* in the scale-space plane *(s, u)* along which all points are modulus maxima [11], and the WTMM are large magnitude components, which are present at time points where the maximum change in the signal has occurred. According to Mallat and Hwang in [12], a local extremum of the wavelet transform $Wf(s,u)$ is any point (u_0, s_0) such that $\frac{\partial Wf(s_0,u_0)}{\partial u}$ has a zero-crossing at $u = u_0$, when u varies. A modulus maximum is any point (u_0, s_0) such that $|Wf(s_0,u)| < |Wf(s_0,u_0)|$ when *u* belongs to either a right or a left neighbourhood of u_0, and $|Wf(s_0,u)| \leq |Wf(s_0,u_0)|$ when u belongs to the other side of the neighbourhood of u_0. A maxima line is thus any connected curve in the scale space (*s, u*) along which all points are modulus maxima.

It should be pointed out, that CWT contains a vast amount of redundant information, whereas Wavelet Transform Modulus Maxima (WTMM), which occur at the points (s_0, u_0) on the translation scale plane that satisfy,

$$\frac{\partial |Wf(s,u)|}{\partial u} = 0 \tag{13}$$

are used to significantly compress the information [11]. Mallat and Hwang in [12], suggested a method for detecting singularities in a signal by examining the evolution of the WTMM across the scales, whereas Hasse and Widjakusuma in [13], suggested that these WTMM might be useful for monitoring structural response due to progressively developing damage. Jumps or singularities in the signal can thus be identified by the presence of WTMM at specific time points in the wavelet map [14].

The decay of a WTMM line allows a very precise analysis of the regularity of a signal at a given point in time, determining the points on a signal or its derivatives that display abrupt changes. Points where large changes occur in the signal, will have large coefficients at all the different scales, thus having little decay. Elements such as noise, show more decay across all of the scales, as they only produce large coefficients in the finer scales. In the context of structural dynamics it has been observed that the decay of maxima lines of a dynamic time response changes due to (i) changes in the forcing conditions and/or force realisation, (ii) changes in the environmental conditions and (iii) damage [73].

It has been also shown by Robertson et al. in [14], that this decay of the WTMM across the scales for each time point offers a less time consuming alternative to the extraction of the maxima lines. The measure of this decay is considered to be the Holder exponent of the signal at a given time point, described in section 3.4.

The WTMM and their corresponding decay lines of the sine wave example given in section 3.6, with NO singularity and with an artificial singularity present at time sample $t = 800$, are shown in figures 10 and 11 respectively.

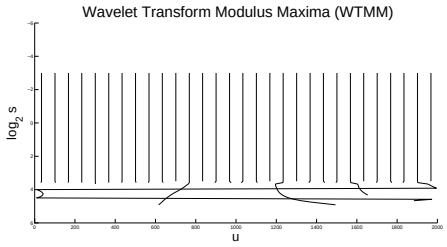

(a) Sine wave signal WTMM - NO singularity

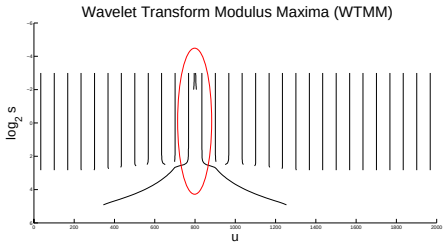

(b) Sine wave signal WTMM - singularity

Figure 10: Wavelet Transform Modulus Maxima of the Sine wave signal (a) without any singularity and (b) with singularity at time point 800.

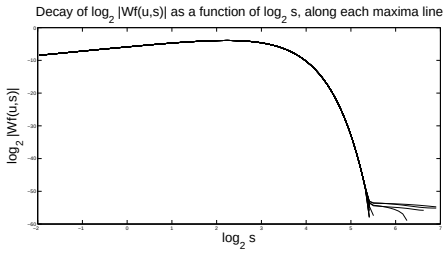

(a) Sine wave signal WTMM decay lines - NO singularity

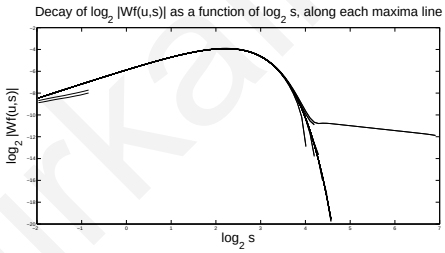

(b) Sine wave signal WTMM decay lines - singularity

Figure 11: WTMM decay lines of the Sine wave signal (a) without any singularity and (b) with singularity at time point 800

As can be seen from the above plots of the WTMM in figure 10, similarly with the Holder Exponent, where there is an abrupt change in the HE at time location location $t = 800$, shown in figure 8, there is a change in the WTMM throughout the whole time range, which is more obvious at and around time location $t = 800$ indicating the presence of singularity.

Additionally the plots of WTMM decay lines shown in figure 11, indicate that there is a change in the WTMM decay lines due to the presence of a singularity in the time range under consideration.

However, as stated earlier, since the presence of singularities can be either due to varying environmental and/or operational conditions or due to the presence of damage, further investigation on the use of WTMM and their decay lines is required in order to enable the identification of damage under conditions of environmental and/or operational variability. This leads to the development of a motivational example using Autoregressive Moving Average (ARMA) and Autoregressive Integrated Moving Average (ARIMA) models. The

ARIMA model transforms a stationary time series generated by an ARMA model to a non-stationary one. This enables the investigation of how the introduction of non-stationarity in a time response signal affects the behaviour of WTMM decay lines.

3.8 ARMA and ARIMA models as motivational example for the behavior of the WTMM decay lines in the presence of non-stationarity

In the literature, that was discussed in section 3.2, the case was made that varying environmental and operational conditions impart non-stationarity to the structural responses. This section carries out an exploratory analysis aiming to assess the effect of non-stationarity on WTMM decay lines. This is done using Autoregressive Moving Average, ARMA, and Autoregressive Integrated Moving Average, ARIMA models, which are widely used to capture the characteristics of homogeneous stationary and non-stationary processes respectively [77].

An ARMA model, of order (p, q) of a random process $y(t)$ is given by,

$$y(t) = \frac{C(T)}{A(T)} e(t) \tag{14}$$

where T is the time lag operator, $A(T)$ is a polynomial in T of order p, called auto regressive polynomial, $C(T)$ a polynomial in T, defined by $Ty(t) = y(t-1)$, of order q, called moving average polynomial and $e(t)$ represents the white noise random process. Equation 14 can be thought as a difference equation representing a system whose input is $e(t)$ and output $y(t)$.

ARIMA captures non-stationary behavior by allowing one or more roots of $A(T)$ to become unity, i.e. $A(T)$ can be factorized into,

$$A(T) = \alpha(T)(1 - T)^d \tag{15}$$

where $\alpha(T)$ is a stationary autoregressive polynomial of order p, and $(1 - T)^d$ represents a unit root of multiplicity d. Now, if $A(T)$ in equation 14 can be factored as in 15 then the model is called ARIMA of order (p, d, q) and is used to model homogeneous non-stationary time series.

In this thesis a time series was generated using Matlab® [68], with coefficient values of $C(T)$ be given by C_1 = [$\frac{1}{3}$, $\frac{1}{3}$, $\frac{1}{3}$], and of $A(T)$ by A_1 = [1, -0.5783, 0.2138] as coefficients of $C(T)$ and $A(T)$ respectively. This is considered as a time series obtained from an intact system in its initial operating conditions. The coefficients of $C(T)$ and $A(T)$ are

varied, simulating the changes in environmental conditions and the introduction of damage respectively.

It is observed that by varying the coefficients of $C(T)$ the number of total WTMM decay lines remain the same. On the other hand by introducing a unit root in A, and hence inducing non-stationarity, the number of total WTMM decay lines reduces significantly.

Plots of the time responses with the corresponding CWT and the WTMM decay lines of the various time series by varying the parameters of the ARMA model can be seen in figure 12. As it can be seen from these plots, it is impossible using the time response of the signal and/or its CWT, to identify changes in the coefficients of $C(T)$ and induced non-stationarity behavior.

The above observations indicate that the WTMM decay lines obtained from the CWT of a time series change by environmental and/or operational variability as well as by the presence of damage in the structure. This implies that the WTMM decay lines seem to be a promising feature to be extracted in identifying the presence of singularities in a time response signal. However, a Damage Detection methodology needs to be adopted that can effectively employ WTMM decay lines in identifying the presence of damage under varying environmental and/or operational conditions. In this thesis, the proposed Damage Detection methodology is based on WTMM decay line similarity and it is presented in chapter 5.

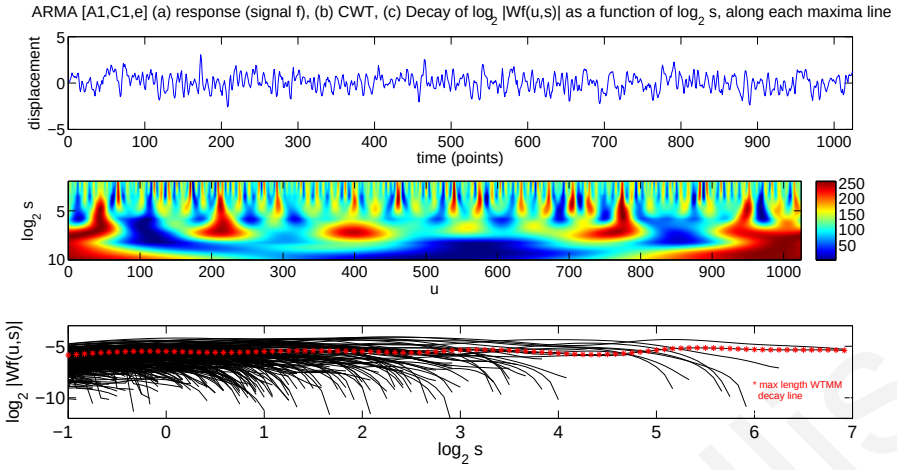

(a) ARMA (a) response C_1, A_1, e_1 , (b) CWT, (c) WTMM decay lines

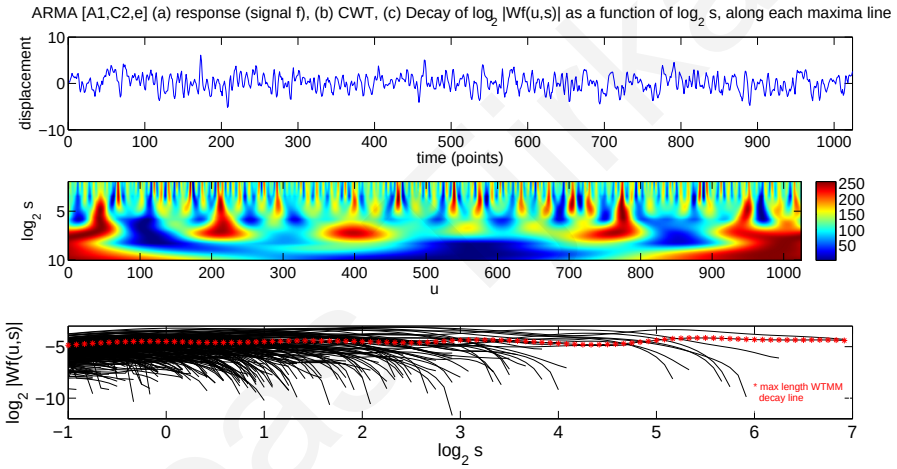

(b) ARMA (a) response C_2, A_1, e_1 , (b) CWT, (c) WTMM decay lines

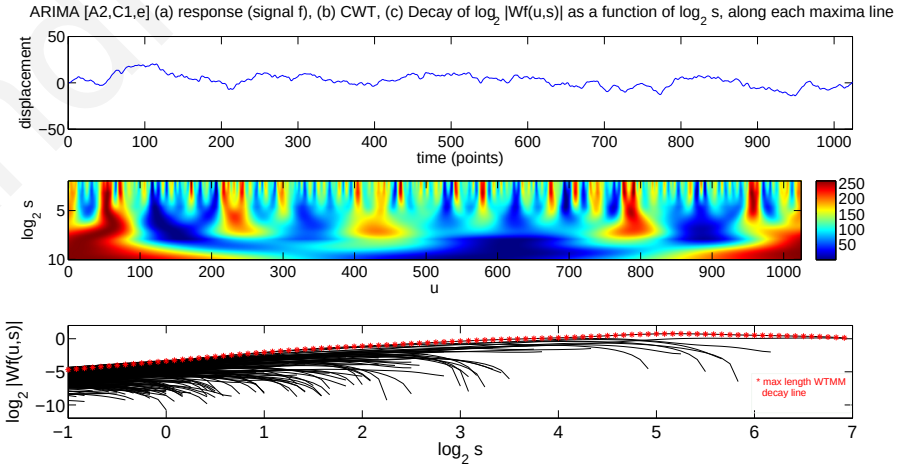

(c) ARMA (a) response C_1, A_2, e_1 , (b) CWT, (c) WTMM decay lines

Figure 12: ARMA and ARIMA time series, CWT and WTMM Decay line plots for varying coefficients of $C(T)$ and $A(T)$, with C_1=[$\frac{1}{3}, \frac{1}{3}, \frac{1}{3}$], C_2=[$\frac{2}{3}, \frac{2}{3}, \frac{2}{3}$], A_1=[1, -0.5783, 0.2138], A_2=[1, -1.2, 0.2138].

Chapter 4

Optical measurement of the vibration responses

In this chapter, the image acquisition and processing as part of the optical measuring process employed in measuring the time domain response of the vibrating experimental cantilever beam using a High Speed camera is presented. The Wavelet Transform edge detection methodology employed in obtaining the contours of the vibrating structure as well as the line tracking algorithm which provides the operational displacement of the structure together with the image sequence analysis providing the time responses along the length of the structure is also given.

4.1 Vibration Measurements

In order for a Structural Health Monitoring Methodology to be effective and robust, it is preferable that only the response of the vibrating structure needs to be measured, and also the measurement to be able to take place with non-contact transducers instead of accelerometers. This will enable the measurement of the response of a structure while operating under hazardous conditions, during motion and/or rotation, as well as under elevated temperatures.

A number of non-contact measuring devices such as eddy current probes that measure displacements and optical devices (laser displacement probes and laser doppler vibrometers) have been used. Details of these measuring devices can be found in the literature [78, 79, 80]. However, all these sensors provide single location measurements, which for laser doppler vibrometer it can be automated via a scanning facility. Thus the measurements

are limited to the number of channels available by the measurement system. In order to provide global measurements, optical methods using a high speed camera are employed. Before moving on to describe optical measurements and the capabilities of an optical measurement system, a summary of image formation and processing in presented in section 4.2.

4.2 Image formation and processing

An image is a representation of the light received by a series of sensors, that are capable of recording that light, and image processing is the manipulation and analysis of images using digital computers [81]. In an optical image of a scene, the light rays from each scene point are focused by the lens at the corresponding image point. The basic equation that describes the production of image locations at different distances from their corresponding scene points is specified by [82],

$$\frac{1}{u} + \frac{1}{v} = \frac{1}{f^*} \tag{16}$$

where, f^* is the focal length of the lens and u and v are the distances of the object and image points from the lens on opposite sides, as it can be seen in figure 13.

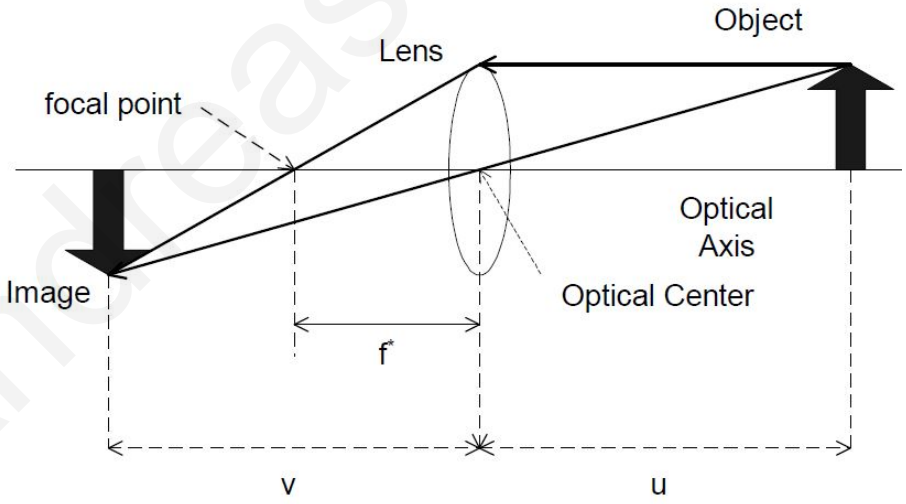

Figure 13: Optical lens Model

The image formation process converts the information of the scene into an illumination pattern in the image plane, which is a function of the coordinates in the plane of the image. As the real world is three-dimensional (3D), the two-dimensional (2D) image carrying information about brightness point, which is called a 2D intensity image, is a result of a projection of the 3D object onto a 2D plane by straight lines passing through a single point.

This projection is called perspective projection and its geometry, where the real world coordinates are related to the image coordinates is illustrated in figure 14, in a model called the pinhole camera model as given by Patsias in [41] and by Sonka et al. in [83].

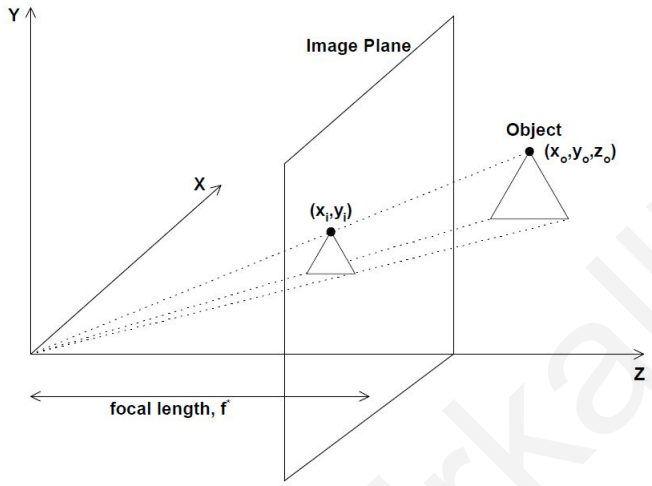

Figure 14: Perspective projection in the pinhole camera model

The image coordinates (x_i, y_i) are related to the object coordinates (x_o, y_o, z_o) using the focal length f^* (the distance of the image plane to the centre of the projection) using expression,

$$x_i = x_0 \frac{f^*}{z_0}, y_i = y_0 \frac{f^*}{z_0} \tag{17}$$

Assuming f^* tends to infinity, the nonlinear perspective projection can be approximated by a linear projection called orthographic. As the transformation is not a one-to-one transformation, some information is lost for objects mapped in the camera plane. The reconstruction of 3D objects from a 2D image is an ill-posed problem [83].

In this thesis, the image processing adopted, is restricted to the use and analysis of 2D images, a restriction which, as stated by Patsias in [41], under certain conditions, is sufficient.

The use of a wide range of image processing techniques is not affected whether or not the object represented in an image is 3D. The only information available in an intensity image is the brightness of the image.

For monochromatic images - which are the ones used in this thesis - the intensity image is described as a function $f(x, y)$, where x and y are the coordinated in the image plane. For multispectral images, the sensor used is sensitive to a number of wavelengths, and the images are represented as $f_1(x, y), f_2(x, y), f_3(x, y)$.

In digital image processing, images are represented by matrices, and thus the image coordinates are integer numbers. The domain of the image function is a subset S of the image plane as described by,

$$S = (x, y) : 0 \leq x \leq x_{max}, 0 \leq y \leq y_{max} \tag{18}$$

where x is the horizontal and y the vertical coordinate of the 2D image plane.

In monochromatic images, the image function values are called gray levels or scales, and are real, non-negative bounded integers. A monochromatic image has image values that vary from black to white, with the black colour represented by an image value of 0 and the white colour by the maximum image value. This maximum value, (the upper limit of the image value), depends on the available resolution of the recording medium.

In computerized image processing, typically 8 bits are used for digitization, providing 2^8 = 256 gray scales. The higher the number of gray scales, the higher the resolution of the image, but this would require more computation time and more storage space.

4.3 Optical Measurements

Optical measurements have been used for decades in the automotive industry, mainly in the development and assessment of safety systems. Such an application is reported to be carried out as far back as in 1938, by General Motors, using a manually controlled camera with a maximum recording speed of 1000 frames per second [84]. Use of high speed cinematography for measuring the vibration levels for a vibration mill used in the manufacturing of ultra fine particle was proposed by Wang et al. in [56]. The concept in such vibration mills is the use of bulk rods or balls as the grinding media in producing ultra fine particles from a base material. In such an application contact measurement principles cannot be used, while due to the transient nature of the vibration, measurement using laser doppler vibrometer is also impossible. The natural frequencies of this complex system, were able to be measured using optical measurements. Spyrou et al. in [85], developed a test procedure using optical measurements for testing steel T-stub assemblies at elevated temperatures and variable loads. A comparison between their video based measurements with conventional methods was performed and found the results to be in good agreement. Patsias and Staszewski in [36], have used optical measurements in identifying the presence and location of damage in

a vibrating cantilever beam. Further details of the use of optical measurements can be found in [41], and the references therein.

The images acquired by any optical measurement method are collected in an image sequence. The time step between consecutive frames of an image sequence is usually kept constant. A routine is developed based on edge detection to extract the variation in the location in the image with respect to time. Using edge detection the contours of each frame in an image sequence is obtained, making motion estimation a more robust and computationally efficient operation.

4.4 Capabilities of an Optical Measurement System

A number of optical measuring devices can be used to form image sequences, ranging from simple video cameras to high speed video systems. The capabilities of each optical measurement system depends on the technical characteristics of the system, with the main parameters being the recording speed which provides the sampling frequencies in frames per second (FPS), the image size (in pixels) and the shutter speed which depends on the surrounding lighting conditions. In this thesis, Mega Speed MS70K with Mega Pixel CMOS Sensor [86], with specifications given in section 7.1 is used.

An appropriate frame rate used to capture the images must be set, depending both on the capabilities of the Optical measuring device, as well as on the maximum frequency at which the structure under consideration is expected to operate. In this thesis, the maximum frequency contained in the random excitation force operating on the experimental cantilever beam is set to 200 Hz. This excitation frequency can excite up to the fifth mode of the cantilever beam, as can be seen in table 7 of section 7.1. Thus to avoid aliasing problems, based on the Nyquist sampling theorem [87], the minimum frame capture rate to be used in this thesis is 500 FPS.

Image size is an important factor to be set, depending on the structure to be recorded. Wide angle and zoom lenses can be used depending whether the structure under investigation is to be recorded in full, or whether enlarging certain locations of the structure is considered. For the purpose of this thesis, recording of the full size of the cantilever beam

is required, so as to be able to record its Operational Deflection Shape (ODS) and its time-domain response at every required location along the length of the beam. Thus an image resolution of 504 x 504 pixels is used.

It is obvious that the capabilities of the image acquisition system places limitations on the maximum frame rate and thus on the maximum frequency of the measurements, resulting in spatial resolution limitations, as well as limitations on the number of images contained in a sequence. Thus before an optical measurement is to be carried out, suitable optimal parameters must be selected. A digital image is formed by digitizing an analogue scene into discrete locations forming a rectangular matrix. The size of the image depends on the hardware used to capture the image, and it is measured in pixels. The distance between pixels in a digital image can be defined in several ways, which can be found in [41]. The most common method however, is to measure the number of pixels in the horizontal (x-direction) and in the vertical (y-direction) directions. This method is the one adopted in this thesis.

4.5 Edge Detection

Edge detection is an important task in image processing, and has attracted many researchers over the last thirty years [88, 89]. It is a tool used in pattern recognition, image segmentation and scene analysis. An edge detector is actually a high-pass filter that can be applied to extract the edge points in an image.

As stated by Jain et al. in [90], edge detection can be summarised in four steps:

1) Smoothing step: In this step the process is to suppress as much noise as possible, without destroying the true edges.

2) Enhancement step: In this step a filter is applied to enhance the quality of the edges in the image (sharpening).

3) Detection step: In this step, which edge pixels should be discarded as noise and which should be retained is determined.

4) Localisation step: In this step, the exact location of an edge is determined. Edge thinning and linking are usually required in this step.

In this thesis, edge detection is used to produce an accurate representation of the state of a vibrating structure at a specific point in time. The detected edges in the image plane, are the boundaries of the vibrating structures, called contours.

Edges in images can be considered as local image singularities. Before the development of wavelet theory, Fourier Transform was the main mathematical tool for analysing singularities. However, the Fourier Transform is global and thus not well adapted to local singularities, whereas Wavelet analysis is a local analysis and thus suitable for singularity detection.

A comprehensive theory of edge detection was presented by Marr and Hildret in [91], and by Canny in [92], whereas Mallat and Zhong [93], suggested the use of wavelet transform in edge detection.

Edge image is a black and white image that consist of the number 0 for black also known as background and 1 for white also known as foreground. Edges often occur at points of large variation in the intensity values in the image. The most common approach is to define an edge as a step discontinuity in the image, considering the image as a two-dimensional signal.

The edges can be located by searching for such discontinuities in the image. This usually is the local maximum of the first derivative or the zero-crossing of the second derivative of the image. Canny was the first to introduce a continuous computational model that can be used for image edge detection. The Canny edge detection method is a projection kernel that when convolved with an image $f(u_1, u_2)$, the zero-crossing of the resulting function are the edges of the image. A description of both first and second derivative edge detection processes as well as of the Canny edge detection and Wavelet Transform edge detection follows.

4.5.1 First Derivative Edge Operators

Edges are considered as discontinuities in the intensity of an image, thus by taking the derivative of intensity values across the image and searching for the maximum values of the derivative, the edge points can be located. For a continuous image $f(x, y)$ its derivative assumes a maximum in the direction of the edge. According to Jain [94], the gradient of the image function f along the direction of the edge is illustrated in figure 15 which is the

gradient of f along r in a direction θ, and is given by,

$$\frac{\partial f}{\partial r} = \frac{\partial f}{\partial x}\frac{\partial x}{\partial r} + \frac{\partial f}{\partial y}\frac{\partial y}{\partial r} = f_x\frac{\partial x}{\partial r} + f_y\frac{\partial y}{\partial r} \tag{19}$$

where $f_x = \frac{\partial f}{\partial x}$ and $f_y = \frac{\partial f}{\partial y}$ are the rates of change of the image function f in the two perpendicular directions.

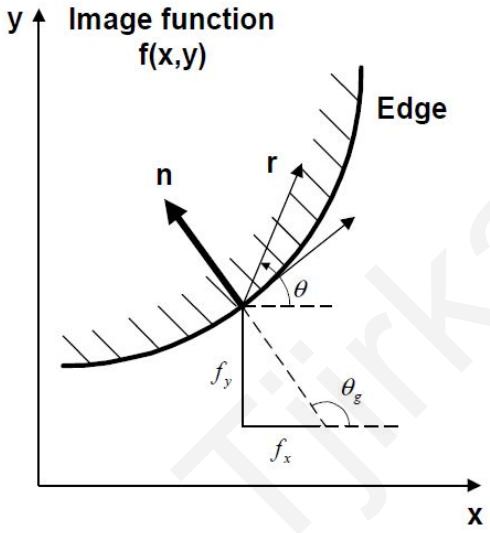

Figure 15: Gradient of image function f along the direction of the edge.

From trigonometry, $sin\ \theta = \frac{\partial y}{\partial r}$ and $cos\ \theta = \frac{\partial x}{\partial r}$. thus equation 19 becomes,

$$\frac{\partial f}{\partial r} = f_x cos\theta + f_y sin\theta \tag{20}$$

The direction of the edge is at 90^o with gradient direction n which gives the direction of the maximum growth of the image function (that is for gray level 0 to maximum value according to the resolution). Thus the maximum rate of change $\frac{\partial f}{\partial r}$ occurs when $\frac{\partial}{\partial \theta}\frac{\partial f}{\partial r} = 0$.

As specified in [41], the magnitude and direction of the edge are given by,

$$M = \sqrt{{f_x}^2 + {f_y}^2} \tag{21}$$

$$\theta = tan^{-1}(\frac{f_y}{f_x}) \tag{22}$$

For digital images, the gradient has to be computed using the difference approximations of either the directional or the orthogonal gradients. For edge detection to be performed, it is necessary to have a method of going through an image systematically. This process is called *correlation*, and is a method by which an image is analysed, by applying a set of rules on it,

which affect the output of each pixel. The operator for edge detection is called kernel, and is basically like a looking-glass, or band-pass filter, through which the output is determined by the rules of the applied kernel [95].

A number of edge detection operators (kernels) have been proposed in the literature, with the simplest one presented by Roberts [94]. This kernel, as well as Prewitt and Sobel kernels are based on the grey-level gradients of pixel values, in an image, originating from the first order derivatives of these particular gradients.

The Roberts operator performs a simple and computationally quick 2D spatial gradient measurement on an image. It highlights regions of high spatial frequency which often correspond to edges [96]. In its most common usage, both the input to the operator and the output is a grayscale image. The pixel neighbourhood is a 2x2 pixels, and the kernel consists of a pair of 2x2 convolution masks defined as:

$$G_x = \begin{pmatrix} 1 & 0 \\ 0 & -1 \end{pmatrix} \qquad (23) \qquad G_y = \begin{pmatrix} 0 & 1 \\ -1 & 0 \end{pmatrix} \qquad (24)$$

These masks are designed to respond maximally to edges running at 45^o to the pixel grid, that is one mask for each of the two perpendicular orientations. The masks can be applied separately to the input image, to produce separate measurements of the component of the gradient in each orientation (G_x and G_y). These are then combined together to find the absolute magnitude and the orientation of the gradient at each point. The magnitude of the gradient is obtained using equation 21, while the angle of orientation of the edge giving rise to the spatial gradient is obtained using equation 22. The output is thresholded to remove any maxima produced by the presence of noise. However, the threshold value is not an easy matter, as there is no automatic procedure to determine the optimum threshold value for all the images.

Sober and Prewitt kernels are a 3 x 3 approximation of the derivatives along the horizontal x and vertical y directions. They perform a 2D spatial gradient measurement on an image, emphasizing regions of high spatial gradient that correspond to edges. They are typically used to find the approximate absolute gradient magnitude at each point in an input greyscale image. The Sobel operator consists of a pair of 3x3 convolution masks defined as:

$$G_x = \begin{pmatrix} -1 & 0 & 1 \\ -2 & 0 & 2 \\ -1 & 0 & 1 \end{pmatrix} \quad (25) \qquad G_y = \begin{pmatrix} -1 & -2 & -1 \\ 0 & 0 & 0 \\ 1 & 2 & 1 \end{pmatrix} \quad (26)$$

These masks are designed to respond maximally to edges running vertically and horizontally relative to the pixel grid, one mask for each of the two perpendicular orientations. Similar to Roberts operator, the masks can be applied separately to the input image to produce separate measurements of the component of the gradient in each orientation (G_x and G_y). These can be combined together to find the absolute magnitude and orientation of the gradient using equations 21 and 22 respectively. The output, as in the case with Roberts operator, is thresholded to remove any maxima produced by the presence of noise.

The effect of noise on the derivatives obtained using the differences of pixel values cannot be ignored, as any discontinuities in the derivative from noise can affect the true maxima that indicate the location of an edge. In order to avoid this problem, the images are smoothed before the derivatives are calculated. The smoothing filter used has to satisfy certain design criteria as provided in [97]. Burt and Adelson have shown in [98] that the Gaussian kernel, as a 2D smoothing operator, defined by equation 27, satisfy the required design criteria.

$$g(x, y) = e^{-\frac{x^2+y^2}{2\sigma^2}} \quad (27)$$

More details about image smoothing can be found in [41, 97].

The Sobel operator is slower to compute than the Roberts operator, but its larger convolution kernel smooth the input image to a greater extent and so makes the operator less sensitive to noise. In general this operator produces considerably higher output values for similar edges, compared to the Roberts operator.

The Prewitt operator works in a very similar way to the Sobel operator but uses slightly different pair of 3x3 convolution masks defined as:

$$G_x = \begin{pmatrix} -1 & 0 & 1 \\ -1 & 0 & 1 \\ -1 & 0 & 1 \end{pmatrix} \quad (28) \qquad G_y = \begin{pmatrix} -1 & -1 & -1 \\ 0 & 0 & 0 \\ 1 & 1 & 1 \end{pmatrix} \quad (29)$$

The results produced are similar to that of the Sobel operator, but not as isotropic in its response, that is the operator is not applied equally well in all the directions in an image.

4.5.2 Second Derivative Edge Operators (Zero crossings)

Marr and Hildreth [91], proposed a second derivative edge operator (kernel), by using the Laplacian of the image function in both the horizontal and the vertical directions as given by equation 30, with the Gaussian distribution used as the optimum filter, using a convolution.

$$\nabla^2 f(x,y) = \frac{\partial^2 f(x,y)}{\partial x^2} + \frac{\partial^2 f(x,y)}{\partial y^2} \tag{30}$$

The main advantage of the second derivative kernel, is that it is easier to determine the zero crossing of the second derivative than the maxima of the first derivative, however there is more influence of noise in the second derivative and thus false edge location is possible to occur.

4.5.3 Canny Edge Detection

Canny in [92] followed a list of criteria to improve current methods of edge detection, which can be summarized as follows:

1) Low error rate criterion, that is edges occuring in images should not be missed and that there are no false responses to non-edges.

2) The edge point to be well localized. This means that the distance between the edge pixels, as found by the detector, and the actual edge is to be at a minimum.

3) Only one response should occur at a single edge, thus eliminating the possibility of multiple responses to an edge.

The Canny edge detector initially smoothens the image to eliminate any noise, and then finds the image gradient to highlight regions with high spatial derivatives. Once a suitable kernel has been calculated, the Gaussian smoothing is performed using standard convolution methods. As the convolution kernel is usually smaller than the actual image, it is slid over the image, manipulating a square of pixels at a time. The Gaussian kernel must not be too large, as the larger its width the lower is the sensitivity to noise. The Sobel operator then, performs a 2D spatial gradient measurement on the image, and the approximate edge strength (the absolute gradient magnitude) at each point is obtained. The Sobel kernels used for estimating the horizontal G_1 and the vertical G_2 gradients are given by equations 25 and 26 respectively. The magnitude, or Edge strength of the gradient is approximated by adding the absolute of the horizontal and vertical gradients: $|G| = |G_1| + |G_2|$.

The next step is for the algorithm to track along the regions with high spatial derivatives and suppress any pixel that is not at the maximum. The gradient array is then further reduced by hysteresis, by tracking along the remaining pixels that have not been suppressed. Hysteresis uses two thresholds and if the magnitude is below the first threshold, it is set to zero, implying that there is no edge. If the magnitude is above the high threshold, it is made an edge. If the magnitude is between the two thresholds, it is set to zero, unless there is a path from this pixel to a pixel with a gradient above the maximum threshold.

The Canny edge detector operator $G\overrightarrow{n}$ as stated in [92] is given by,

$$G\overrightarrow{n} = \frac{\partial G}{\partial \overrightarrow{n}} = \overrightarrow{n}\nabla G \tag{31}$$

where $\overrightarrow{n}$ is the vector normal to the edge curves.

In order to measure the change in the image intensity along the direction normal to the edges, a directional derivative is taken. Since, the edge is unknown, an approximation $\overrightarrow{n} \approx \frac{(\nabla(G\star f)}{|(\nabla(G\star f)|}$ is used. The edge points are thus the solution of,

$$\frac{\partial}{\partial \overrightarrow{n}}(G\overrightarrow{n} \star f) = 0 \tag{32}$$

By substituting the expression in equation 31 for $G\overrightarrow{n}$ equation 33 is obtained, giving the edge points as the inflection points of the image, smoothed by the Gaussian kernel.

$$\frac{\partial^2}{\partial \overrightarrow{n}^2}(G\overrightarrow{n} \star f) = 0 \tag{33}$$

4.5.4 Wavelet Transform Edge Detection

The Wavelet Transform edge detection methodology in images is closely related to Canny's kernel and for a particular class of wavelets it is equivalent to detecting the Wavelet Transform maxima. The multiscale nature of Canny edge detection is controlled by the standard deviation of the Gaussian σ, whereas in the wavelet edge detection, it is controlled by the scale parameter [93]. In Wavelet Transform edge detection, the multiscale edges are obtained from zero crossing of the second derivative of a smoothed signal at various scales [99]. It was suggested by Mallat and Zhong in [93], that a complete representation is not necessarily stable, and thus a precise reconstruction of the original signal from the zero-crossings is not possible. To improve the stability of the reconstruction, the suggestion was to record together with the location of the maxima, the actual maxima value.

The edge detection method used in this thesis, is the Mallat-Zhong (M-Z) Discrete Wavelet Transform (DWT) edge detection, which is based on Mallat's fast multiscale edge detector, details of which are given in [11], and uses an undecimated wavelet transform executed via a filter bank. Although the maxima of the modulus of the discrete wavelet transform approximate well an edge in an image, there are still false edges, even without any noise in the signal. Thus a threshold on the intensity of the modulus maxima is used as a criterion to identify and eliminate the false edges.

For edge detection, a constant threshold is sufficient to be used. The constant threshold is applied to the modulus maxima of a point $u_{j,p}$ on the image, such that the point is an edge point if and only if, the maximum $M_j f[m]$, as given by equation 39 in section 4.6, is greater than the specified constant threshold value. In this thesis, this constant threshold value is set by trial and error for the first and last image of each sequence. This was done to ensure that no major changes in the lighting conditions occurred and so a single threshold value of 2% of the maximum of the absolute values in the image. [i.e. $T = 0.02$ x $max(M_j f[m])$] is used.

4.6 Detecting Edges in an Image

An edge is detected between regions of different intensity. Thus a simple criterion to detect the edges in an image would be the change of a certain magnitude in the intensity of the image between two adjacent pixels in the image. This simple criterion is used by the classical edge detectors such as the Roberts and the Sobel edge detectors, which are using discrete considerations. As mentioned in section 4.2, the gradients are approximated by pixel kernels, a 2x2 kernel in Roberts and a 3x3 kernel in Sobel. These pixel edge detectors are not very good and there is only a finite number of ways to design the kernels, as the kernel cannot be too large, to keep computation processing to acceptable levels. Canny edge detector is a continuous computational model allowing for an adjustment parameter that is a real number unlike the finite number of kernels for the pixel edge detectors. Wavelet edge detector has a built-in sense of scale, or resolution in addition to a free parameter to vary, providing for multiresolution constructions [93].

The scaling function and wavelet associated with M-Z DWT are generated from a quadratic spline filter, as can be seen in equation 34 below, which is a choice made to speed-up computation and prevent group delays that would be introduced by non-symmetric filters.

$$h[n] = \{..., 0, 1, [3], 3, 1, 0...\}\frac{\sqrt{2}}{4} \tag{34}$$

The scaling function and wavelet generated from this filter are illustrated in figure 16.

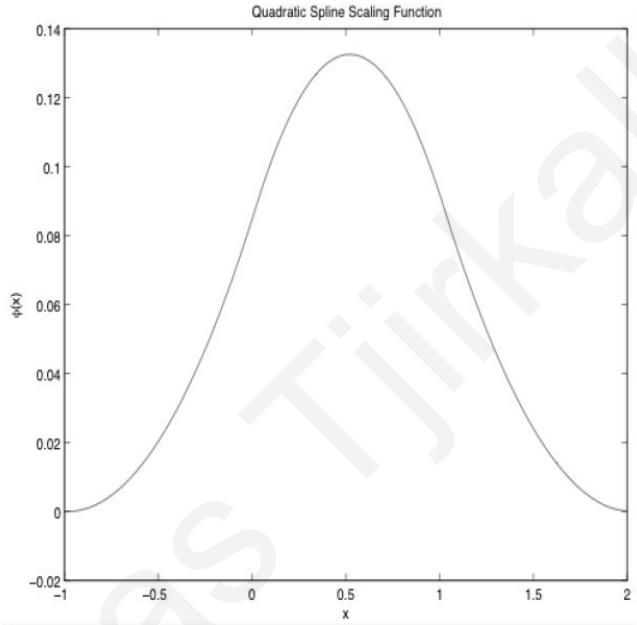

(a) Quadratic scaling function $\phi(x)$

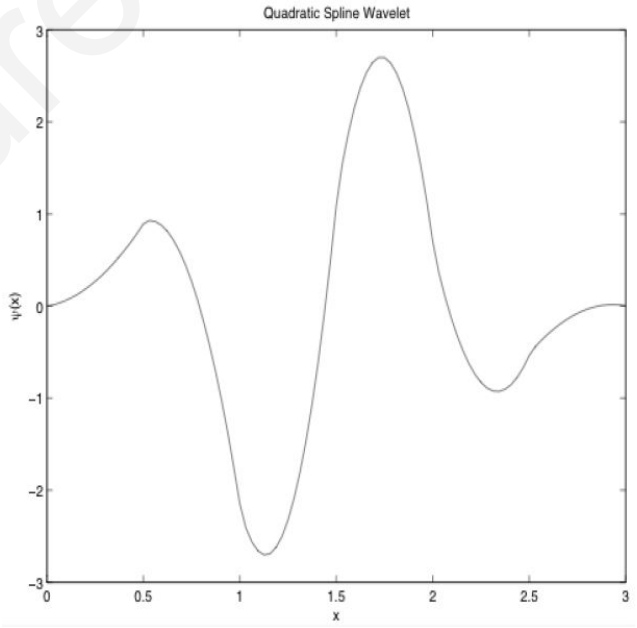

(b) Quadratic wavelet ψ

Figure 16: (a) The quadratic scaling function $\phi(x)$, and (b) the quadratic wavelet ψ.

The decomposition filters at each resolution 2^j are computed by upsampling the filter $h[n]$ by j,

$$\overline{h}[n] = (\uparrow j)h[-n] \tag{35}$$

The $g_j[n]$ filters are normalized finite difference filters that approximate the gradient of the image.

$$\overline{g_j}[\mp 2^{j-1}] = \pm\frac{\sqrt{2}}{2}, \qquad \overline{g_0}[0] = \overline{g_0}[-1] = -\frac{\sqrt{2}}{2} \tag{36}$$

The M-Z DWT is performed by a suggestion of separable convolutions using the above mentioned filters, with Image and Detail Coefficients at each resolution 2_j as displayed in equations 37 and 38 respectively.

$$\text{Image coefficients: } a_{j+1}[m] = a_j \star \overline{h_j h_j}[m] \tag{37}$$

$$\text{Detail coefficients: } d^1_{j+1}[m] = a_j \star \overline{g_j}\delta[m] \qquad d^1_{j+1}[m] = a_j \star \delta\overline{g_j}[m] \tag{38}$$

where $[m]$ = $\{m_1, m_2\}$.

Since an image is a finite object, in order to account for edge effects all the convolutions are circular.

Mallat stated in [11] that the 1D implementation of the M-Z DWT is a stable representation and has perfect reconstruction, whereas the 2D M-Z DWT does not have perfect reconstruction, as the diagonal detail coefficients are not calculated. For edge detection, it is sufficient to calculate the horizontal and vertical wavelet coefficients. Computation can be speed-up by ignoring the diagonal coefficients. It is also shown in [93], that the 2D transform is also stable, and even without perfect reconstruction, a reconstructed image is visually identical with the original, with an error of the order of 10^{-2}.

The local maxima of the modulus of the M-Z DWT is obtained by calculating the modulus and the angle of the DWT using,

$$M_j f[m] = |d^1_j[m]|^2 + |d^2_j[m]|^2 \tag{39}$$

$$A_j f[m] = arg(d^1_j[m] + i \cdot d^2_j[m]) \tag{40}$$

where $[m]$ = $\{m_1, m_2\}$, and $f[m]$ is a discrete sampling of the image $f(u)$ normalized such that $f[m] \in$ [0,1] for all m.

4.7 Image Sequence

In Optical measurement procedure, a collection of images are acquired at predefined time instances, depending on the Capture Speed of the High Speed Camera in Frames Per Second (FPS) used.

An overview of image sequence analysis is given by Al Bovik in [100] and Nagel in [101], where an image sequence is interpreted as an abstraction process, which searches for the minimum number of parameters necessary to describe the recorded data. This abstraction process, can be the localization of grayscale variations that can be found in subsequent images, such as the edge representation of a frame, traced in the subsequent frames. Another process used to describe image sequence analysis, as specified in [41], is ”Dynamic scene analysis” or ”analysis of time varying imagery”, which also refer to the processing of a sequence of images.

The aim of any image sequence analysis, is to obtain information from the whole of the image sequence, that cannot be obtained from individual images, and thus can provide information about the motion of a structure, by locating the moving regions in the images. This can be done either by feature or by pixel based segmentation.

Feature-based segmentation is a term used to describe image processing methods that extract feature like edges. The features extracted can also be corners or other distinguishable descriptions. Pixel-based segmentation uses pixels intensity values to obtain velocity estimates as illustrated in [102]. In this thesis, feature-based segmentation and in particular edge contours is employed in the analysis of acquired image sequences.

Correspondence in image sequence

The correspondence problem is necessary to be accounted for before any measurements from image sequences can be made. The correspondence step is to match the structures features, as are the edge contours for this thesis, in the first frame to that of the subsequence frames. The method that achieves this matching is called a correspondence procedure.

For vibration measurements, only the structure vibrating is of interest, thus the background can be ignored, and the physical corners of the structure can be used in order to track its motion, eliminating the correspondence problem. In cases where the structure under consideration does not have distinguishable physical features, then artificial features,

such as markers, as suggested in [103] can be added. It should be emphasized that the added markers must not interfere with the dynamics of the system under consideration.

Another problem that can occur in image sequence is occlusion. This happens if the structure being tracked is obscured by another moving object or by a sudden shadow, thus causing uncertainties in the interpretation of the image as stated in [41]. In this thesis, care is taken not to obscure the vibrating structure, thus occlusion does not cause any problems.

Chapter 5

Structural Health Monitoring based on WTMM decay line similarity

An overview of the WTMM decay line similarity as a feature extracted in damage identification obtained using Normalized Cross Correlation (NCC) is presented in this chapter. Besides the effectiveness of this principle is demonstrated on the ARMA and ARIMA model motivational example. The principle of the Difference of the Pointwise Summation of Similar WTMM decay lines, abbreviated by $DSSD$, used in cases where a decision about damage existence cannot be made from the similarity between the WTMM decay lines directly, is also provided. These principles are employed in a proposed Damage Detection Methodology, which enables the detection of the presence of damage from the time response signal of vibrating structures, while at the same time distinguishing the changes in the time response due to damage existence to changes due to environmental and/or operational variability.

5.1 Wavelet Transform Modulus Maxima (WTMM) decay line similarity

In Chapter 3, the possibility of WTMM decay lines to be used as a feature that can be extracted from the time response signal of a vibrating structure under investigation, capable in identifying the presence of singularities and thus damage in the structure was discussed. However, real life structures are subjected to changing environmental and operational conditions, such as temperature and moisture, which cause significant changes in its properties. Thus in order for a SHM method to be utilised in real life monitoring of structures, it must account for the effects of varying environmental and/or operational conditions.

The motivation example using the ARMA and ARIMA models in section 3.2, demonstrated that the change in WTMM decay lines in a time range varies depending whether the change induced was due to the introduction of damage in the time response signal or due to varying environmental and/or operational conditions or a combination of them.

This indicates that the similarity of WTMM decay lines between successive time ranges can be used to provide an effective damage detection method under varying environmental and/or operational variability conditions. Two WTMM decay lines, are considered to be similar if they are of the same shape, even if their magnitudes are not the same.

For the identification of similar WTMM decay lines between successive time ranges a mathematical tool capable to measure this similarity is necessary to be developed and implemented in a damage detection methodology. One such mathematical tool was developed based on the principle of Normalize Cross Correlation (NCC), details of which are given in the following section.

It was also observed that some WTMM decay lines, under certain operational and/or environmental variability conditions, apart from being similar they were also identical, that is they were exactly the same. In section 5.4, a methodology that quantifies the vertical distance between two similar WTMM decay lines using the pointwise summation of WTMM decay lines, abbreviated by $DSSD$, is devised. Typical plots of similar and identical WTMM decay lines as well as similar but non identical WTMM decay lines can be seen in figures 17 (a) and (b) respectively.

As it will be discussed in section 5.5, where the Damage detection methodology is given, this principle is useful in cases when a decision about damage existence cannot be made from the similarity between the WTMM decay lines, using the NCC principle.

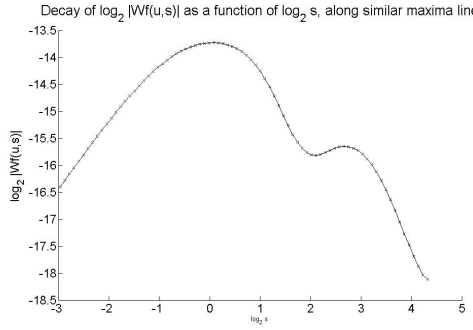

(a) Similar identical WTMM decay lines with meanDSSD=0

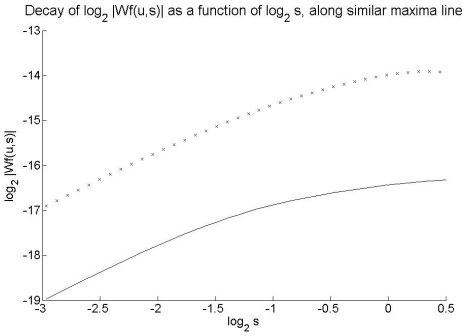

(b) Similar non-identical WTMM decay lines with meanDSSD=0.71

Figure 17: Plot of (a) similar identical (meanDSSD = 0) and (b) similar non-identical (meanDSSD $\neq$ 0) WTMM decay lines.

5.2 Normalized Cross Correlation and WTMM decay line similarity

Autocorrelation refers to the correlation of a time series with its own past and future values. Autocorrelation can be exploited for predictions as an autocorrelated time series is predictable, probabilistically, because future values depend on current and past values. Three tools for assessing the autocorrelation of a time series are (a) the time series plots, (b) the lagged scatterplot, and (c) the autocorrelation function.

The autocorrelation function $C(\tau)$ measures the correlation of a signal $x(t)$ with itself shifted by some time delay τ,

$$C(\tau) = \frac{1}{t-\tau} \int_0^{t-\tau} x(t)x(t+\tau)dt \tag{41}$$

Cross-correlation is essentially the same process but instead of comparing a sequence with a time shifted version of itself, it compares two different sequences. The cross-correlation measures the similarity in shape between two signals as a scalar between 0 and 1. Two signals with exactly the same shape will have a cross-correlation of 1.0. Uniform scaling (that is changing the amplitude of the signal without changing its shape) does not affect the cross-correlation results. Cross-correlation measures are useful in statistical analysis, financial analysis [104], biomechanics [105] and engineering [106]. As stated in [107], correlation is applicable to nonperiodic, periodic as well as random signals, and are respectively given by,

$$R_{xy}(\tau) = \int_{-\infty}^{+\infty} x(t)y(t+\tau)dt \tag{42}$$

for non-periodic functions $x(t)$ and $y(t)$,

$$R_T xy(\tau) = \frac{1}{T}\int_T x_T(t)y_T(t+\tau)dt \tag{43}$$

for periodic functions $x_T(t)$ and $y_T(t)$ and

$$R_{a,xy}(\tau) = \lim_{T\to\infty}\frac{1}{T}\int_{-T/2}^{T/2} x(t)y(t+\tau)dt \tag{44}$$

for random or noise signals $x(t)$ and $y(t)$. More details about correlation measures can be found in [107, 108] and the references therein.

As the correlation of two high amplitude signals tend to give big numbers, the similarity of two signals cannot be determined by just comparing the amplitude of their cross correlation, but their Normalized Cross Correlation (NCC) is needed, which for two time domain signals can be defined by,

$$NCC(x,y) = \frac{|R_{a,xy}(\tau)|}{||x(t)||_2 * ||y(t)||_2} \tag{45}$$

where x and y are the signals under comparison and $||\ ||_2$, denotes the Euclidean norm.

The NCC quantity varies between -1 and 1. A value of $NCC(x,y)$ = 1 indicates that the two signals (x and y) have exactly the same shape, even though their amplitudes may be different, while a value of $NCC(x,y)$ = -1 indicates that the two signals (x and y) have the same shape but opposite signs. A value of $NCC(x,y)$ = 0 indicates that the two signals (x and y) are completely uncorrelated.

The maximum magnitude of the Normalized Cross Correlation (NCC) is used in this thesis, to enable the comparison between the WTMM decay lines between successive time ranges, by measuring their similarity. Based on equation 45 this is defined by,

$$maxNCC(DLt_n, DLt_m) = \frac{max|R_{a,(DLt_n,DLt_m)}|}{||DLt_n||_2 * ||DLt_m||_2} \tag{46}$$

where DLt_n and DLt_m are vectors with the values of the WTMM decay lines under consideration, $||\ ||_2$, denotes the Euclidean norm, and *n*, *m* indicate different time ranges.

In section 5.3, the effectiveness of the principle of the NCC using WTMM decay lines, in order to identify the number of similar WTMM decay lines between successive time

ranges, and thus the presence of non-singularities, is investigated using the ARMA and ARIMA model motivational example, presented in section 3.8

5.3 Identification of similar WTMM decay lines using NCC with the ARMA/ARIMA Motivational Example

From the results obtained using the ARMA and ARIMA motivational example model in section 3.8, it was observed that WTMM decay lines seem to be a promising feature to be extracted in identifying the presence of singularities in a time response signal. To enable this feature extraction process, the similarity of WTMM decay line between successive time ranges of the response of the model, based on the NCC principle as described in section 5.2 is used.

It is observed that by changing the coefficient values of $C(T)$ from C_1 to C_2, where C_1= $[\frac{1}{3}, \frac{1}{3}, \frac{1}{3}]$ and C_2= $[\frac{2}{3}, \frac{2}{3}, \frac{2}{3}]$, while keeping the coefficinet values of $A(T)$ and the realisation of $e(t)$ the same, the total number of WTMM decay lines in both time ranges remain constant and are 277. The number of similar WTMM decay lines between the two time ranges is obtained, using the NCC principle, to be 108. On the other hand, if the coefficient values of $A(T)$ are varied from A_1 to A_2, where A_1=[1, -0.5783, 0.2138] and A_2 = [1, -1.2, 0.2138], a unit root is introduced in the model. This indicates the introduction of non-stationarity in the signal. The total number of WTMM decay lines between the time ranges reduces from 277 to 209, while the number of similar WTMM decay lines between the two time ranges reduces to 24.

The above observations indicate that the similarity of WTMM decay lines between time ranges obtained from the CWT of time series can be used to identify the presence of damage, and distinguish it from changes due to varying environmental effects, if the WTMM decay line similarity process is employed in a Damage Detection methodology. Such a novel Damage Detection methodology was developed for the purpose of this research and it is presented in section 5.5.

However, before going on to present the proposed Damage Detection Methodology, during the damage detection procedure, as will be presented in the following chapters, it was observed that there is some possibility under different force realisations or different forcing conditions and/or varying environmental conditions and/or the introduction of damage in

the structure, that a decision about damage existence cannot be made from the similarity between the WTMM decay lines. For this case, a method based on the Difference of the Pointwise Summation of Similar WTMM decay lines, abbreviated by $DSSD$, that computes the distance between the maximum in length WTMM decay line in different time ranges with a reference one is proposed. This novel method which is presented in the following section, enables the identification of changes in the WTMM decay lines due to the presence of damage, to changes due to different force realisation and/or varying operational conditions, if a decision about the introduction of damage into a structure or not cannot be made using the WTMM decay line similarity principle directly.

The effectiveness of the proposed Damage Detection Methodology presented is section 5, is tested using both a simulated 3-DOF mass, spring, damper system, and an experimental cantilever beam, as described in chapters 6 and 7 respectively.

5.4 Difference of the Pointwise Summation of Similar WTMM decay lines (DSSD)

The necessity for a method of distinguishing changes due to damage from those due to changing environmental and/or operational conditions was discussed in the previous section. A method called the Difference of the Pointwise Summation of Similar WTMM decay lines and abbreviated by $DSSD$ is proposed in this section. $DSSD$ can be used to identify whether two similar signals are identical or not, and enables the quantification of the vertical distance between two signals, and hence their difference in magnitude. This is done by obtaining the difference between the summation of corresponding points along the length of two WTMM decay lines as follows,

$$DSSD_n = \sum_{d=1}^{k} |y(DLt_n)_d| - \sum_{d=1}^{j} |y(DLt_{(n-1)})_d| \tag{47}$$

where y(DLt_n) and y(DLt_{n-1}) are the points along the WTMM decay line of the corresponding current *n*, and previous *n-1* time ranges respectively, and *k*, *j* are the total number of points in the WTMM decay lines in ranges *n* and *n-1* respectively.

The $DSSD$, as illustrated in equation 47, is actually the difference of the summations of the absolute values of all points along a WTMM decay line of the current time range with its corresponding/similar WTMM decay line of the previous time range. It should be noted that if the mean value of $DSSD = 0$ the corresponding similar WTMM decay lines between

successive time ranges are identical, as shown in figure 17 (a), whereas if the mean value of $DSSD \neq 0$ they are non identical as shown in figure 17 (b).

The $DSSD$ principle can be used to distinguish the changes in the time response signals that are due to changes in forcing conditions and/or force realisation, to changes due to the presence of damage, and its effectiveness is tested using both the 3-DOF mass spring damper simulation system and the experimental cantilever beam.

For the $DSSD$ principle to be capable in distinguishing between the above two cases, the WTMM decay line with the maximum length, that is the one that extends through all the scales, of the first time range, from the start of the damage detection algorithm is stored as the reference one. The WTMM decay line with the maximum length in the current time range is then compared to the reference one. The comparison is done by considering the WTMM decay line as two halves, and using the $DSSD$ principle, the difference of the pointwise summation of the WTMM decay lines between the current time range and the reference one in the 1^{st} and 2^{nd} half respectively is obtained, resulting in two vectors the $DSSD_{1^{st}}$ and $DSSD_{2^{nd}}$.

To demonstrate the ability of the proposed $DSSD$ principle in distinguishing changes due to damage to the ones due to environmental and/or operational variability, the principle is used with the time response measurement of the 3 DOF simulation system, details of which are given in chapter 6, under six different cases summarised in table 2 with their corresponding plots shown in figure 18.

Table 2: DSSD principle for 6 cases between successive time ranges using the 3DOF simulation system

Case	Change between successive time range	mean $DSSD_{1^{st}}$	mean $DSSD_{2^{nd}}$
(a)	No change	0	0
(b)	Introduce damage	0.0062	0.5098
(c)	Force realisation	0.7455	0.3255
(d)	Force from pink to white noise	2.0831	0.2954
(e)	Temperature	0.1745	0.2070
(f)	Temperature & Damage	0.4581	0.8083

From the results summarised in table 2, as well as from the plots in figure 18 below, the following conclusions are obtained:

(a) If in the time range under consideration, the system is operating under the same environmental and operational conditions as with the previous time range, and no damage is introduce between the time ranges, then $meanDSSD_{1^{st}} = meanDSSD_{2^{nd}} = 0$.

(b) If in the time range under consideration, the system is operating under the same forcing conditions, but varying temperature (environmental) conditions compared to the previous time range, and no damage is introduced between the two time ranges, then $meanDSSD_{1^{st}} \approx meanDSSD_{2^{nd}} < 0.3$.

(c) If the operational conditions and/or the force realisation between the current and the previous time ranges are varied, while the temperature (environmental) conditions remain constant, and no damage is introduced between the two time ranges, then $meanDSSD_{1^{st}} > meanDSSD_{2^{nd}}$.

(d) If the environmental and operational conditions remain unchanged between the current and the previous time range, but damage is introduced into the system then $meanDSSD_{1^{st}} < meanDSSD_{2^{nd}}$.

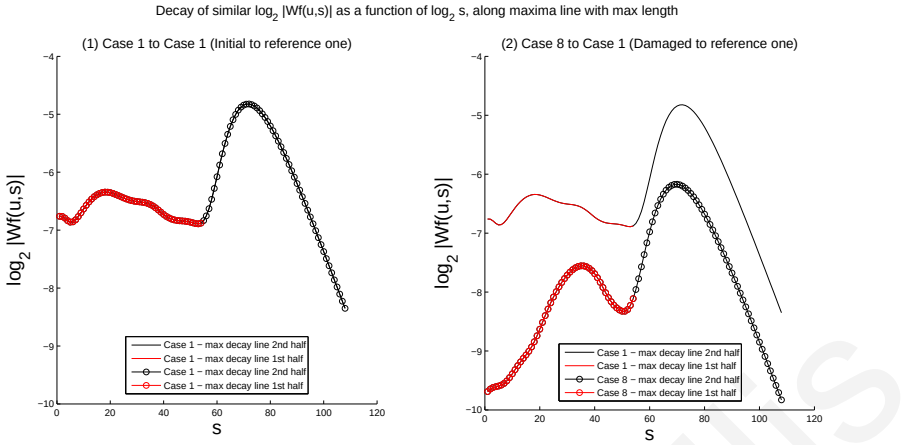

(a) DSSD (1) Initial - reference $DSSD_{1^{st}}$=$DSSD_{2^{nd}}$=0 , (2) Damaged, $DSSD_{1^{st}}$=0.0062, $DSSD_{2^{nd}}$=0.5098

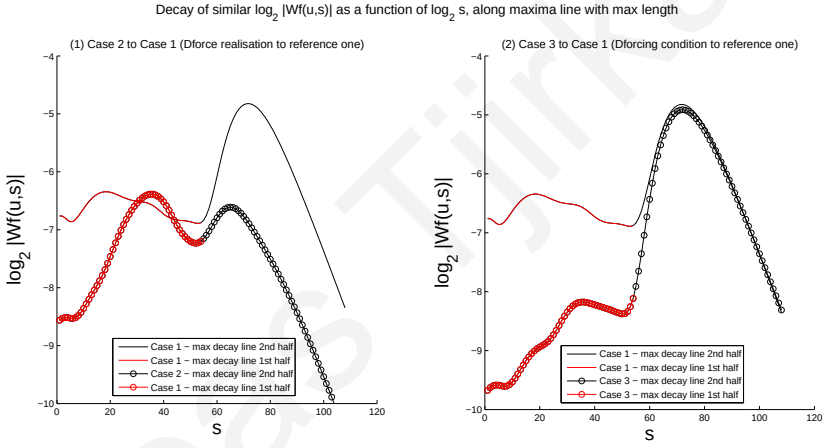

(b) DSSD (1) Δf realisation: $DSSD_{1^{st}}$=0.7455, $DSSD_{2^{nd}}$=0.3255, (2) Δf pink to white noise: $DSSD_{1^{st}}$=2.0831, $DSSD_{2^{nd}}$=0.2954

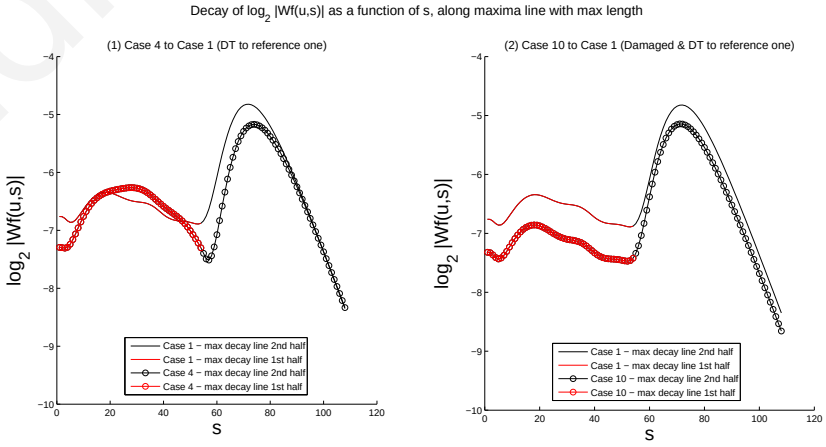

(c) DSSD (1) ΔT: $DSSD_{1^{st}}$=0.1745, $DSSD_{2^{nd}}$=0.2070, (2) ΔT and Damage: $DSSD_{1^{st}}$=0.4581, $DSSD_{2^{nd}}$=0.8083

Figure 18: Mean value of the $DSSD$ between current time range WTMM decay line with maximum length to the reference one, under Cases 1, 8, 2, 3, 4 and 10 respectively.

The $DSSD$ principle together with the principle of similar WTMM decay lines between successive time ranges are employed in a Damage Detection methodology, described in the following section.

5.5 Damage Detection Methodology

To enable the effective detection of damage introduction in a dynamic system during operation under varying environmental and/or operational conditions, the principles of WTMM decay line similarity, described in section 5.2, and $DSSD$, described in section 5.4, are employed in a proposed damage detection methodology, presented in this section.

For the proposed Damage Detection Methodology, the time response of a vibrating structure under consideration is measured, in specified time ranges. Time ranges of 2000 up to 10000 time samples have been investigated, with the 2000 and 4000 time samples per time range adopted so as to enhance computational speed. The recorded time series in each range is normalized by setting the maximum value in the time series to unity. This is done in order to eliminate the effects due to the variations in the amplitude of the excitation force.

Using CWT analysis, the Wavelet Transform Modulus Maxima (WTMM) and their corresponding decay lines of the normalized signal in each time range are obtained. It should be noted that only the decay lines that have a decay line length (DLL) threshold value above a specified value are considered. This is done to remove the effect of noise, as according to Peng et. al in [109], the WTMM decay lines generated by the presence of noise are short in length, and thus can be eliminated by excluding the decay lines which have a length shorter than the specified DLL threshold value. The DLL threshold value is set according to the application that the damage detection algorithm is to be adopted, but it has been observed that a DLL value of 40 is adequate to remove noise in experimental applications.

The similarity between the WTMM decay lines of successive time ranges is obtained using the NCC principle, resulting in a similarity value for each of the compared decay lines in successive time ranges, which are stored in a "Similarity Array". This is a 2-dimensional array, where each k^{th} column of the j^{th} row contains the similarity value between the k^{th} WTMM decay line in the current time range with the j^{th} WTMM decay line in the previous time range. In order to identify that two WTMM decay lines are similar or not, a Similarity

Threshold Value (STV) is specified, according to the application that the Damage Detection methodology is to be adopted.

The number of WTMM decay lines between successive time ranges that have a similarity value equal to or greater than the STV are recorded, resulting in the so-called Successive WTMM Decay line Similarity (SDS) number, indicating the number of similar WTMM decay lines between successive time ranges. If the SDS number is greater than a set value called the Damage Possibility Similarity (DPS) number, then the structure is operating without any damage, with the changes in the time series being due to operational and/or environmental variability. If the SDS number is less than a set value called the Damage Indication Similarity (DIS) number, then damage has been introduced at that current time range into the structure. Both the DIS and DPS numbers used in the Damage Detection methodology, are set according to the system under monitoring.

However, when the SDS number is greater than the DIS number but less than the DPS number, the changes in the time series are either due to changing force realisation and/or forcing conditions or due to the presence of damage in the structure. In order to distinguish between these two cases, the $DSSD$ principle between the WTMM decay line with the maximum length, and thus the one that extents throughout all the scales, in the current and previous time ranges compared with a reference WTMM decay line is adopted. The reference WTMM decay line used is the decay line with the maximum length in the first time range from the start of the Damage Detection monitoring.

If the mean value of the $DSSD$ between the current time range and the reference time range, indicating the distance in the first half of the decay line between the two cases, is greater than the mean value of the $DSSD$ in the second half of the decay line, as is the case in figure 18 b, ($meanDSSD_{1^{st}} > meanDSSD_{2^{nd}}$), then the changes resulting in the SDS number to be in the range between the DIS and DPS numbers ($DIS < SDS < DPS$) is due to changes in the force realisation and/or forcing conditions, whereas if the mean value of the $DSSD$ in the first half of the decay line between the current and reference time ranges is less than or equal to the mean value of the $DSSD$ in the second half of the decay line, as is the case in figure 18 $a(2)$ and $c(2)$, ($meanDSSD_{1^{st}} < meanDSSD_{2^{nd}}$), then damage has been introduced into the structure.

The Damage Detection methodology is also capable to identify the increasing order / severity of damage in a structure. This enables the setting up of a crack order acceptable

limit, called the damage tolerance, before the structure under consideration can be classified as dangerous and thus required to be taken out of operation, in order to be repaired or replaced. However, the process of setting up of a damage order acceptable limit is still under research. The proposed Damage Detection Methodology is illustrated in a flowchart in figure 19 for clarity.

The proposed Damage Detection methodology is tested using a 3DOF mass-spring-damper simulation system, as well as experimentally using a cantilever beam, the results of which are shown in chapters 6 and 7 respectively.

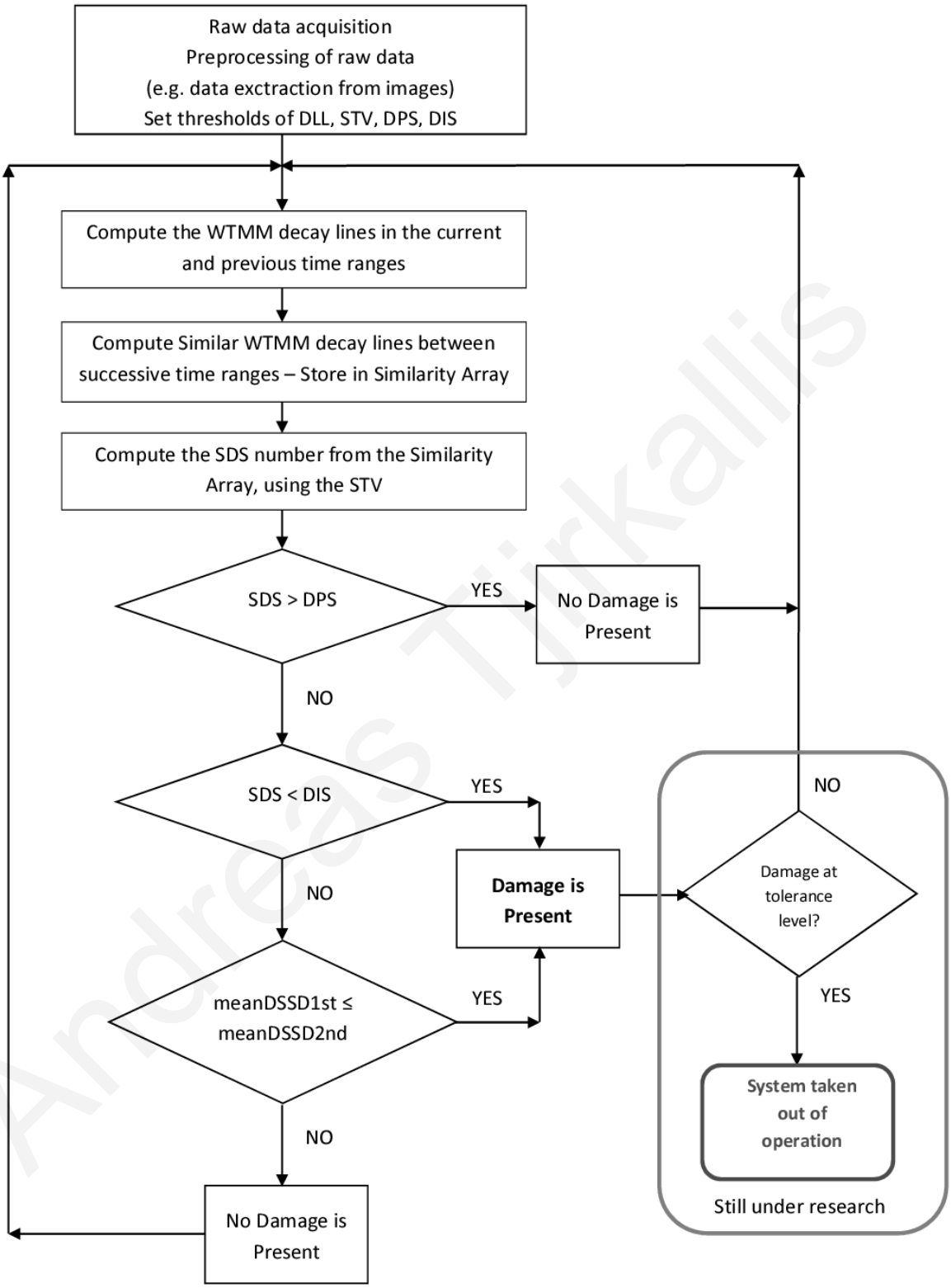

Figure 19: Damage Detection Methodology Flowchart

Chapter 6

Simulation System and Results

6.1 Simulation System

The validity of the proposed methodology is demonstrated using a simulated system. This is a linear, 3 DOF, lightly-damped, mass, spring, damper system as shown in figure 20. The system is excited by both a pink and white noise force, acting on each of the three masses respectively, as well as on all the three masses simultaneously, generated in Labview® [110]. Pink noise occurs in many physical, biological and economic systems, and thus pink noise force simulates general real life excitations. White noise is a signal that contains equal power within any frequency band with a fixed width, and it is used in many scientific and technical disciplines as well as in experimental cases.

The time-domain responses of the three masses are measured, under varying environmental and/or forcing conditions. Damage is simulated in the system by a stiffness reduction of a spring. The spring stiffness is gradually reduced from a value of 450 N/m, which is the initial, intact state, up to a value of 45 N/m, to simulate varying degrees of damage in a system. Damage is introduced at a different spring every time, simulating the location of damage at different parts of the system. The temperature variation is simulated by increasing linearly all four stiffness gradually with respect to running time. This is indicative of a hardening temperature effect [111].

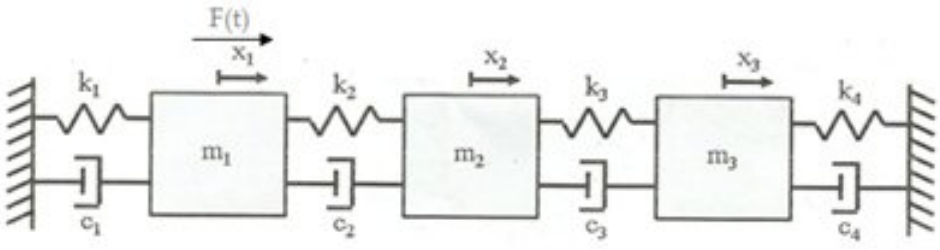

Figure 20: 3DOF mass(m_i) - spring(k_i) - damper(c_i) system

The masses ($m_1 = m_2 = m_3$ = 1kg) as well as the damping values of the system ($c_1 = c_2 = c_3 = c_4$ = 0.2 Ns/m) are kept constant throughout the simulated analysis. An intact system is considered as one having all the spring constants equal to 450 N/m. The time response, CWT, Power Spectrum Density (PSD), WTMM and WTMM decay lines of pink-noise random excitation force are shown in figure 21, whereas that of white-noise random excitation force in figure 22.

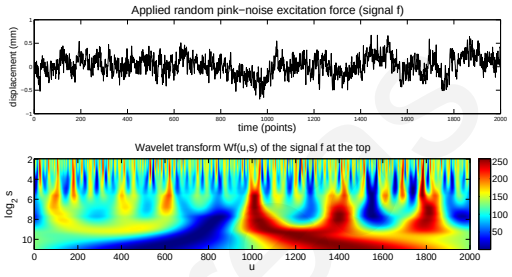

(a) Pink-noise force time response and CWT

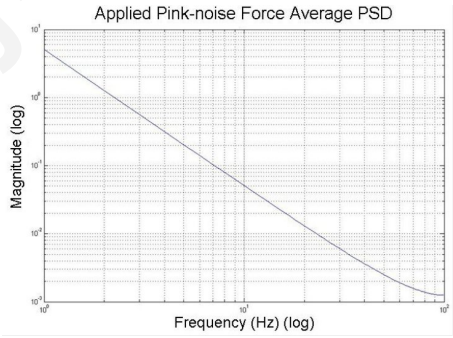

(b) Pink-noise force PSD

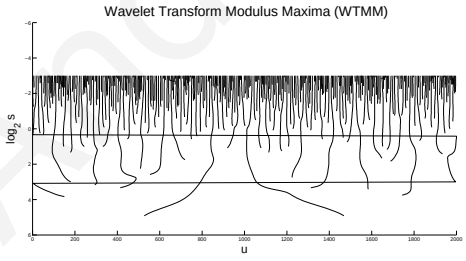

(c) Pink-noise force WTMM

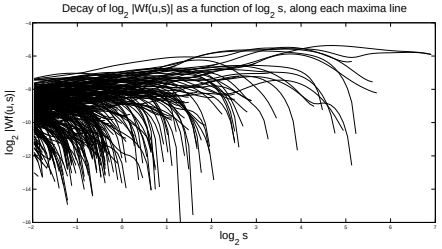

(d) Pink-noise force WTMM decay lines

Figure 21: Pink-noise excitation force (a) time response and CWT, (b) PSD, (c) WTMM and (d) WTMM decay lines

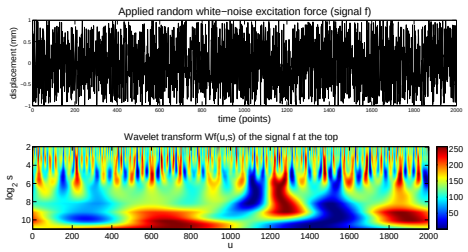

(a) White-noise force time response and CWT

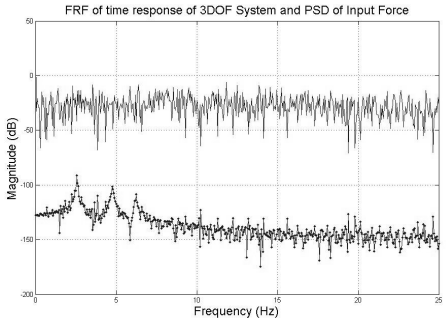

(b) White-noise force PSD

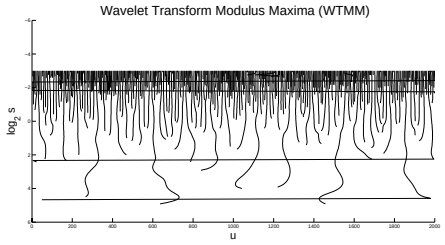

(c) White-noise force WTMM

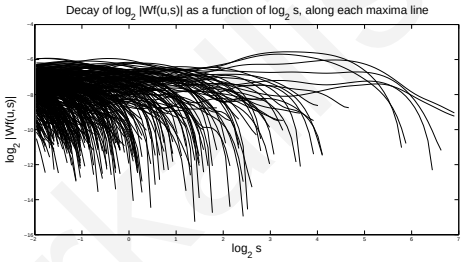

(d) White-noise force WTMM decay lines

Figure 22: White-noise excitation force (a) time response and CWT, (b) PSD, (c) WTMM and (d) WTMM decay lines

It should be noted that in figure 22 (b) the Frequency Response Function (FRF) of the 3 DOF simulation system in an intact state, under white-noise excitation force is given, together with the PSD of the excitation force.

6.2 Simulation System Results when excitation force is acting on a single mass

The time-domain responses of the three masses under pink noise excitation force, acting on mass 1 of the 3 DOF simulation system in an intact case under constant temperature is illustrated in figure 23.

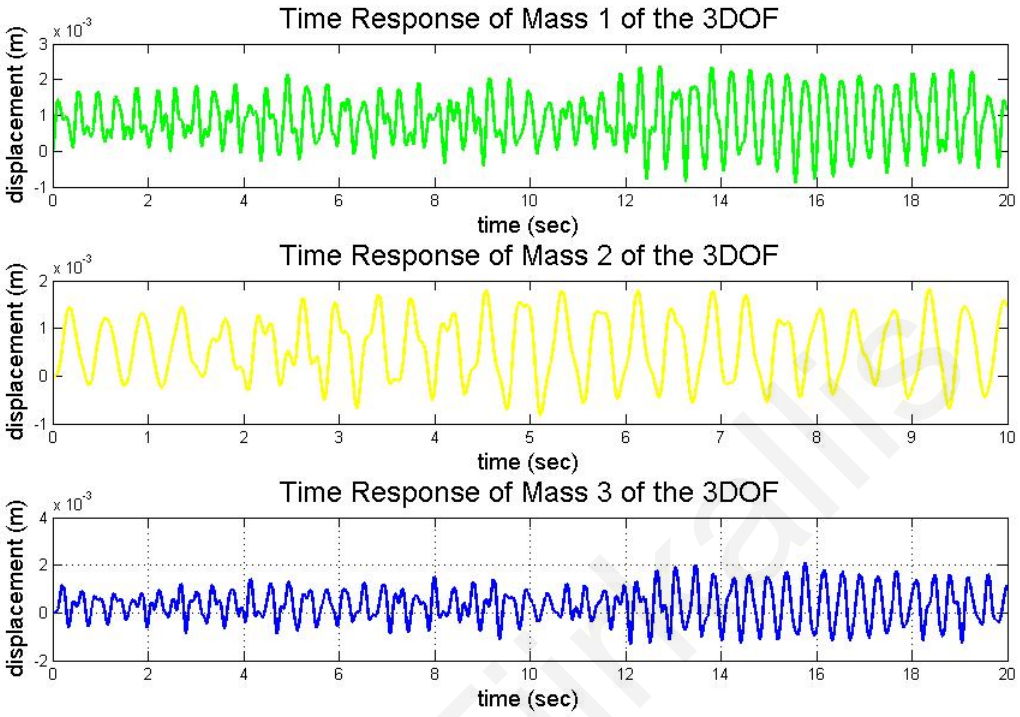

Figure 23: 3DOF system time-domain response of all three masses, under pink noise excitation force acting on mass 1

The time response of mass 1 with its corresponding CWT, WTMM and their WTMM decay lines under different operational and environmental conditions which are summarised in table 3, and cover all the possible environmental and/or operational condition variability, are obtained. The time-domain responses have been normalized with the maximum value in the time series set to unity, to eliminate changes associated with variations in the amplitude of the excitation force.

Typical time-domain responses of mass 1, with their CWT and WTMM decay lines for cases 1, 2, 7 and 11 are shown in figures 24 and 25, whereas for the other seven cases are shown in figures 48, 49 and 50 in appendix A.2. It has to be noticed that for the damaged cases (cases 7 to 11), the simulated damage is introduced at spring k_1 by reducing its stiffness from 450 N/m to 225 N/m. As it can be seen from the plots in figures 24 and 25, neither is it possible to identify the existence of damage in the structure, nor can it be distinguished by changes due to environmental and/or force realisation and/or forcing conditions, without employing the proposed SHM methodology.

Table 3: Cases under which the time response of the simulation model is obtained

01-Intact case, Constant Temp., Pink-noise force
02-Intact case, Constant Temp., Pink-noise force - different realisation
03-Intact case, Constant Temp., White-noise force
04-Intact case, Varying Temp., Pink-noise force
05-Intact case, Varying Temp., Pink-noise force - different realisation
06-Intact case, Varying Temp., White-noise force
07-Damaged case, Constant Temp., Pink-noise force
08-Damaged case, Constant Temp., Pink-noise force - different realisation
09-Damaged case, Constant Temp., White-noise force
10-Damaged case, Varying Temp., Pink-noise force
11-Damaged case, Varying Temp., White-noise force

For this application the number of samples in each time range is set to 4000, which has been found to be a good compromise between accuracy in the results and computational speed. The CWT, WTMM and WTMM decay lines for each time range is obtained. Using the methodology proposed in section 5.5, the number of similar WTMM decay lines between successive time ranges, that have a length greater than the DLL threshold value, which for this application is set to 40, is obtained. These similarity values are stored in a "Similarity array". For this application the STV value is set to 0.9997, thus if the value between any k^{th} column of the j^{th} row, containing the similarity value between the k^{th} WTMM decay line in the current time range with the j^{th} WTMM decay line in the previous time range is greater than the STV value, then the corresponding WTMM decay lines are considered to be similar.

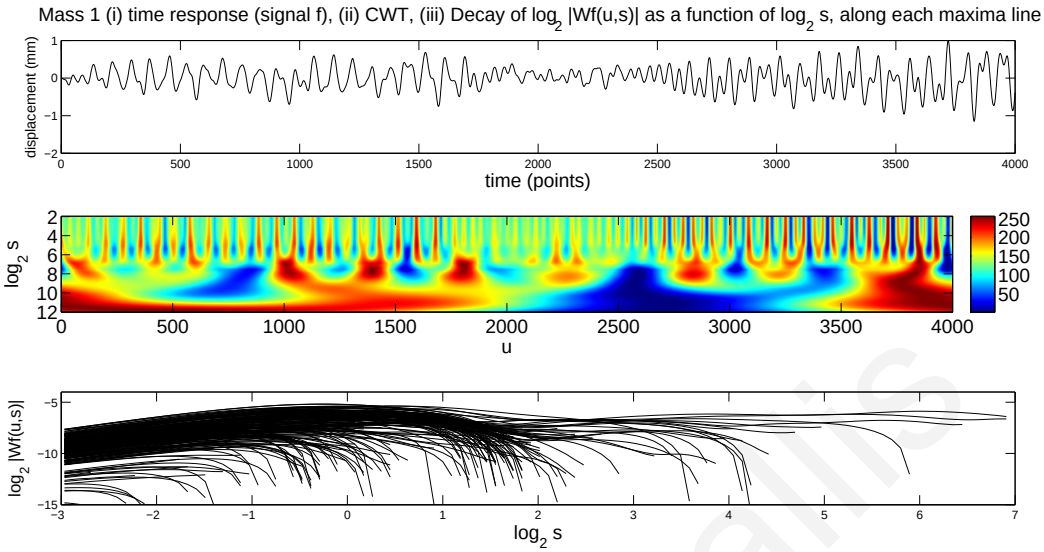

(a) (Case 1) Intact, Constant T, Pink-noise force (i) time response, (ii) CWT, (iii) WTMM decay lines

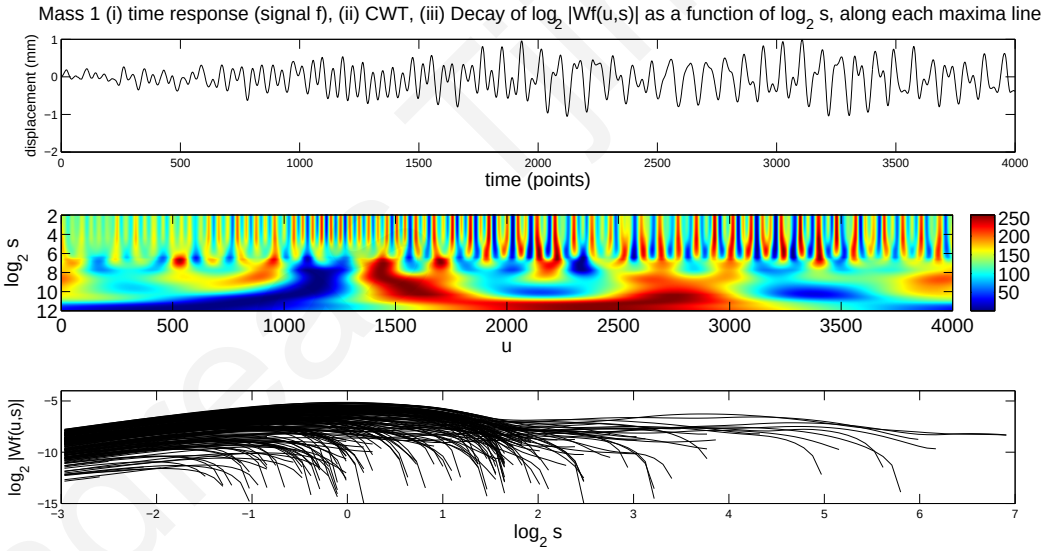

(b) (Case 2) Intact, Constant T, Pink-noise force different realisation (i) time response, (ii) CWT, (iii) WTMM decay lines

Figure 24: 3DOF mass 1 time domain response, CWT and WTMM Decay lines for cases 1 and 2 (Intact cases)

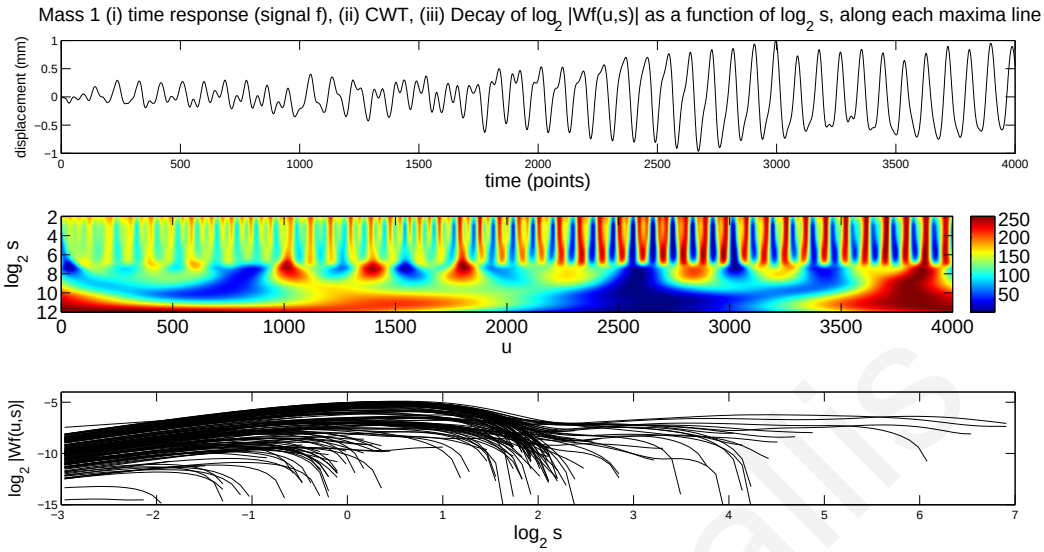

(a) (Case 7) Damaged, Constant T, Pink-noise force (i) time response, (ii) CWT, (iii) WTMM decay lines

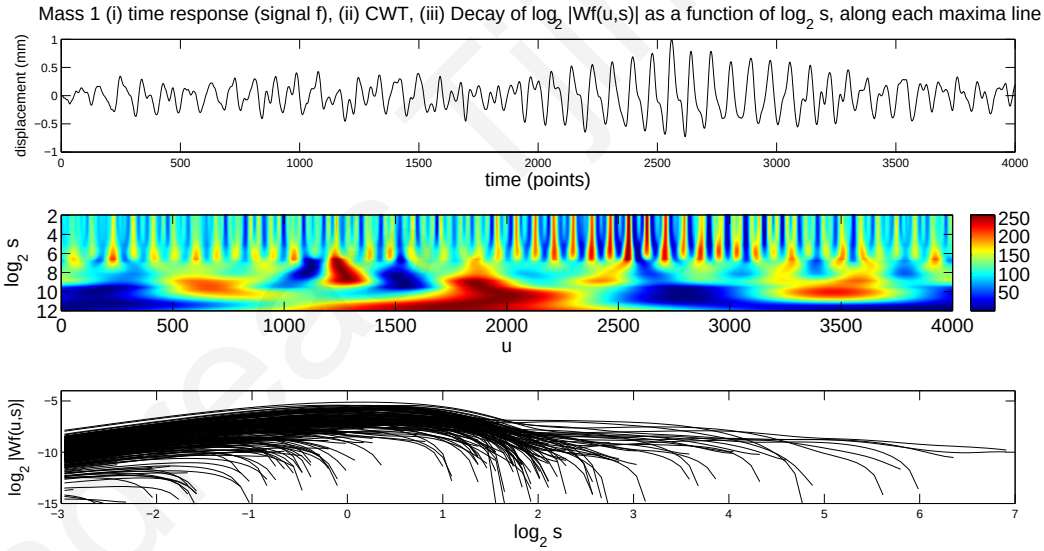

(b) (Case 11) Damaged, ΔT, Pink-noise (i) force response, (ii) CWT, (iii) WTMM decay lines

Figure 25: 3DOF mass 1 time domain response, CWT and WTMM Decay lines for cases 7 and 11 (damaged cases)

To test the effectiveness of the proposed methodology, the environmental and/or operational conditions as well as the healthy state of the system is varied in each time range, according to the 11 cases given in table 3. An extract from the ”Similarity Array” between successive time ranges, where both environmental and operational conditions remain unchanged, and no damage is introduced (case 1) can be seen in figure 26, while for the time ranges corresponding to cases 2, 7 and 11 in figure 51 of Appendix A.2. It should be noted

that the WTMM decay line with the maximum length of the initial time range (case 1) is stored as a reference one, to be used in the $DSSD$ principle.

1	0.993101	0.973047	0.938298	0.89296	0.874651	0.861623	0.844928	0.846568	0.838725	0.844613	0.840371	0.832667	0.825572
0.993101	**1**	0.975651	0.950206	0.91204	0.905106	0.889712	0.874507	0.875095	0.866261	0.875153	0.874517	0.866397	0.85237
0.973047	0.975651	**1**	0.964386	0.916684	0.900609	0.883833	0.867516	0.86836	0.86015	0.865726	0.860531	0.85124	0.840885
0.938298	0.950206	0.964386	**1**	0.924061	0.909214	0.893751	0.877957	0.877654	0.870852	0.876936	0.874378	0.863902	0.855386
0.89296	0.91204	0.916684	0.924061	**1**	0.972246	0.954709	0.934055	0.936716	0.926056	0.931709	0.925591	0.916758	0.908353
0.874651	0.905106	0.900609	0.909214	0.972246	**1**	0.976389	0.958502	0.957302	0.948917	0.955293	0.950121	0.938326	0.9248
0.861623	0.889712	0.883833	0.893751	0.954709	0.976389	**1**	0.978263	0.979993	0.968274	0.972713	0.964452	0.956232	0.943296
0.844928	0.874507	0.867516	0.877957	0.934055	0.958502	0.978263	**1**	0.998069	0.989734	0.986769	0.975647	0.964999	0.955946
0.846568	0.875095	0.86836	0.877654	0.936716	0.957302	0.979993	0.998069	**1**	0.988224	0.987975	0.977332	0.970866	0.959501
0.838725	0.866261	0.86015	0.870852	0.926056	0.948917	0.968274	0.989734	0.988224	**1**	0.996082	0.983157	0.972004	0.96628
0.844613	0.875153	0.865726	0.876936	0.931709	0.955293	0.972713	0.986769	0.987975	0.996082	**1**	0.989209	0.979145	0.968534
0.840371	0.874517	0.860531	0.874378	0.925591	0.950121	0.964452	0.975647	0.977332	0.983157	0.989209	**1**	0.988916	0.976905
0.832667	0.866397	0.85124	0.863902	0.916758	0.938326	0.956232	0.964999	0.970866	0.972004	0.979145	0.988916	**1**	0.986656
0.825572	0.85237	0.840885	0.855386	0.908353	0.9248	0.943296	0.955946	0.959501	0.96628	0.968534	0.976905	0.986656	**1**

Figure 26: Extract of similarity array between successive time ranges, where both environmental and operational conditions remain unchanged, and no damage is introduced (case 1)

The number of similar WTMM decay lines between successive time ranges, between cases 2 to 11 and case 1, which is used as the initial intact state, under pink-noise excitation and constant temperature condition, are obtained using the NCC principle as described in section 5.5. The number of similar WTMM decay lines, the so-called Successive WTMM Decay line Similarity (SDS) number, for each pair of successive time ranges is given in table 4. It should be noted that for this application of the Damage Detection methodology, the DPS number is set to 20 and the DIS number to 14.

In table 4, the changes in the time-domain range for cases 1, 2, 4 and 5 compared to the previous time range which is case 1, is not due to the presence of damage as the SDS number for these cases is greater than the DPS number. It is also obvious that the change in the time range for cases 7, 8, 9 and 11 compared to the previous time range which is case 1 is due to the introduction of damage in the current time range, as the SDS number for these cases is less than the DIS number. However, the SDS number between the time ranges of cases 3, 6 and 10 compared to case 1 is between the DIS and the DPS number, indicating that the change is either due to the presence of damage or due to change in force realisation and/or forcing condition. In this case, where a decision about damage existence cannot be made from the similarity between the WTMM decay lines, the method based on the Difference of the Pointwise Summation of Similar WTMM decay lines ($DSSD$), as described in section

5.4 is used to identify changes in the WTMM decay lines due to the presence of damage, to changes due to different force realisations and/or varying operational conditions.

Table 4: Number of similar WTMM decay lines between successive time ranges for specified cases

Previous time range	Current time range	SDS number
Case 01	Case 01	98
Case 01	Case 02	21
Case 01	Case 03	**16**
Case 01	Case 04	43
Case 01	Case 05	22
Case 01	Case 06	**15**
Case 01	Case 07	12
Case 01	Case 08	4
Case 01	Case 09	8
Case 01	Case 10	**17**
Case 01	Case 11	12

The mean value of the $DSSD$ ($meanDSSD$) for the first half of the WTMM decay line for a current time range of case 3 to a previous time range of case 1, is 2.08 ($meanDSSD_{1^{st}}$ = 2.08), whereas for the second half of the WTMM decay line is 0.30 ($meanDSSD_{2^{nd}}$ = 0.30). Similarly, the mean value of the $DSSD$ for the first half of the WTMM decay line for a current time range of case 6 to a previous time range of case 1, is 2.30 ($meanDSSD_{1^{st}}$ = 2.30), whereas for the second half of the WTMM decay line is 0.85 ($meanDSSD_{2^{nd}}$ = 0.85). The $DSSD$ values for both of these cases, indicate that the mean distance between the maximum in length WTMM decay line with the reference one is increased significantly in the first half of the decay line compared to the second half, as can be seen in figures 27 (a) and (b). This indicates that the resulting SDS number for these cases is due to changes in the force realisation and/or forcing conditions and not due to the presence of damage.

However, the mean value of the $DSSD$ for the first half of the WTMM decay line for a current time range of case 10 to a previous time range of case 1, is 0.21 ($meanDSSD_{1^{st}}$ = 0.21), whereas for the second half of the WTMM decay line is 0.29 ($meanDSSD_{2^{nd}}$ =

0.29). This indicates that the mean distance between the maximum length WTMM decay line with the reference one in the first half of the decay line is slightly less than that in the second half, as it can be seen in figure 27 (c). As the value of $meanDSSD_{1^{st}}$ is not increased compared to that of $meanDSSD_{2^{nd}}$, this indicates that the resulting SDS number for this case is due to the presence of damage.

The simulation system was also tested with the same excitation forcing acting on all three masses simultaneously, while the stiffness of spring k_1 for the damaged cases (cases 7 to 11) is gradually reduced from 450 N/m to 45 N/m. These results are presented in the following section.

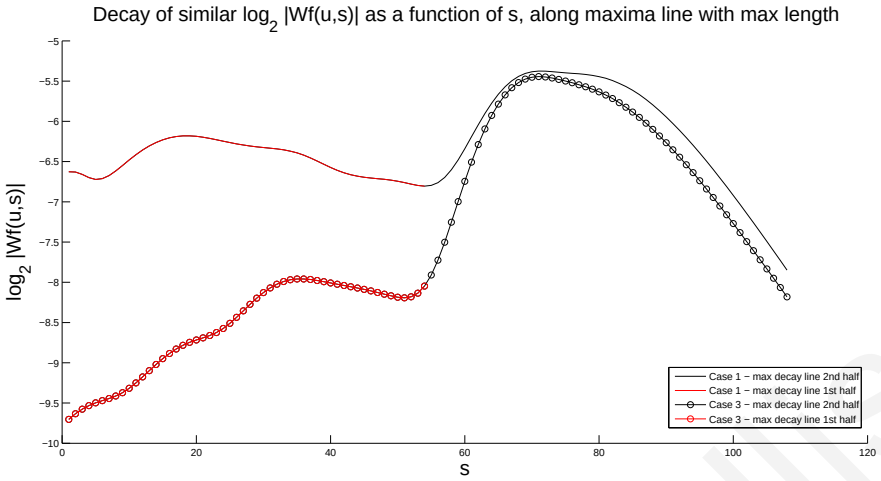

(a) Distance between max length DL of case 3 to 1

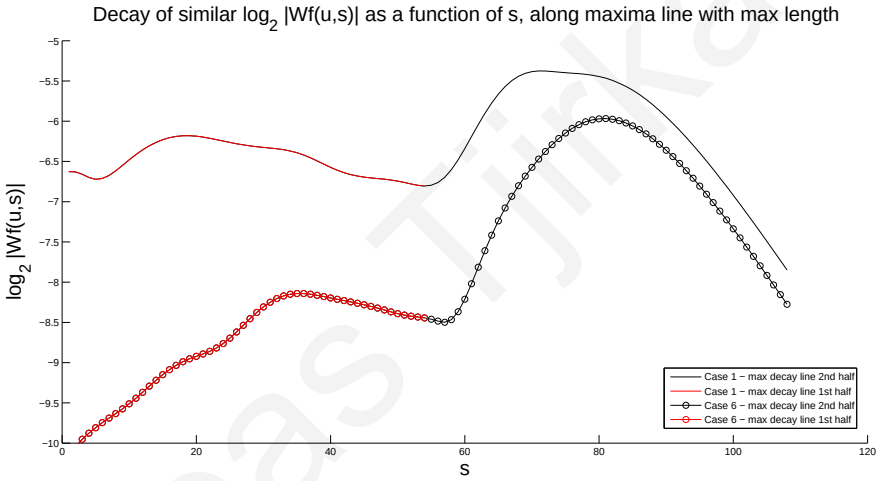

(b) Distance between max length DL of case 6 to 1

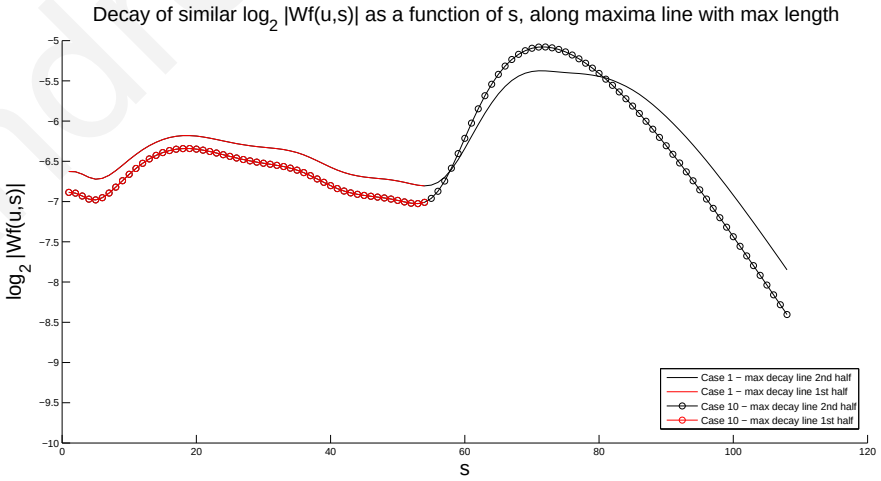

(c) Distance between max length DL of case 10 to 1

Figure 27: Distance between max length WTMM DL of (a) case 3 to 1, (b) case 6 to 1 and (c) case 10 to 1, with (a) $meanDSSD_{1^{st}} = 2.08$, $meanDSSD_{2^{nd}} = 0.30$, (b) $meanDSSD_{1^{st}} = 2.30$, $meanDSSD_{2^{nd}} = 0.85$ and (c) $meanDSSD_{1^{st}} = 0.21$, $meanDSSD_{2^{nd}} = 0.29$

6.3 Simulation System Results when excitation force is acting on all three masses

The simulation system was also tested with the same excitation force acting on all three masses simultaneously. The time response of mass 1 with its corresponding CWT, WTMM and their decay lines under the different operational and environmental conditions given in table 3 are obtained and the proposed Damage Detection methodology is employed.

The number of samples in each time range is set to 4000, the DLL threshold value to 40, and the STV value to 0.99997, as was with the case when the excitation force was acting on mass 1 only, and the number of similar WTMM decay lines between successive time ranges, between cases 2 to 11 and case 1 are obtained using the NCC principle as described in section 5.5. The SDS number, for each pair of successive time ranges and for different stiffness values of spring k_1, simulating different crack sizes, are given in table 5. It should be noted that for better efficiency in this application the DPS number was set to 37 and the DIS number to 30. Similar results were obtained with different stiffness values for springs k_2, k_3 and k_4 respectively.

Table 5: Number of similar WTMM decay lines between successive time ranges for specified cases for reducing spring k_1 stiffness, simulating increasing crack size

Previous time range	Current time range	SDS No(k_1 =405 N/m)	SDS No(k_1 =315 N/m)	SDS No(k_1 =225 N/m)	SDS No(k_1 =135 N/m)	SDS No(k_1 =45 N/m)
Case 01	Case 01	100	100	100	100	100
Case 01	Case 02	39	39	39	39	39
Case 01	Case 03	39	39	39	39	39
Case 01	Case 04	53	53	53	53	53
Case 01	Case 05	38	38	38	38	38
Case 01	Case 06	**30**	**30**	**30**	**30**	**30**
Case 01	Case 07	51	**24**	4	0	0
Case 01	Case 08	**36**	**22**	4	1	0
Case 01	Case 09	**37**	**26**	9	7	1
Case 01	Case 10	50	48	**26**	2	2
Case 01	Case 11	**37**	**35**	**26**	12	0

From the results shown in table 5, and with DPS=37 and DIS=20, it can be seen that the SDS number for all the intact cases, except for case 6, is above the DPS number, indicating that no damage is present, directly using the NCC principle. For a current time range of case 6 compared to a previous time range of case 1, the $DSSD$ principle must be employed to clarify that the change is not due to the presence of damage, as can be seen in figure 28. For a stiffness reduction to 225 N/m and below, the SDS number of all the damaged cases is below the DIS number, thus the presence of damage can be identified directly using the NCC principle.

More attention needs to be given though for spring k_1 stiffness values of 405 N/m and 315 N/m. For the damaged cases with spring k_1 stiffness values of 405 N/m the presence of damage in case 10 cannot be identified until the stiffness value is reduced to 225 N/m or less, whereas in case 7, it cannot be identified until the stiffness value is reduced to 315 N/m or less. For case 8, the damage simulated by a spring k_1 stiffness value of 405 N/m can be identified by employing the $DSSD$ principle, whereas for cases 9 and 11, damage at this stiffness value cannot be identified using the $DSSD$ principle, as the damage size seems not to affect the changes as much as the variability in operational conditions, as can be seen in figure 29. For cases 9 and 11, the k_1 spring stiffness must be reduced to a value of 315 N/m to be identifiable by the proposed methodology.

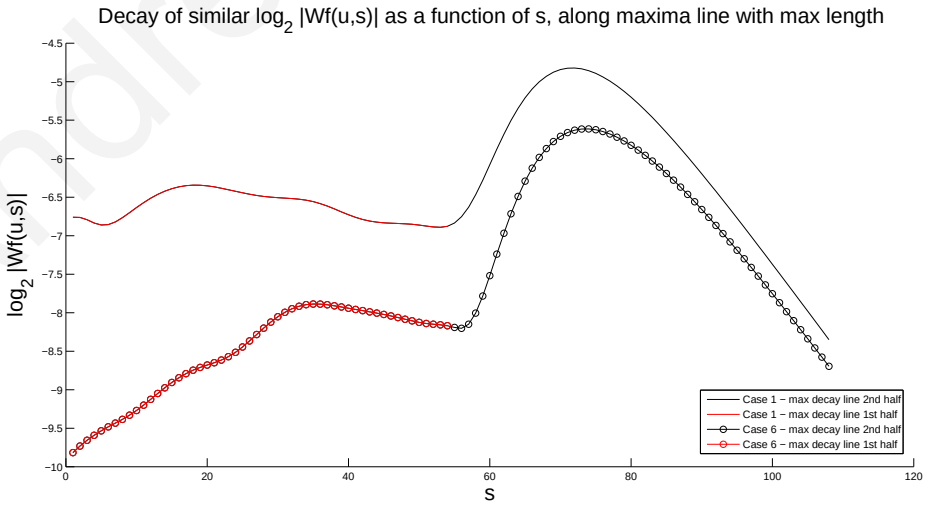

Figure 28: Distance between max length WTMM DL of case 6 to 1, with $meanDSSD_{1^{st}}$ = 1.89 and $meanDSSD_{2^{nd}}$ = 0.73

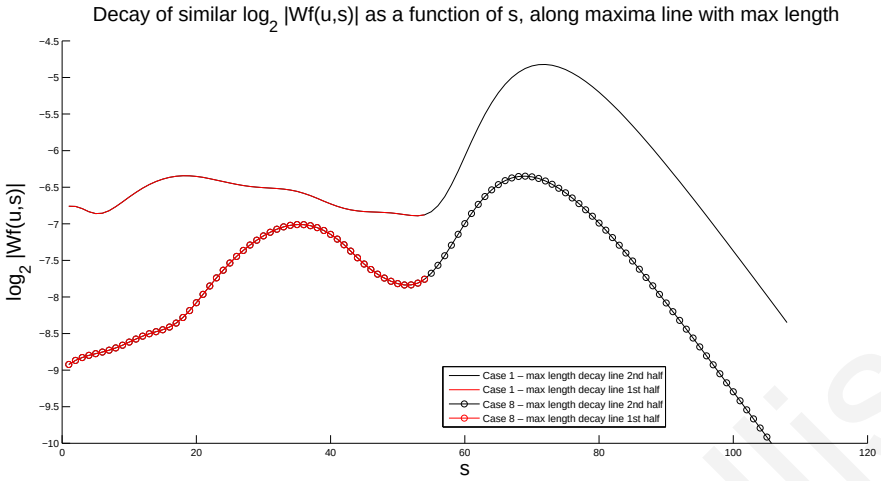

(a) Distance between max length DL of case 8 to 1

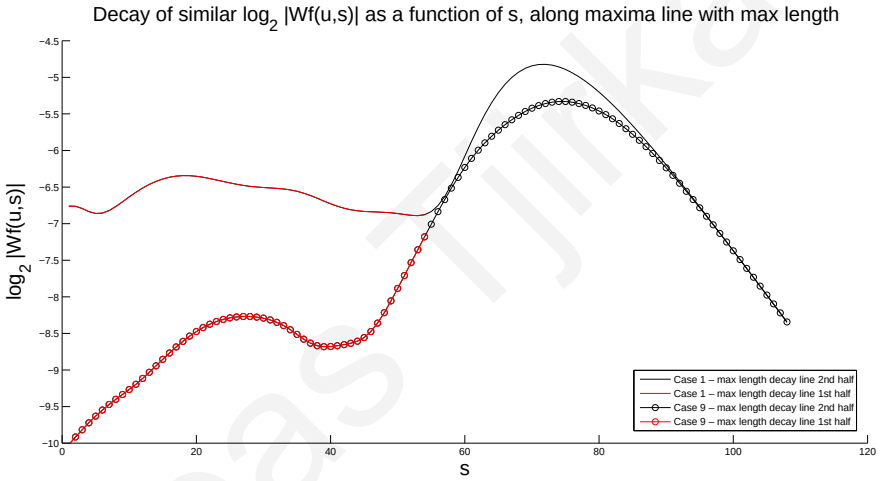

(b) Distance between max length DL of case 9 to 1

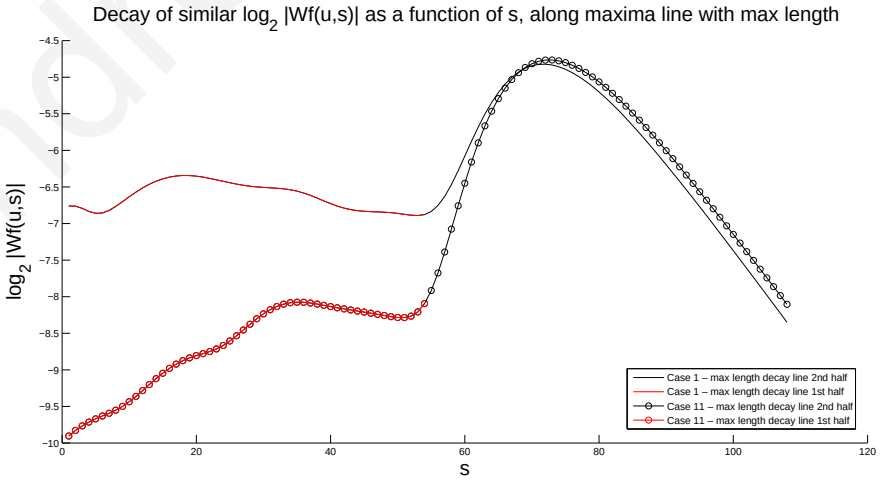

(c) Distance between max length DL of case 11 to 1

Figure 29: Distance between max length WTMM DL of (a) case 8 to 1: $meanDSSD_{1^{st}}$ = 1.23, $meanDSSD_{2^{nd}}$ = 1.62, (b) case 9 to 1: $meanDSSD_{1^{st}}$ = 2.01, $meanDSSD_{2^{nd}}$ = 0.20, (c) case 11 to 1: $meanDSSD_{1^{st}}$ = 2.05, $meanDSSD_{2^{nd}}$ = 0.22, for k_1 = 405 N/m.

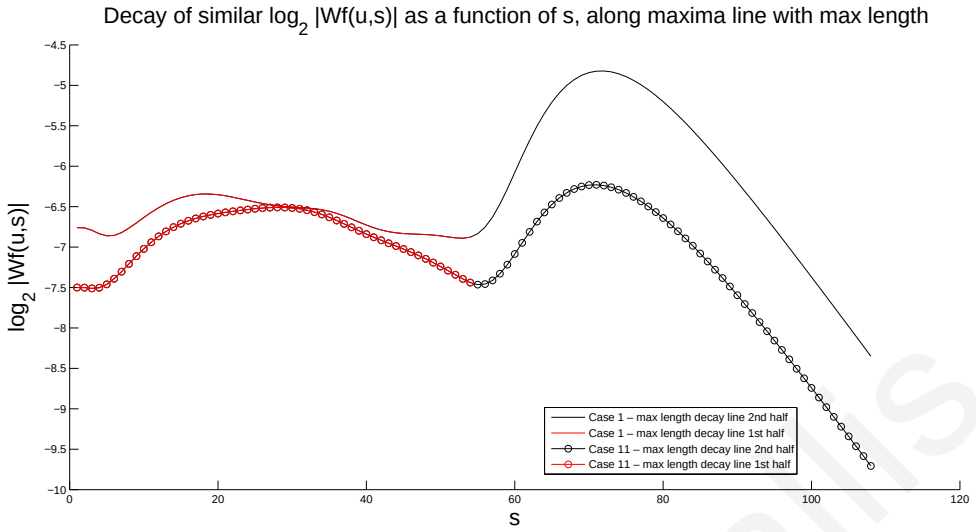

Figure 30: Distance between max length WTMM DL of case 11 to 1, for k_1 = 315 N/m and $meanDSSD_{1^{st}}$ = 0.27 and $meanDSSD_{2^{nd}}$ = 1.31

For the damaged cases with spring k_1 stiffness values of 315 N/m the presence of damage in only case 10 cannot be identified until it reaches a stiffness value of 225 N/m. For cases 7, 8 and 9 the presence of damage can be identified directly from the NCC principle, where for case 11, damage is identified by employing the $DSSD$ principle as can be seen in figure 30.

The results obtained from the simulation model, using all the possible environmental and/or forcing condition variability as well as different force realisation, both in intact and damage cases, indicate that the proposed SHM methodology, is capable of identifying the presence of damage in a time range under varying environmental and/or operational conditions. It has also been observed that, by reducing the spring stiffness gradually from 450 N/m to 45 N/m, the proposed damage detection methodology can be used effectively in monitoring the increase of a damage order in a system until a predefined damage tolerance limit is reached. However, for the proposed methodology to be used effectively in damage identification, the spring stiffness must be reduced to a value of 315 N/m or less. This enables the system to operate safely until the damage order reaches the damage tolerance limit, where the system must stop its operation for the necessary repairs or replacements to be done. In chapter 7, the SHM methodology is applied to experimental data, to verify its ability in identifying the presence of damage in real life operations.

6.4 Summary

The proposed damage detection methodology was employed on the time response measurements of a 3DOF mass spring damper simulation system, excited by both a pink and white noise force, acting either on one of the three masses or on all three masses simultaneously. The forcing realisation was also changed during the procedure. The system was simulated under 11 cases covering a number of environmental and/or operational condition variability. The environmental conditions were changed by varying the temperature, which was simulated by increasing linearly all four spring stiffness gradually with respect to running time. Damages of varying crack size were investigated by reducing any one of the four spring stiffnesses from the initial / intact state value of 450 N/m gradually to 45 N/m. The proposed Damage Detection methodology proved effective in identifying damage into the system at any time range during its operation, under varying temperature (environmental) and/or operational conditions.

Chapter 7

Experimental Cantilever Beam and Results

The experimental setup with the resulting time response signals, their corresponding CWT, WTMM and their decay lines of the cantilever beam operating under varying temperature and/or operational conditions, in initial/intact as well as damaged states is presented. The proposed Damage Detection methodology, described in section 5.5, is employed to investigate its effectiveness in determining the healthy state of the cantilever beam vibrating under varying environmental and/or operational conditions.

7.1 Experimental Setup

A cantilever beam made up of steel with specifications shown in Table 6, in a vertical arrangement, is excited both under a white and pink noise excitation force generated in Labview® [112]. The beam is excited by an LDS V201 permanent magnet shaker ® [110], which is connected to the beam via a stringer rod to minimize the interaction between the shaker and the structure, as can be seen in figure 31.

Table 6: Steel Beam Specifications

Length (l): 592 mm	Density (ρ): 7.87x10^{-6} kg/mm^3
Width (b): 30 mm	Young Modulus (E): 200x10^6 mN/mm^2
Thickness (t): 1.5 mm	Second moment of area (I): 8.44 mm^4

(a) Experimental Setup

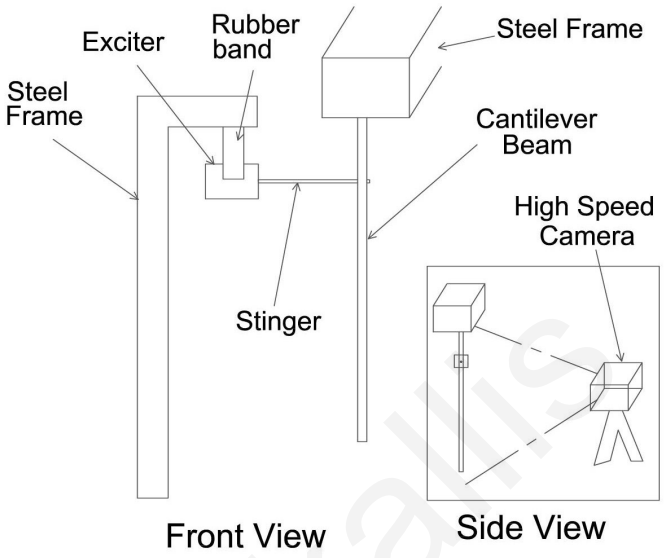

(b) Experimental Setup Schematic

Figure 31: Cantilever beam experimental setup

The beam is fixed on one end, using a steel frame, and the electrodynamic exciter is attached on a steel frame fixed on the side of the cantilever. The stinger is attached to the beam, at a distance of 119 mm from the fixed end of the beam.

The natural frequencies of the cantilever beam are obtained theoretically using equation 48, and by using Finite Element Analysis in Matlab, using the specifications given in table 6. The results of both are summarized in table 7.

$$\omega_n = 2\pi f = k_n^2 \sqrt{\frac{EI}{\rho A L}} \qquad\qquad f = \frac{k_n^2}{2\pi} \sqrt{\frac{EI}{\rho A L}} \tag{48}$$

where k_n = 1.875, 4.694, 7.855, 10.996, 14.137, 17.279

It should be noted that for the Finite Element Analysis calculations, 60 elements for the length of the beam have been used.

Table 7: Theoretical natural frequencies of the cantilever beam

	Mode 1	Mode 2	Mode 3	Mode 4	Mode 5
Theoretical freq (Hz)	3.4	21.8	61.2	119.9	198.1
Finite Element freq (Hz)	3	22	61	120	198

A crack of depth (d), width (b) and opening (e) is introduced at a distance of 452 mm from the fixed end of the beam, as can be seen in figure 32. Both the width and the opening of the crack are kept constant throughout the experimental procedure with values of b = 30 mm, and e = 2 mm respectively, while the crack depth d is varied, indicating a progressive increase in crack size.

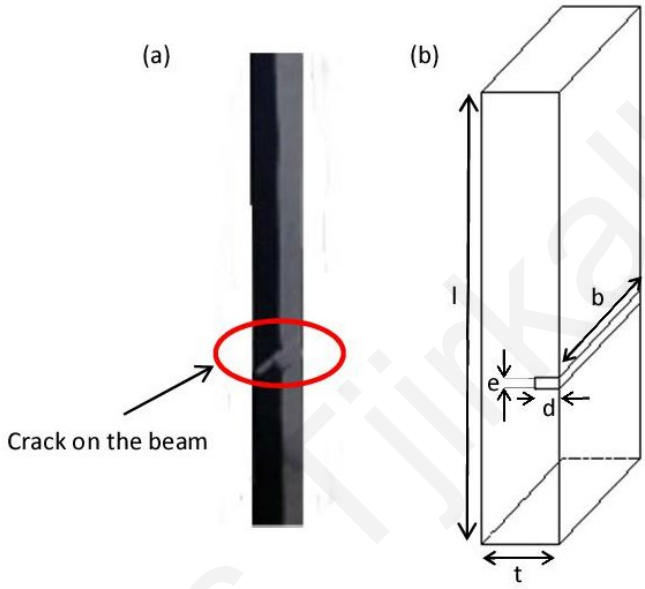

Figure 32: (a) Crack on the cantilever beam, (b) Schematic of the crack of depth d, width b and opening e

In order to be able to measure the time response at a number of required points (more than 15 points) along the length of the beam simultaneously, the vibrating response of the cantilever beam is measured using Mega Speed MS70K MDG2 High Speed Camera [86], recording and analysing monochromatic images with grayscale values. The high speed camera used has a maximum resolution of 504 x 504 pixels, frame rates of up to 100,000 FPS and a shutter speed in the range of $1\mu s$ to $30ms$ [86]. The time responses obtained using images acquisition have been verified using an accelerometer attached on the cantilever beam, at a distance of 402 mm from the fixed end of the beam. The accelerometer used is an $Omega\ ACC103$ model, with a frequency response of 1 Hz to 10 kHz, an amplitude range of $\pm$500g peak and a temperature range between -50 to 120^oC [113].

To avoid further complications in the capturing process, the lighting conditions are ensured to be adequate and constant across the length of the cantilever beam. Also, the camera is positioned so that the cantilever is at the middle of the lens and at right angles in the plane

on which the edge of the beam lies. The image size was set to 504x504 pixels so as to capture the whole of the structure. A frame captured is shown in figure 33 (a). It should be noted, that the image capture was rotated by 90^o, for convenience, and the edge used for the tracking procedure, is the top edge of the cantilever beam.

Edge detection is used to produce an accurate representation of the state of a vibrating structure at a specific point in time. The detected edges in the image plane are the boundaries of the vibrating structures, called contours. The edges can be located by searching for such discontinuities in the image using wavelet transform edge detection as suggested in [10]. This edge detection methodology is employed for each of the captured frames in the image sequence, resulting in the formation of contours of the images, as it is shown in figure 33 (b).

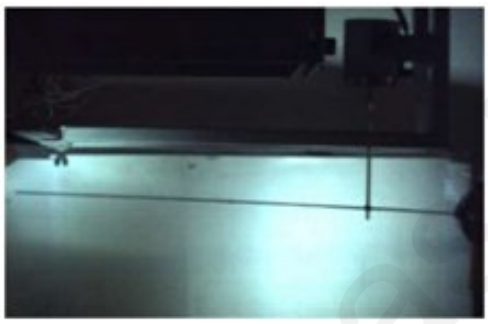

(a) frame capture

(b) edge contour

Figure 33: (a) Cantilever beam typical frame capture and (b) its corresponding edge contour.

In this thesis, the motion of the vibrating structure is confined in the 2D space, with the third dimension being time. The changes in the response of the structure with respect to time can be obtained from the displacement of the edge contours across the frames. An illustration of the image sequence analysis used in the thesis is shown in figure 34.

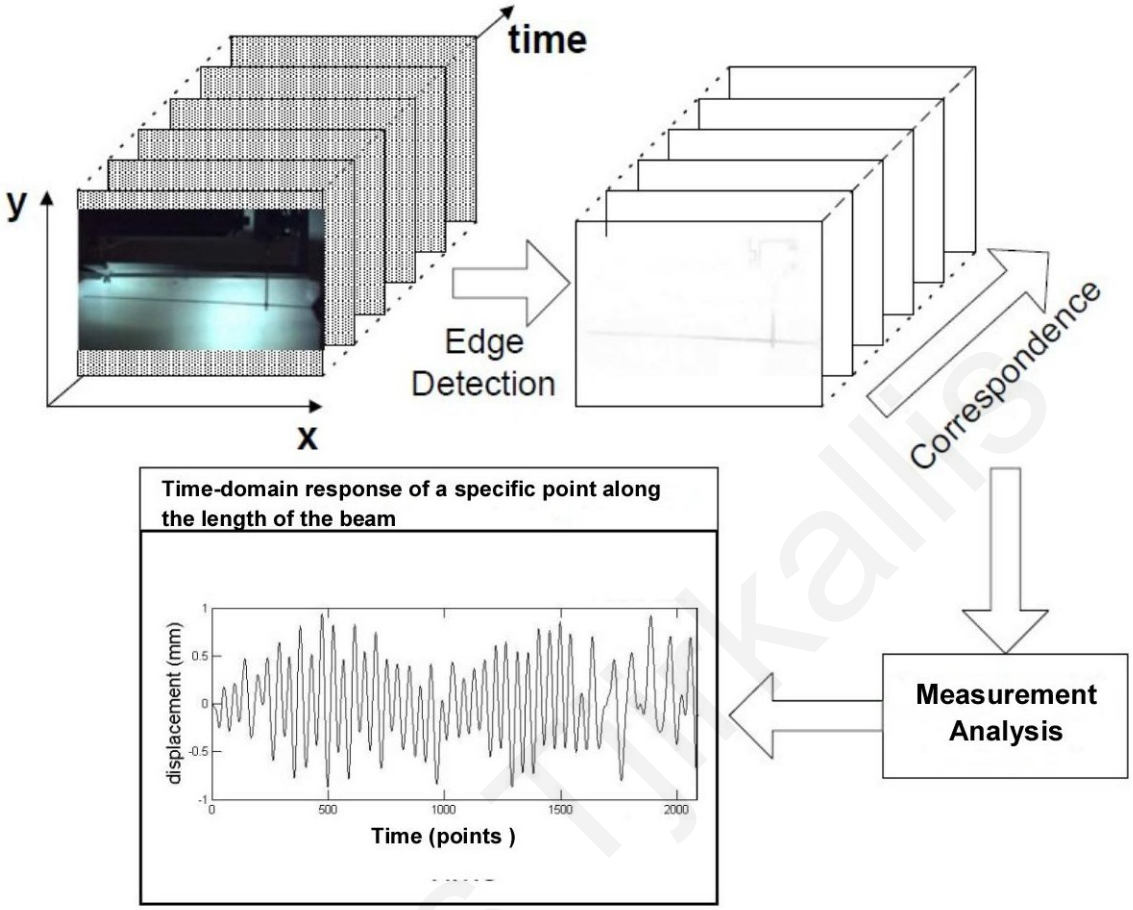

Figure 34: Image sequence analysis process

In order to obtain the time responses at each pixel along the length of the cantilever beam, a conversion of the measurements from pixels to real world units, and a line tracking algorithm resulting in the displacement of the cantilever beam from image sequence, described in sections 7.2 and 7.3 respectively, must be employed.

7.2 Conversion of measurements from image pixels to real world units

The distances and locations in an image acquired using edge contours, are measured in pixels in the two possible directions (horizontal and vertical). In order to be able to convert the measurements from pixels to real world measurements (e.g mm or m) an object of known dimensions such as a ruler can be used to calibrate the measurements, i.e. to calculate the sensitivity of the instrument (mm per pixel).

However before the image calibration can take place, one must ensure that any image distortions are either negligible or corrected, as this would affect the accuracy of the information obtained as stated in [114].

The distortions are separated into two types, geometric and radiometrical. The geometric distortions can further be separated into two groups, (a) internal distortions, which are related to the sensor (the cameras lens) and (b) external distortions which are related to the scene characteristics. These can be corrected by camera calibration methods, details of which can be found in [115].

In this thesis, the conversion of pixels to real world measurements (mm) is achieved using both an object of known dimensions, which is the pole of the steel frame holding the beam in its place, as can be seen in figure 35, as well as the dimensions of the cantilever beam, specifications of which are given in table 6 in section 7.1, in its initial (rest) position.

Figure 35: Pixels to mm conversion using cantilever beam and object of known dimensions

Using the dimensions of the cantilever beam, its known length of 592 mm occupies 439 pixels in the acquired image, resulting in a horizontal mm to $pixels$ ratio of $\frac{592}{439}$ = 1.349 $mm/pixel$. Similarly its known thickness of 1.5 mm occupies 1 pixel in the acquired image, resulting in a vertical mm to $pixels$ ratio of $\frac{1.5}{1}$ = 1.5 $mm/pixel$.

Using the dimensions of the pole of the steel frame, its known length of 524 mm occupies 389 pixels in the acquired image, resulting in a horizontal mm to $pixels$ ratio of $\frac{524}{389}$ = 1.347 $mm/pixel$, whereas its known thickness of 20 mm occupies 15 pixel in the acquired image, resulting in a vertical mm to $pixels$ ratio of $\frac{20}{15}$ = 1.333 $mm/pixel$.

From the above, it can be observed that whether using the dimensions of the cantilever beam or that of the steel frame pole with known dimensions, the measurement conversion results are the same. However, due to the thickness of the cantilever beam, covering only 1 pixel, and also being susceptible to minor flexural bending even when at rest, the measurement conversion results obtained from the steel frame pole are considered to be more accurate and are thus used in the experimental analysis of this thesis.

The image formation and processing using wavelet transform edge detection as described in section 4.2, are employed in the image acquisition using high speed camera in recording the displacement of the experimental cantilever beam, as can be seen in the following section.

7.3 Operating Deflection Shapes and time-domain responses from image sequences

The Operating Deflection Shape (ODS) of the cantilever beam as well as the time-domain displacements of specified points along the length of the vibrating beam are obtained from the contours using a line tracking algorithm. This algorithm track lines starting from an initial specified point in the image, which for a cantilever beam, this initial point is the clamped end of the cantilever, providing the displacement of the cantilever beam as a function of the distance from the clamped end.

As stated in [41], the line-tracking algorithm is based on the fact that smooth and continuous lines in an image cannot change by more than 1 or 2 pixels. It should be noted, that for this algorithm to be usable, edge contours of high quality are required, which are achieved using the wavelet edge detection procedure.

Line-tracking algorithm

The line-tracking method used, requires a starting point, which for the cantilever beam, used in this thesis, this is the clamped-end of the beam. It then moves to the adjacent column, searching for the closest edge point, that is by comparing the pixel one row up $y - 1$, with the pixel on the same row y, and one row down $y + 1$, as can be seen in figure 36, in a decision making process.

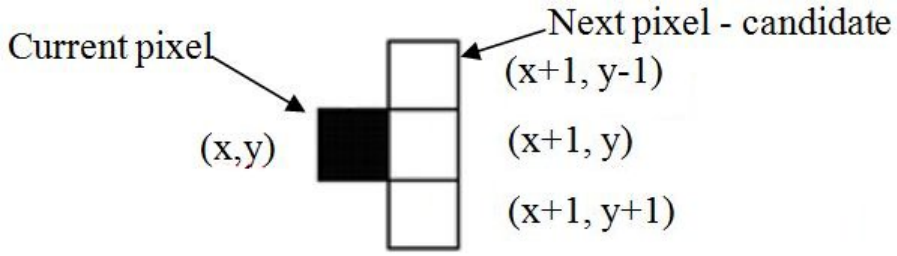

Figure 36: Decision making process of line tracking algorithm for pixels.

Once the pixel in the next column in obtained, this is marked as the new point, from which the decision algorithm is repeated, until the end of a line is reached. It should be noted that in this thesis, since the end of the line - which is the free-end of the cantilever- is known, this is specified in the algorithm, thus avoiding the problem of possible gaps in the edge line.

The column (x-direction) number of the free-end of the beam, is checked in the first and last images in a sequence, to verify that the image acquisition system remains in its position with respect to the vibrating structure throughout the recording procedure.

The decision making process of the line tracking algorithm based on the comparison of the 3 adjacent rows of each adjacent column is clarified using figure 37 below.

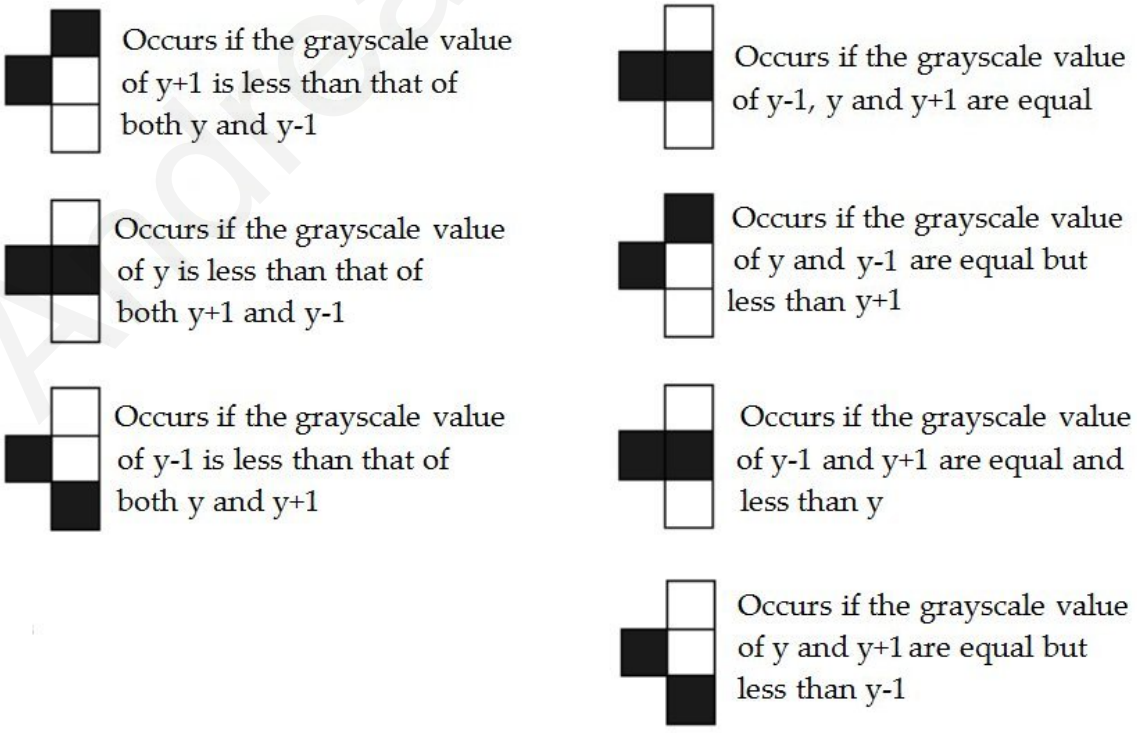

Figure 37: Schematic of the decision making process of the line tracking algorithm.

For case 1 on the left side of figure 37, the grayscale value of the pixel in the adjacent column one row up $y + 1$ is less than that of both the same row y and one row down $y - 1$, thus it is marked as the next point in the line tracking algorithm. Similarly in case 2, the grayscale value of the pixel in the adjacent column on the same row y is less than that of both one row up $y + 1$ and one row down $y - 1$, and is thus selected, whereas case 3, the grayscale value of the pixel in the adjacent column one row down $y - 1$ is less than that of both the same row y and one row up $y + 1$.

For case 4 (the 1^{st} case on the right of figure 37), the grayscale value of all 3 pixels of one row up $y - 1$, of the same row y and one row down $y + 1$ of the adjacent column are equal, thus the pixel in the adjacent column selected is the one on the same row, that is pixel $(x + 1, y)$.

For case 5, the grayscale value of pixels in the adjacent column, on the same row y and one row up $y - 1$ are equal and less than that of one row down $y + 1$, which results in selecting the pixel in the adjacent column one row up, that is pixel $(x + 1, y - 1)$.

For case 6, the grayscale value of pixels in the adjacent column, one row up $y - 1$ and one row down $y+1$ are equal, and less than that of the same row y . In this case, the selected pixel in the adjacent column is that on the same row, that is pixel $(x + 1, y)$.

For case 7, the grayscale value of pixels in the adjacent column, on the same row y and one row down $y + 1$ are equal and less than that of one row up $y - 1$, which results in selecting the pixel in the adjacent column one row down, that is pixel $(x + 1, y + 1)$.

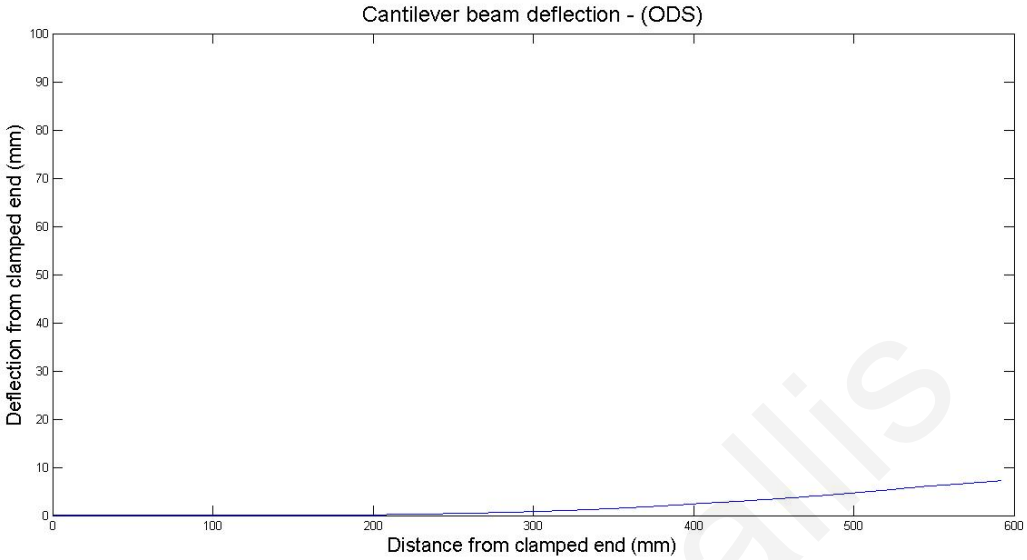

(a) Beam Deflection - ODS

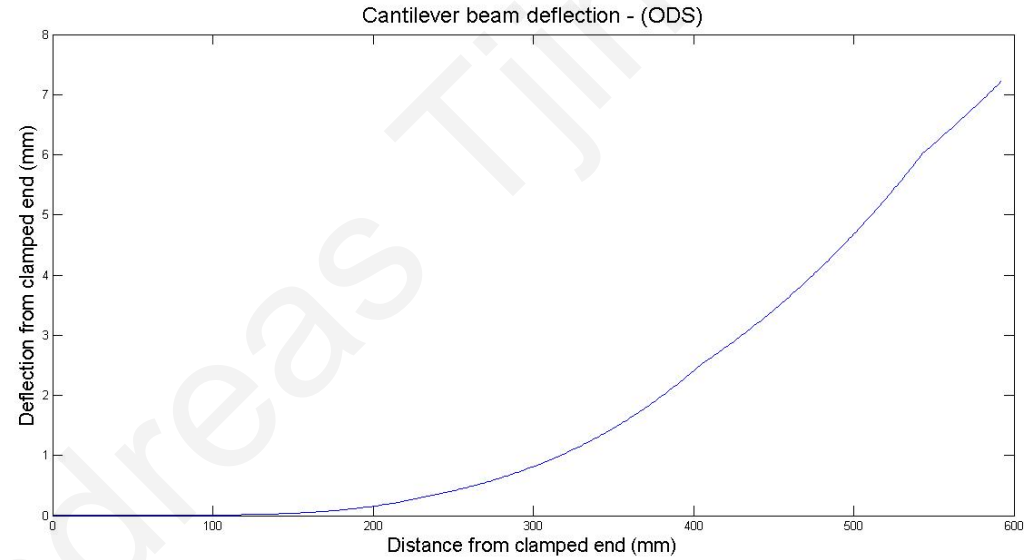

(b) Beam Deflection - ODS vertical axis zoomed

Figure 38: Cantilever beam deflection - Operating Deflection Shape (ODS) at time 0.1s, obtained using the line tracking method, with the vertical displacement (y-axis) zoomed in (b).

Using this line tracking method, a line, indicating the displacement of the cantilever beam, at each time step is obtained. A typical displacement of the vibrating structure, of the 50^{th} image, that is at time 0.1 seconds from the time the image recording process has begun, obtained using the line tracking method employed in this thesis is illustrated in figure 38.

7.4 Damage Detection Methodology and Results

The damage detection methodology as described in section 5.5 based on the wavelet transform edge detection given in section 4.5.4 and the line-tracking methodology described in section 7.3 is employed to obtain the time responses at increments of 30 pixels (≈40 mm) along the length of the beam, starting from the fixed end of the beam. Thus for the beam of length of around 600 mm, the time response of 15 points along the length of the beam are recorded and their CWT, WTMM and WTMM decay lines are computed. A typical time response for a time range of 2000 samples, with its CWT and WTMM decay lines at a distance of 300^{th} pixel (≈405 mm) from the fixed end of the cantilever beam, under constant room temperature in an intact state, operating under pink-noise force is shown in figure 39. This is considered as the initial intact state operating under constant environmental conditions, corresponding to Case 1 of table 3, shown in chapter 6. It should be noted that the WTMM decay line with the maximum length of this initial time range is stored as a reference one, to be used in the $DSSD$ principle.

The time domain responses of all the 15 points along the length of the beam are recorded continuously, while the temperature (environmental) and/or the forcing conditions are varied, with different force realisation, as well as introducing damage of different size in the beam. Damage is introduced into the beam at the location of 452 mm (≈ 335 pixel) from the fixed end of the beam, and temperature variations of around 30^oC - from 28 to 58^oC - are achieved experimentally using an electric heat gun to raise the temperature of the beam. This variation was recorded using Flir Systems InfraCam thermal camera [116]. Typical images recorded showing the temperature distribution along the length of the beam, with the beam at a constant temperature of 28^oC which is the same as the surrounding temperature, a uniform and controlled temperature variation and a non-uniform temperature variation with a maximum temperature of 58^oC can be seen in figure 40 (a), (b) and (c) respectively. It should be noted that the temperature distribution, being uniform or not, does not affect the effectiveness of the proposed Damage Detection methodology.

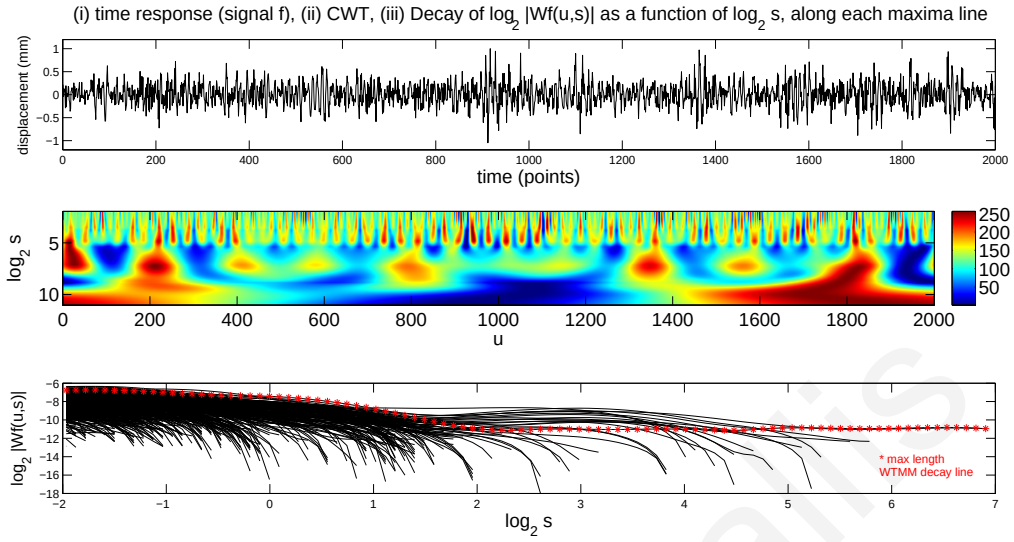

(a) Intact case Constant Temp (405mm) time response - CWT

Figure 39: Cantilever beam (i) time domain response (ii) CWT and (iii) WTMM Decay lines at location of 405 mm from fixed-end of the beam in intact state, under constant temperature conditions and pink-noise excitation force

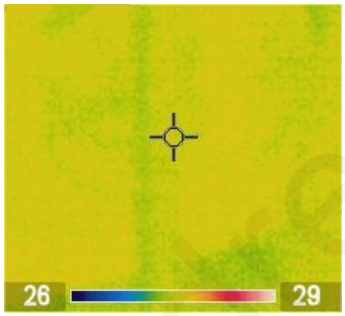

(a) Beam temperature at Surrounding temperature

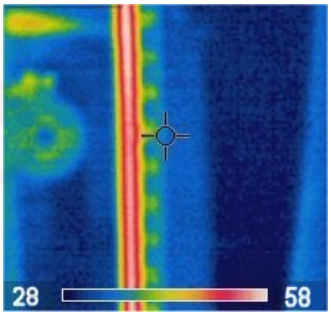

(b) Beam Temperature varies uniformly

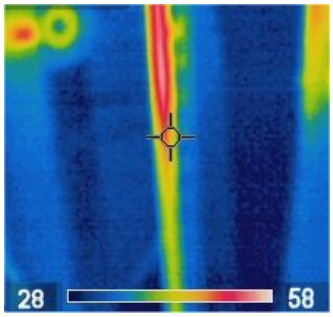

(c) Beam Temperature varies non-uniformly

Figure 40: Temperature distribution along the length of the cantilever beam, captured using thermal camera, when (a) beam is at ambient temperature, (b) the temperature along the beam varies uniformly and (c) the temperature along the beam varies non-uniformly

It is observed that the proposed Damage Detection methodology is capable to detect and identify cracks with a depth of 0.45 mm or more effectively. In order to investigate the effect of all possible combinations of varying environmental and/or forcing conditions and presence of damage, the time domain response of the beam operating under all of the 11 cases mentioned in table 3, of the simulation section, are recorded. The time-domain responses, CWT and their WTMM decay lines for cases 2, 7 and 11 at the location of a

distance of 300^{th} pixel ($\approx$405 mm) from the fixed end of the cantilever beam can be seen in figure 41, whereas for the other 7 cases can be seen in figures 52, 53 and 54 in appendix B. The crack size for the damaged cases (cases 7 up to 11) has a depth of 0.75 mm. Crack sizes of depth 0.15 mm, 0.45 mm and 1.05 mm were investigated as well. As mentioned in theory above, the time-domain responses have been normalized with the maximum value in the signal set to unity, to eliminate changes associated with variations in the amplitude of the excitation force.

As it can be seen from the plots in figure 41, neither it is possible to identify the existence of damage in the structure, nor can it be distinguished by changes due to environmental and/or force realisation and/or forcing conditions, without employing the proposed SHM methodology.

For this application the number of samples in each time range is set to 2000 samples, which has been found to be a good compromise between accuracy in the results and computational speed. The CWT, WTMM and WTMM decay lines for each time range is obtained. Using the proposed methodology as described in section 5.5, the number of similar WTMM decay lines between successive time ranges, that have a length greater than the DLL threshold value, which for this application is set to 40, is obtained. These similarity values are stored in a "Similarity array". For this application the STV value is set to 0.9997, thus if the value between any k^{th} column of the j^{th} row, containing the similarity value between the k^{th} WTMM decay line in the current time range with the j^{th} WTMM decay line in the previous time range is greater than the STV value, then the corresponding WTMM decay lines are considered to be similar. It should be noted that the WTMM decay line with the maximum length of the initial time range (Case 1) is stored as a reference one, to be used in the $DSSD$ principle.

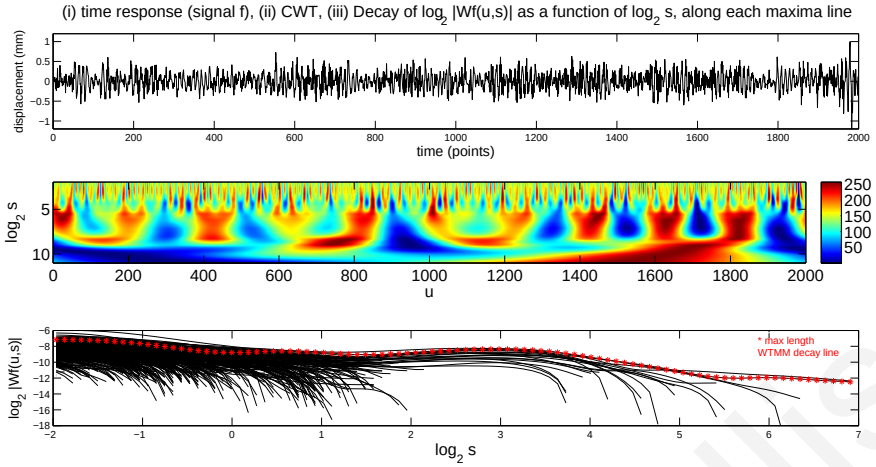

(a) (Case 2) Intact, Pink-noise Δf realisation (i) time response, (ii) CWT, (iii) WTMM decay lines

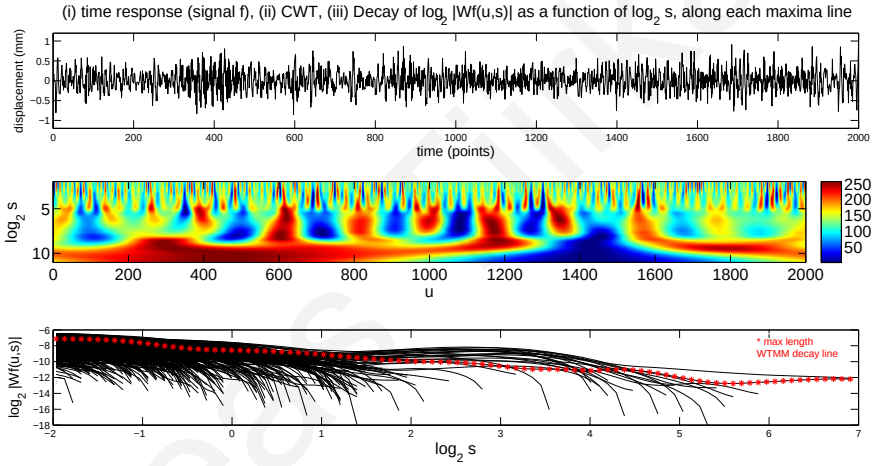

(b) (Case 7) Damaged, Pink-noise force (i) time response, (ii) CWT, (iii) WTMM decay lines

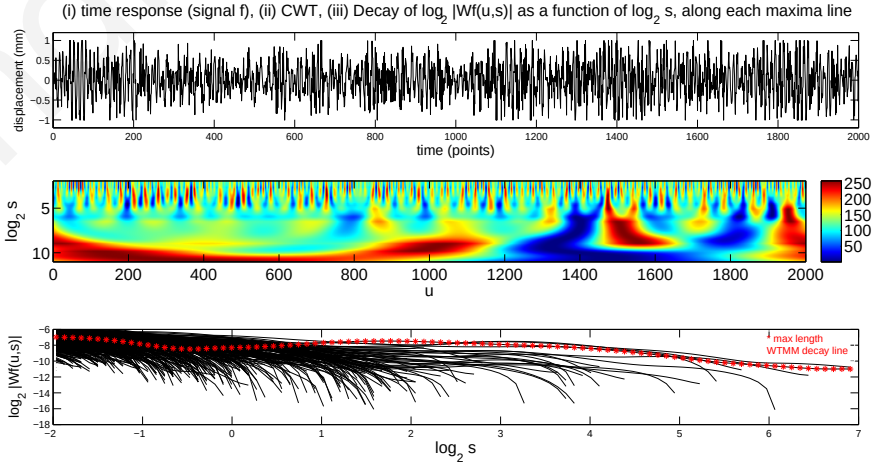

(c) (Case 11) Damaged, ΔT, White-noise force (i) time response, (ii) CWT, (iii) WTMM decay lines

Figure 41: Cantilever beam (i) time response, (ii) CWT and (iii) WTMM Decay lines at a distance of 405 mm from fixed end for cases 2, 7 and 11, with a crack size depth of 0.75 mm

The number of similar WTMM decay lines between successive time ranges, between cases 2 to 11 and case 1, which is used as the initial intact state, under constant temperature and pink-noise forcing condition is obtained using the NCC principle as described in theory. The number of similar WTMM decay lines, the so-called Successive WTMM Decay line Similarity (SDS) number for each pair of successive time ranges at six locations along the length of the beam is given in table 8. For this application of the SHM methodology, the DPS number is set to 22 and the DIS number to 14.

Table 8: Number of similar WTMM decay lines (SDS No.) between successive time ranges for specified cases along a number of locations along the length of the experimental cantilever beam, with a crack size of depth 0.75 mm

		Location along length of beam-pixels from fixed end					
Previous time range	Current time range	240 SDS No	270 SDS No	300 SDS No	330 SDS No	360 SDS No	390 SDS No
Case 01	Case 01	44	44	44	44	44	44
Case 01	Case 02	28	28	27	27	27	27
Case 01	Case 03	**20**	**20**	**20**	**17**	**17**	**14**
Case 01	Case 04	28	28	28	28	26	24
Case 01	Case 05	**20**	24	23	23	**22**	**19**
Case 01	Case 06	24	23	24	24	24	23
Case 01	Case 07	14	12	11	11	10	9
Case 01	Case 08	**20**	**20**	12	12	12	12
Case 01	Case 09	**22**	**20**	**18**	**18**	**18**	**17**
Case 01	Case 10	**19**	12	12	11	12	**14**
Case 01	Case 11	12	5	8	9	11	12

From the obtained results with a crack size of depth 0.75 mm shown in table 8, the following observations can be made:

(a) The SDS number indicating the presence of damage, does not seem to vary depending on the location along the length of the beam that the measurement is taken place with respect to the position of the damage on the structure. This does have one advantage, which is that the methodology can be used, whichever is the position of the displacement and/or

acceleration being measured on the structure, irrespective of the position that the damage is introduced. However, it does have one disadvantage as well, which is that the methodology cannot be used to locate the position of damage on the structure. A possible solution to this, is if the damage reaches the damage tolerance limit, the structure must be taken out of operation, and if the damage location is required, it must be tested under laboratory conditions, using the Wavelet Transform based Holder exponent methodology, described in section 3.4 to identify the location of damage.

(b) Regions along the length of the structure that do show sufficient displacement as are the regions which are at a distance of less than pixel 210^{th} from the fixed end of the cantilever beam, are not advisable to be used in the proposed methodology, as they will not have effective results. This can also be seen from location at 240^{th} pixel, shown in table 8, where for the damaged cases the $DSSD$ principle must be used for three out of the five cases (cases 8, 9 and 10 compared to case 1), instead of only one case (case 9 compared to 1) for locations at 300^{th}, 330^{th} and 360^{th} pixels, to distinguish changes due to the presence of damage to the ones due to environemtal and/or operational variability.

The results obtained using optical measurements, have also been verified using an experimental procedure where an accelerometer had also been used at location of 405 mm ($\approx 300^{th}$ pixel) from the fixed end of the beam. The time-domain responses, CWT and their WTMM decay lines using measurement from the accelerometer for cases 1 to 6 (intact cases) can be seen in figures 55 and 56, whereas for cases 7 to 11 (damaged cases) in figures 57 and 58 in appendix B. The SDS numbers obtaining using the proposed methodology, as can be seen in figure 9, for a crack size of 0.75 mm, are pretty much the same.

The effectiveness of the proposed damage detection methodology has also been tested on the order of the damage present, as it was the case with the simulation system. Crack sizes with a depth of 0.15mm, 0.45mm, 0.75mm and 1.05mm have been introduced at location of 452 mm ($\approx 335^{th}$ pixel) from the fixed end of the beam respectively, indicating the progressive developing of a crack size.

Table 9: Number of similar WTMM decay lines (SDS No.) between successive time ranges using optical measurement and accelerometer at location of 300^{th} pixel (≈405 mm) from fixed end of cantilever beam, with a crack size of 0.75 mm

		Location - pixel from fixed end of beam - SDS Numbers	
Previous time range	Current time range	Optical 300^{th} pixels	Accelerometer $\approx 300^{th}$ pixel
Case 01	Case 01	44	44
Case 01	Case 02	27	26
Case 01	Case 03	**17**	**17**
Case 01	Case 04	28	28
Case 01	Case 05	23	23
Case 01	Case 06	24	24
Case 01	Case 07	11	11
Case 01	Case 08	12	12
Case 01	Case 09	**18**	**18**
Case 01	Case 10	11	10
Case 01	Case 11	9	9

Since the location of the displacement or accelerometer measurement along the length of the beam with respect to the location of the damage does not affect the results of the proposed methodology, only the displacements at position of 300^{th} pixel from the fixed end of the beam are considered, the results of which are summarised in table 10.

From the results shown in table 10, and with DPS = 22 and DIS = 14, it can be seen that the SDS number for all the intact cases, except for case 3, is above the DPS number, indicating that no damage is present, directly from the use of the NCC principle. For a current time range of case 3 compared to a previous time range of case 1, the $DSSD$ principle must be employed to clarify that the change is not due to the presence of damage, as can be seen in figure 42.

Table 10: Number of similar WTMM decay lines between successive time ranges for specified cases for increasing crack size

Previous time range	Current time range	SDS No. (b=0.15mm)	SDS No. (b=0.45mm)	SDS No. (b=0.75mm)	SDS No. (b=1.05mm)
Case 01	Case 01	44	44	44	44
Case 01	Case 02	27	27	27	27
Case 01	Case 03	**17**	**17**	**17**	**17**
Case 01	Case 04	28	28	28	28
Case 01	Case 05	23	23	23	23
Case 01	Case 06	24	24	24	24
Case 01	Case 07	29	**20**	11	2
Case 01	Case 08	**21**	**19**	12	3
Case 01	Case 09	28	25	**18**	5
Case 01	Case 10	**22**	**20**	11	2
Case 01	Case 11	26	**21**	9	6

For a crack size of depth 1.05 mm ($d = 1.05$ mm) and above, the SDS number of all damaged cases is below the DIS number, thus the presence of damage can be identified directly from the use of the NCC principle, whereas for a crack size of depth 0.75 mm ($d = 0.75$ mm), the SDS number of all the damaged cases, except from case 9, is below the DIS number. For a current time range of case 9 compared to a previous time range of case 1, the $DSSD$ principle must be employed to identify whether the change is due to the presence of damage or not, as can be seen in figure 43.

For a crack size of depth 0.15 mm ($d = 0.15$ mm), the presence of damage in cases 7 and 11, cannot be identified until it reaches a depth of 0.45 mm, whereas in case 9 until it reached a depth of 0.75 mm. For cases 8 and 10, the $DSSD$ principle is employed as can be seen in figure 44 but still the effect of damage seems to be small compared to the effects of varying environmental and/or operational conditions and thus damage cannot be identified until the crack size reaches a depth of 0.45 mm.

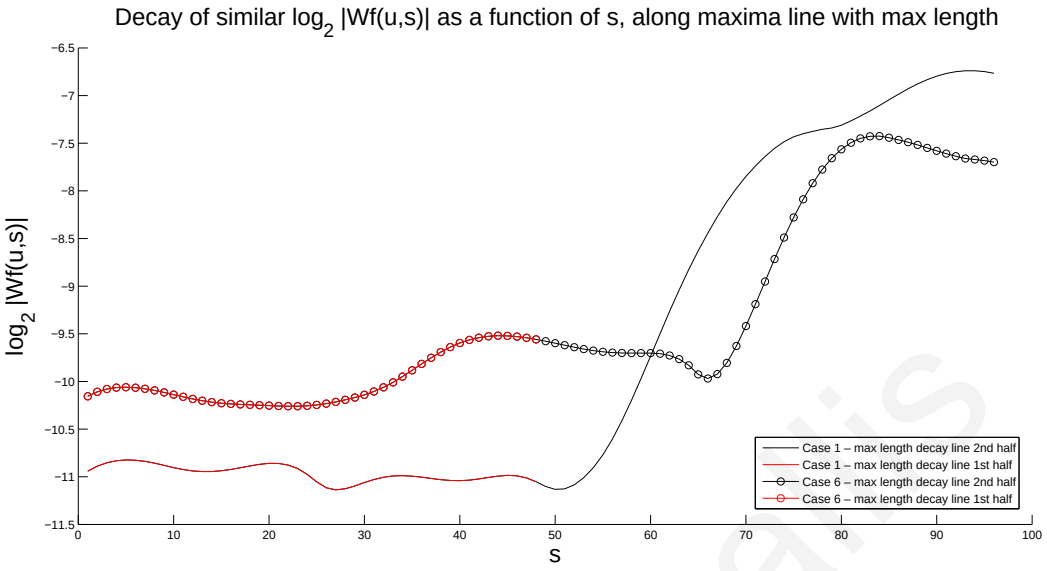

Figure 42: Distance between max length WTMM DL of case 6 to 1, with $meanDSSD_{1st}$ = 1.46 and $meanDSSD_{2nd}$ = 0.67

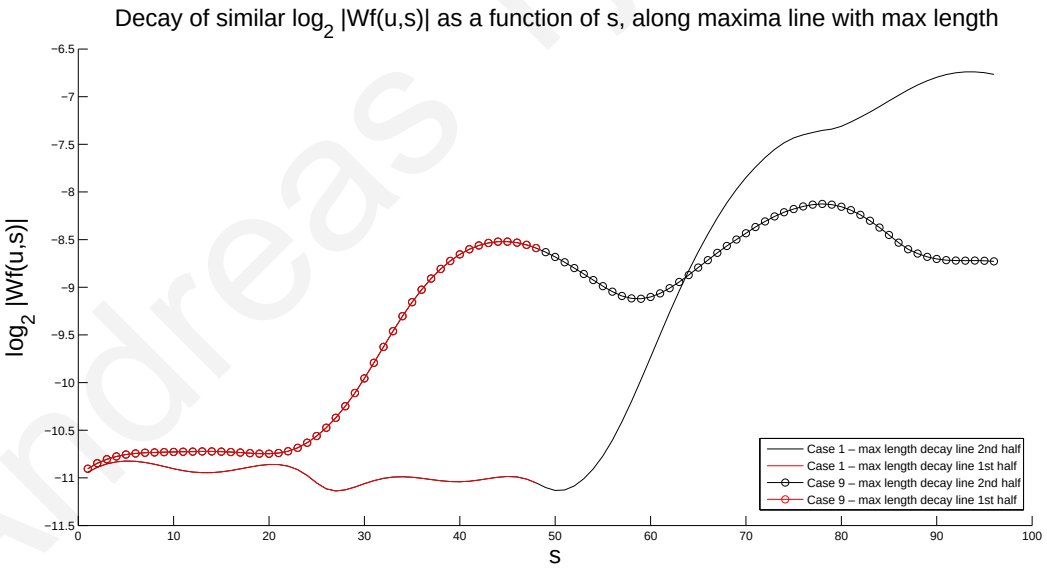

Figure 43: Distance between max length WTMM DL of case 9 to 1 for a crack size of 0.75 mm, with $meanDSSD_{1st}$ = 0.96 and $meanDSSD_{2nd}$ = 1.08

For a crack size of depth 0.45 mm ($d = 0.45$ mm), the presence of damage in all five cases cannot be identified directly from the use of the NCC principle, as the SDS number is above the DIS number but below the DPS number ($DIS < SDS < DPS$), thus the $DSSD$ principle must be employed.

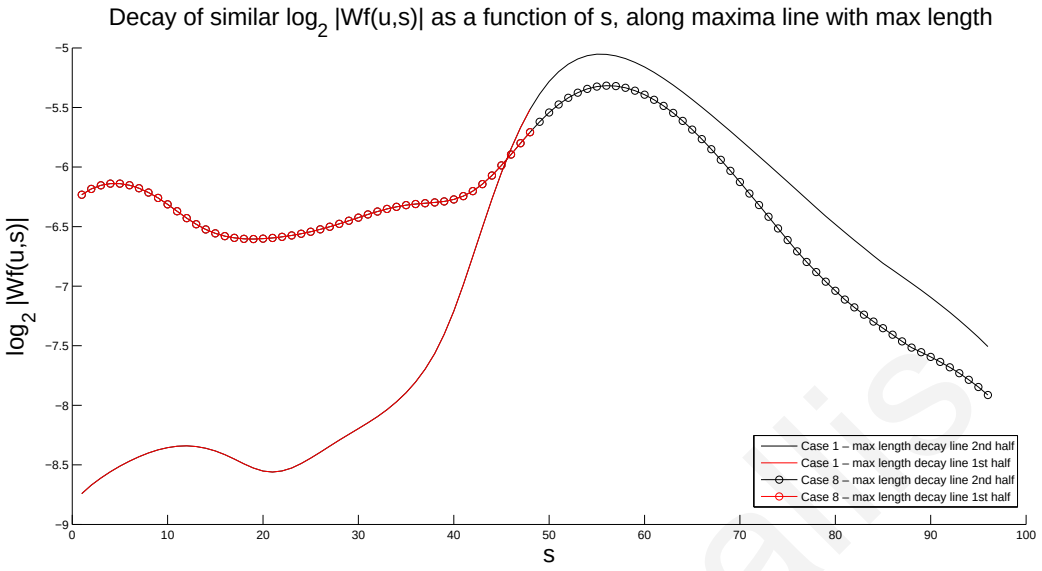

(a) Distance between max length DL of case 8 to reference

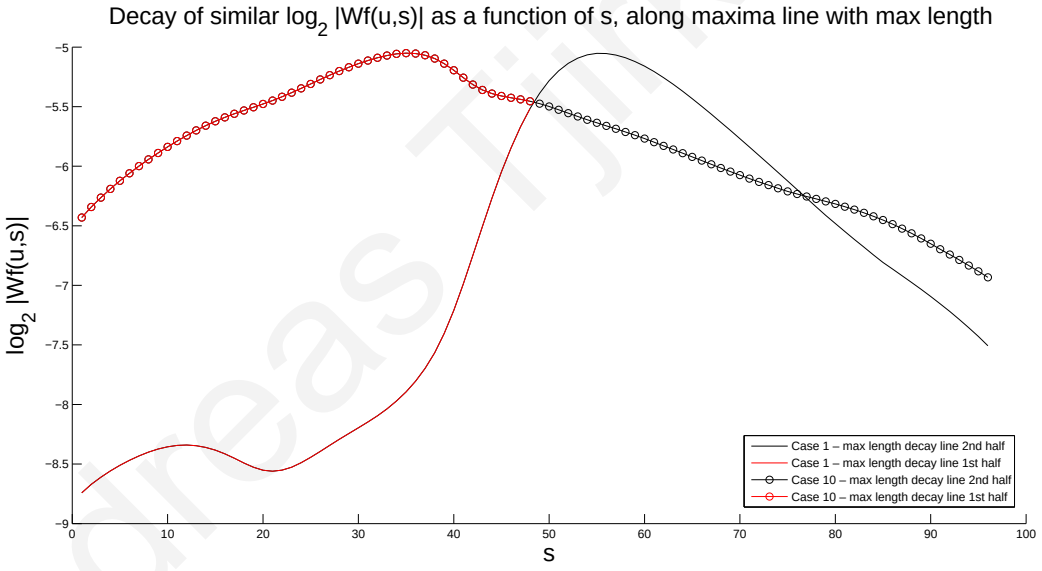

(b) Distance between max length DL of case 10 to reference

Figure 44: Distance between max length WTMM DL of case (a) 8 and (b) 10 to reference, for a crack size of 0.15 mm, with (a) $meanDSSD_{1st}$ = 2.10, and $meanDSSD_{2nd}$ = 0.14 and (b) $meanDSSD_{1st}$ = 1.69 and $meanDSSD_{2nd}$ = 0.45

From the above results, it can be concluded that for the experimental cantilever beam, the proposed damage detection methodology can be employed effectively to identify the introduction of damage in the structure under varying environmental and/or operational conditions. However, for the damage to be identifiable without false alarms the crack must propagate to a depth of at least 0.45 mm. Overall, the proposed methodology can be rendered as effective in real life structural health monitoring.

7.5 Summary

In this chapter, the theory of optical measurements using image acquisition and processing as well as wavelet transform edge detection, used as a global measurement process in measuring the time response of a cantilever beam were presented. A description of the cantilever beam setup used during the experimental procedure was also given. An electrodynamic exciter via a stinger rod attached to the beam was used to excite the beam under pink or white noise excitation, with different force realisations. Damage was introduced into the structure, by inducing a crack at a specified location from the fixed end of the beam. The crack size was gradually increased from a depth of 0.15 mm up to 1.05 mm, indicating the progressive development of the damage in the structure. The displacement along the full length of the beam is recorded using a high speed camera, while the beam is vibrating under varying environmental and/or operational conditions which are summarised in eleven different cases. The time response measurements at six equally spaced locations from the 240^{th} pixel up to the 390^{th} pixel (from $\approx$ 324 mm up to $\approx$ 526 mm) from the fixed end of the cantilever beam were obtained. The proposed Damage Detection methodology was employed on the measurements from these locations under varying operational and/or temperature (environmental) conditions. The methodology proved effective in identifying the introduction of a damage of a crack size of a depth of 0.45 mm and above, at any time range during the operation of the structure under varying environmental and/or operational conditions.

Chapter 8

Conclusions and Further Research

This chapter summarizes the research outcomes of the work described in this thesis and discusses their importance with respect to the knowledge advancement they achieved in the area of damage section under changing environmental and operational conditions.

8.1 Conclusions

The work described in this thesis was focused on the effects of varying environmental and/or operational conditions in Structural Health Monitoring (SHM). These effects pose serious challenges that any real life application of a SHM methodology should face. In the literature the process of eliminating these effects is known as $normalization$.

The damage detection methodology proposed in this thesis achieves $normalization$ by using features extracted from the Wavelet Transform Modulus Maxima (WTMM) decay lines of the Continuous Wavelet Transform (CWT) of the time responses of the structure under consideration. More specifically it has been shown that the WTMM decay lines change between time ranges depending on the variability of environmental and/or operational conditions as well as on the introduction of damage. A method was thus devised, using the principle of Normalized Cross Correlation (NCC), that can quantify the similarity of WTMM decay lines between successive time ranges. It has been observed that the number of similar WTMM decay lines between successive time ranges, referred to as a SDS number in this thesis, reduces significantly when damage is introduced into the system, while this reduction is less if it is caused by environmental and/or operational condition variability.

Furthermore, it has been observed that under certain crack sizes and varying operational and/or environmental conditions, there are cases that a decision about the existence of damage or not cannot be made using the similarity of WTMM decay line directly. To overcome this problem, a methodology which quantifies the difference in magnitude between the similar WTMM decay line with the greatest length, that is the one that extents throughout all the scales, in each time with a reference one, referred to as the Difference of the Pointwise Summation of Similar WTMM Decay lines and abbreviated by $DSSD$ was developed. The above were employed in the proposed Damage Detection methodology. The capabilities and effectiveness of the proposed methodology in identifying damage existence in a system operating under varying environmental and/or operational variability were tested using a simulation 3 DOF mass, spring, damper system and an experimental cantilever beam. The proposed methodology proved effective in identifying the introduction of damage of a crack size of a depth of 0.45 mm and above, at any time range during the operation of the structure under varying environmental and/or operational conditions.

8.2 Further Research

In this thesis it was demonstrated that WTMM decay lines can be used as an extraction feature in eliminating the effects of varying operational and/or environmental conditions, enabling the effective identification of damages in structures during real time operations. However, further investigation is required in identifying the effects of locally concentrated environmental / temperature conditions variability, and whether the proposed methodology is still capable to identify the presence of damage under this condition. Besides, further investigation is required in identifying the effects of gradual matter deposition along the surface of the system under consideration during its operation under varying environmental and/or operational conditions. Further research can also be done, in extending the proposed methodology into monitoring the healthy state of a system continuously for a number of days, while an initially induced crack is gradually propagating. This will enable the testing of the effectiveness of the proposed methodology in the continuous monitoring of a crack propagation in real life operations.

Additionally, an investigation into extending the employment of the WTMM decay lines as an extraction feature in the identification of damages directly from acquired images rather

than from signals sounds challenging but promising. This will result in 2-dimensional (2D) WTMM decay lines, and consequently in the development of a 3-dimensional (3D) Similarity Array. However, further investigations are required in obtaining the CWT, the WTMM and the WTMM decay lines in 2D directly from the acquired images, and comparing the similarity of the 2D WTMM decay lines between successive time sequences of images, using the Normalized Cross Correlation (NCC) as well as the $DSSD$ principles in 2D. This will enable the development of a 2D SHM methodology, which can possibly be a faster and/or more efficient alternative to the presented 1D SHM, in identifying the presence of damages in structures under varying operational and/or environmental conditions. It should be noted that 2D WTMM decay line has been used in multifractal analysis by Arneodo et al. in [117] and by Decoster et al. in [118].

Appendix A

Simulation 3DOF Data and Results

Here, the LabView Block Diagrams and Panels used to generate the excitation forces are shown. In addition the time domain responses of mass 1, their corresponding CWT and WTMM decay lines of the simulation system under a number of intact and damage state cases, are presented. Extracts of the ”Similarity Array” of a number of cases are also illustrated.

A.1 LabView Panel and Block Diagrams

The Labview Block Diagram that was used to generate the pink and white noise realisations which were used both in the simulation 3DOF system, and to excite the experimental cantilever beam is illustrated in figure 45. The Front panel for Pink noise generation is depicted in figure 46, while for the White noise generation in figure 47.

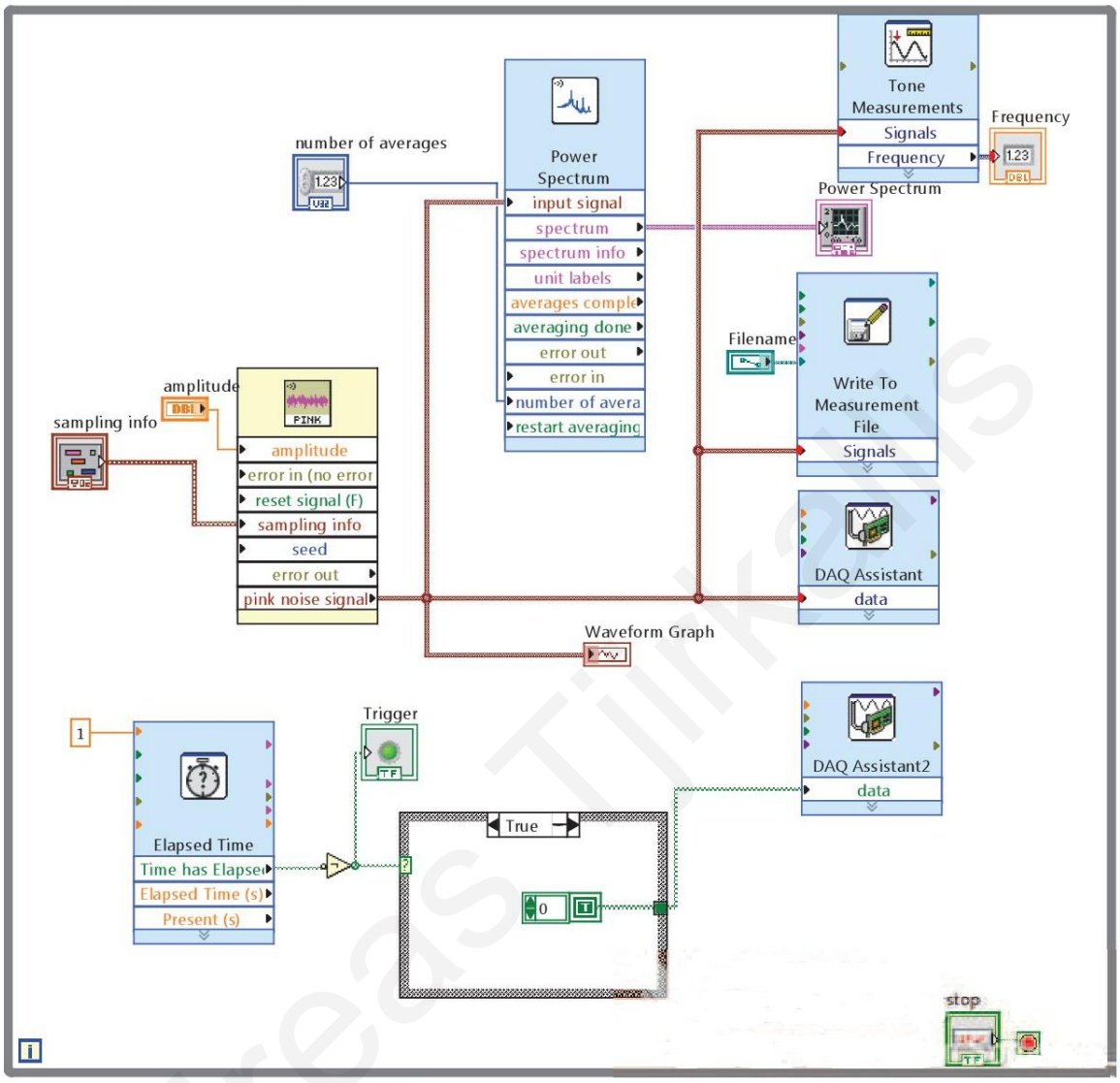

Figure 45: Labview Pink noise Block Diagram

Figure 46: Labview Pink noise Front Panel

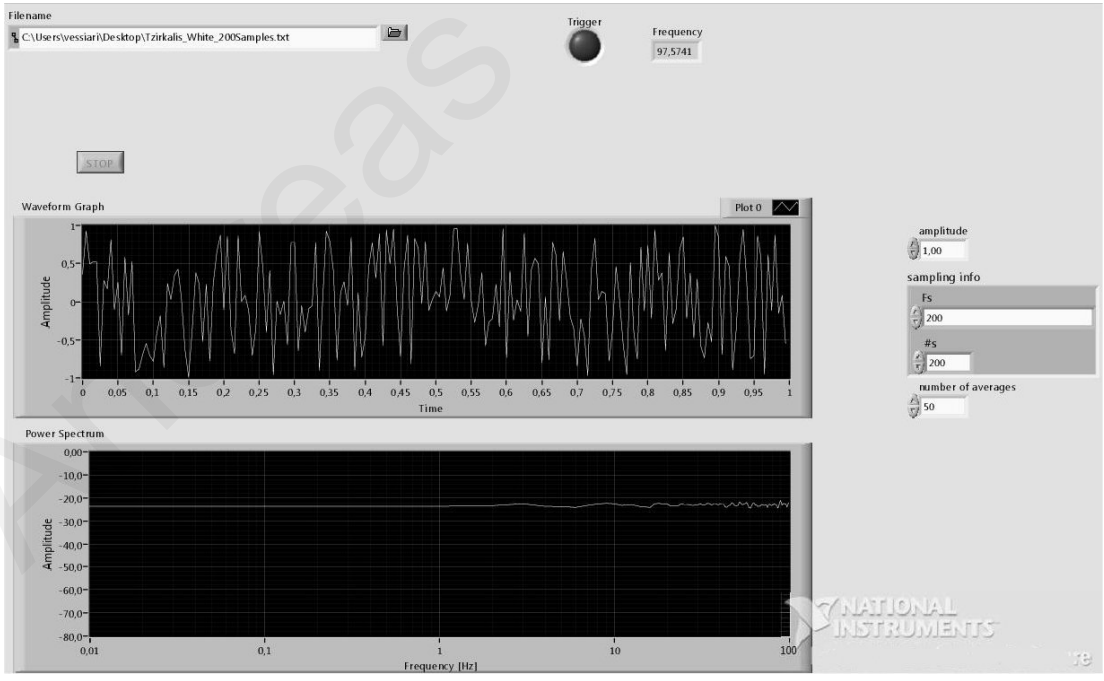

Figure 47: Labview White noise Front Panel

A.2 Simulation 3 DOF results

The time domain responses of mass 1, their corresponding CWT and WTMM decay lines of the simulation system under intact states (cases 3, 4, 5 and 6) and damage states (cases 8, 9 and 10) are shown in figures 48, 49 and 50 respectively. The damage was introduced by reducing the stiffness of spring k_1 from 450 N/m to 225 N/m. The time domain responses, their corresponding CWT and WTMM decay lines of the simulation system for cases 1, 2 are shown in figure 24 and for cases 7 and 11, in figure 25 in section 6.1.

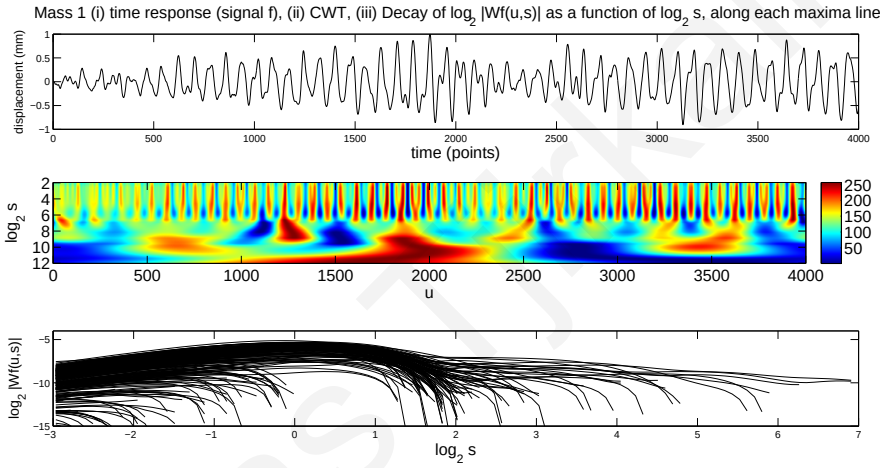

(a) (Case 3) Intact, Constant T, White-noise force (i) time response, (ii) CWT, (iii) WTMM decay lines

Figure 48: 3DOF mass 1 (i) time domain response, (ii) CWT and (iii) WTMM Decay lines for case 3 (intact case)

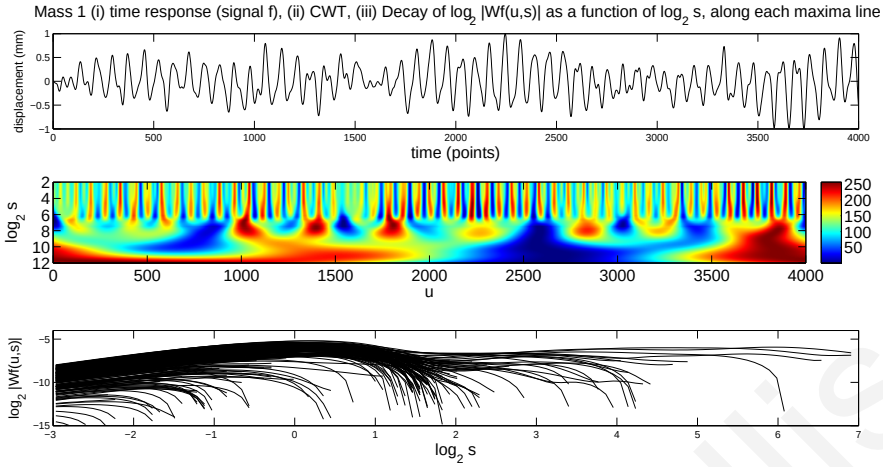

(a) (Case 4) Intact, ΔT, Pink-noise force (i) time response, (ii) CWT, (iii) WTMM decay lines

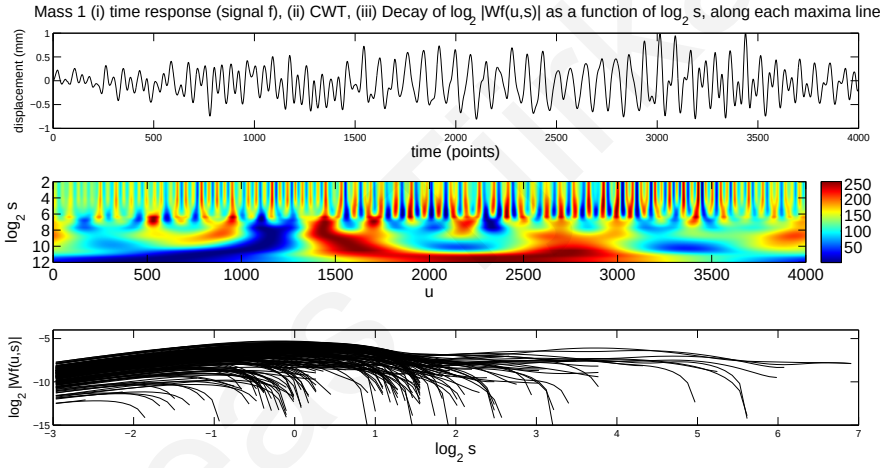

(b) (Case 5) Intact, Pink-noise Δf realisation (i) time response, (ii) CWT, (iii) WTMM decay lines

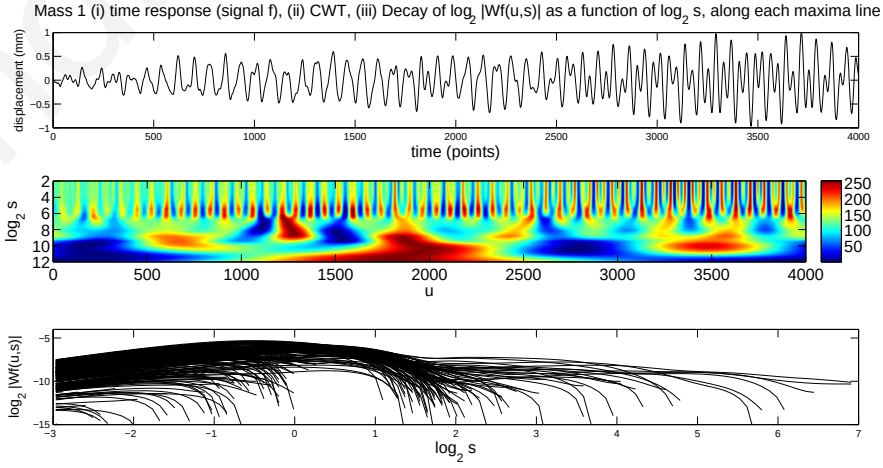

(c) (Case 6) Intact, ΔT, White-noise force (i) time response, (ii) CWT, (iii) WTMM decay lines

Figure 49: 3DOF mass 1 (i) time domain response, (ii) CWT and (iii) WTMM Decay lines for cases 4, 5 and 6 (intact cases)

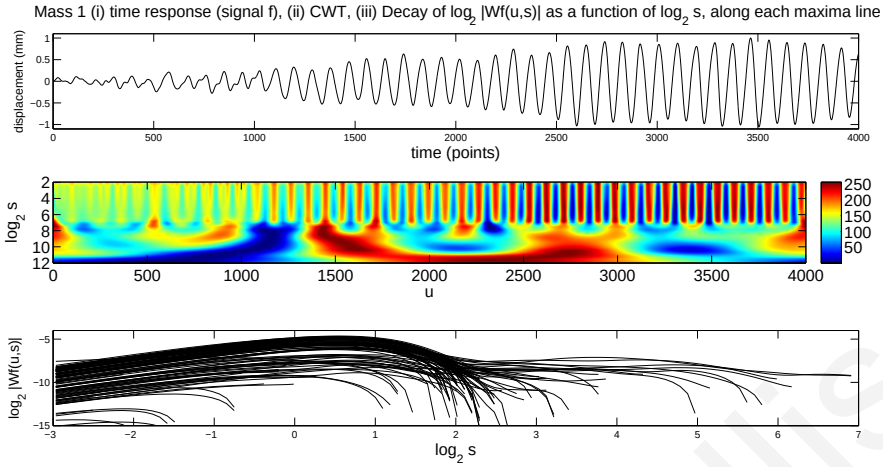

(a) (Case 8) Damaged, Pink-noise Δf realisation (i) time response, (ii) CWT, (iii) WTMM decay lines

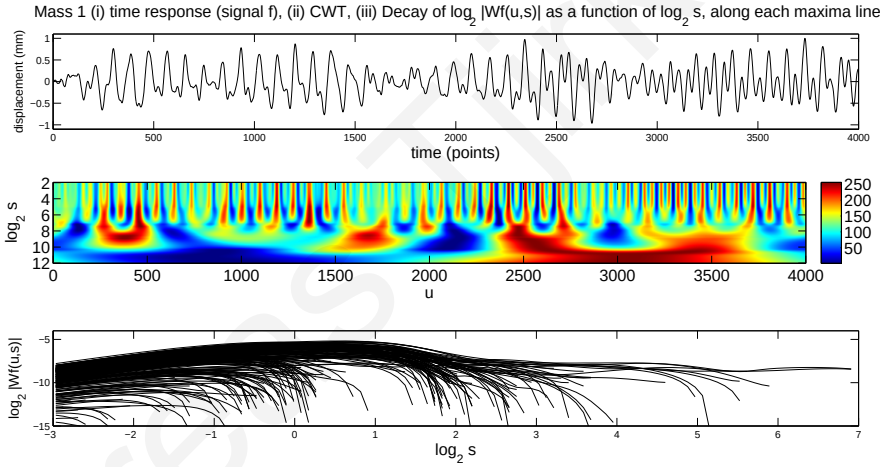

(b) (Case 9) Damaged, White-noise force (i) time response, (ii) CWT, (iii) WTMM decay lines

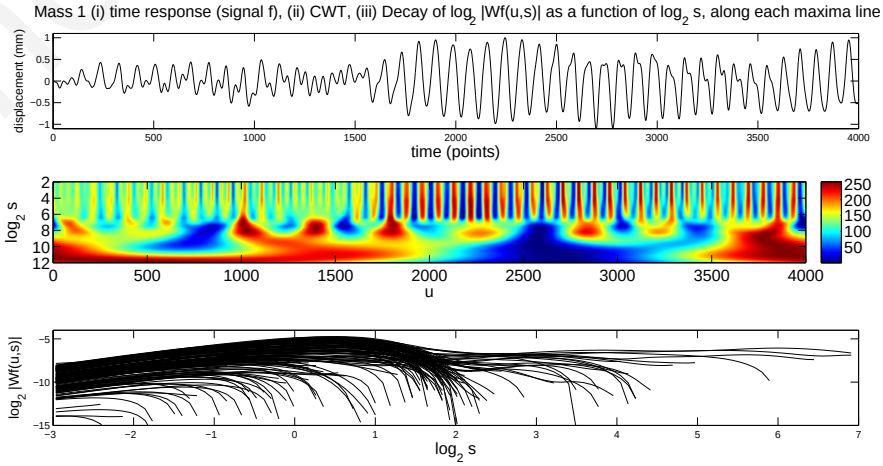

(c) (Case 10) Damaged, ΔT, Pink-noise force (i) time response, (ii) CWT, (iii) WTMM decay lines

Figure 50: 3DOF mass 1 (i) time response, (ii) CWT and (iii) WTMM Decay lines for cases 8, 9 and 10 (stiffness reduction of spring k_1 from 450 N/m to 225 N/m for damaged cases)

Extracts of the ”Similarity Array” for cases 2, 7 and 11 are shown in figure 51. As mentioned in section 5.5, each k^{th} column of the j^{th} row of these 2-dimensional arrays, contain the similarity value between the k^{th} WTMM decay line in the current time range with the j^{th} WTMM decay line in the previous time range.

0.997175	0.998759	0.951338	0.944311	0.930796	0.920495	0.898928	0.889024	0.855988	0.827406	0.821554	0.820391	0.822993	0.808621
0.990411	0.98687	0.946102	0.957849	0.940476	0.926546	0.926494	0.908109	0.884886	0.855239	0.859273	0.850595	0.854175	0.84789
0.964506	0.96698	0.974512	0.971431	0.956239	0.944715	0.926555	0.914272	0.878429	0.842396	0.839237	0.835563	0.837307	0.822099
0.925402	0.927962	0.970836	0.989659	0.988935	0.968709	0.935627	0.920928	0.88847	0.857614	0.855638	0.851671	0.8546	0.842705
0.878083	0.877201	0.918127	0.922537	0.941887	0.949083	0.977885	0.997139	0.946668	0.910418	0.900262	0.902214	0.905102	0.884681
0.865679	0.862486	0.894529	0.90978	0.921893	0.92018	0.966626	0.968891	0.970174	0.926316	0.930236	0.920061	0.921673	0.9106
0.856798	0.854183	0.888045	0.893539	0.909142	0.91134	0.94664	0.95111	0.990308	0.94487	0.940873	0.937136	0.939944	0.923405
0.844517	0.84048	0.872936	0.877508	0.897273	0.896161	0.930748	0.934728	0.987097	0.954406	0.948171	0.950674	0.94646	0.922387
0.847132	0.845169	0.882299	0.87874	0.902116	0.905301	0.929326	0.939389	0.987329	0.958614	0.95086	0.954514	0.951369	0.928441
0.840715	0.835474	0.867703	0.869778	0.890784	0.889762	0.922519	0.927241	0.978014	0.964174	0.954469	0.95958	0.95489	0.928124
0.846038	0.843466	0.876012	0.877816	0.893388	0.895677	0.930285	0.929833	0.982679	0.968605	0.960776	0.960201	0.959959	0.93531
0.840252	0.838981	0.86992	0.875262	0.884857	0.88818	0.927311	0.920431	0.974313	0.978402	0.973871	0.970385	0.972017	0.95254
0.840619	0.842805	0.878646	0.867485	0.887206	0.895593	0.917465	0.919796	0.962673	0.987624	0.980305	0.979599	0.980831	0.959875
0.83416	0.831169	0.864129	0.854713	0.875343	0.881514	0.904674	0.909212	0.951973	0.999344	0.9827	0.989832	0.989287	0.96044

(a) Extract of Similarity Array for case 2, Intact Case, Pink-noise Δf realisation. Actual Array size is 98x103.

0.99897	0.99954	0.972146	0.94848	0.8873	0.876364	0.858363	0.857878	0.840929	0.844716	0.839109	0.842149	0.839932	0.830155
0.992766	0.990944	0.974842	0.959922	0.905294	0.898145	0.880119	0.876681	0.862145	0.867467	0.867186	0.865435	0.874938	0.857321
0.969826	0.971956	0.999317	0.974971	0.910382	0.900065	0.880133	0.877459	0.860707	0.864934	0.860366	0.861171	0.860517	0.847648
0.936005	0.939552	0.963326	0.98331	0.917595	0.906443	0.886684	0.88527	0.868301	0.874412	0.869345	0.871785	0.874233	0.859709
0.889369	0.893671	0.914878	0.918743	0.992336	0.976881	0.952315	0.9529	0.931939	0.93527	0.927216	0.930184	0.924924	0.914551
0.87425	0.871637	0.901093	0.90556	0.977427	0.995033	0.969614	0.964599	0.945406	0.951707	0.947751	0.946817	0.950836	0.932434
0.861364	0.858282	0.883602	0.890104	0.959039	0.972703	0.995713	0.994495	0.973419	0.976848	0.969527	0.968528	0.963947	0.952643
0.846512	0.84088	0.868424	0.873523	0.938262	0.951061	0.97681	0.973418	0.993262	0.996658	0.988393	0.983916	0.975532	0.967931
0.845952	0.842603	0.867375	0.875108	0.940064	0.955447	0.980356	0.978648	0.996446	0.997533	0.990618	0.98549	0.976842	0.971227
0.840908	0.834684	0.861504	0.865462	0.930712	0.943086	0.97066	0.966174	0.986019	0.988497	0.997562	0.995585	0.982884	0.977643
0.846066	0.839879	0.86619	0.873484	0.935275	0.94892	0.974879	0.969027	0.982444	0.985438	0.996084	0.996763	0.98915	0.978145
0.842792	0.83499	0.860659	0.871522	0.927675	0.939661	0.964946	0.959132	0.970012	0.97301	0.983885	0.983912	**0.999819**	0.985225
0.832662	0.833335	0.849601	0.863781	0.919565	0.936311	0.962076	0.956271	0.967597	0.965395	0.978137	0.974734	0.988694	0.995586
0.827658	0.821224	0.840895	0.851231	0.91173	0.925623	0.955649	0.948553	0.962309	0.960274	0.969154	0.970428	0.976257	0.990422

(b) Extract of Similarity Array for case 7, Damaged Case, Pink-noise force. Actual Array size is 98x88.

0.997629	0.997606	0.964594	0.94773	0.933449	0.918154	0.876932	0.867566	0.861176	0.850699	0.848051	0.836506	0.838287	0.825791
0.989831	0.986545	0.953029	0.94976	0.940142	0.930325	0.895773	0.888468	0.873604	0.870987	0.876758	0.859947	0.866945	0.856282
0.967751	0.96843	0.989576	0.973453	0.958613	0.94556	0.90293	0.893319	0.881603	0.869509	0.869405	0.853006	0.85691	0.84309
0.931418	0.934204	0.95397	0.982803	0.987988	0.971509	0.912612	0.905554	0.885443	0.877287	0.877789	0.864442	0.868134	0.857233
0.887313	0.892668	0.912502	0.920189	0.938335	0.943523	0.984134	0.971993	0.961623	0.943894	0.937679	0.923221	0.924321	0.9082
0.873086	0.87733	0.889165	0.897091	0.911902	0.91869	0.972449	0.976259	0.969023	0.954331	0.957899	0.9358	0.943027	0.929564
0.864891	0.868925	0.886657	0.887455	0.899027	0.903182	0.956825	0.96002	0.972147	0.984394	0.980431	0.959765	0.96358	0.945448
0.851745	0.854734	0.872992	0.874359	0.882665	0.89003	0.943503	0.95102	0.953212	0.981259	0.992673	0.971184	0.975	0.959991
0.855367	0.859685	0.882052	0.880547	0.889889	0.894661	0.948709	0.954368	0.961863	0.987576	0.996964	0.976028	0.97954	0.962663
0.847097	0.849591	0.869231	0.868803	0.875955	0.884923	0.938475	0.945083	0.948506	0.974209	0.984454	0.981739	0.984103	0.969048
0.853212	0.857015	0.875899	0.872592	0.881958	0.886396	0.939459	0.941442	0.951963	0.97676	0.989902	0.985179	0.988918	0.970428
0.848187	0.851677	0.869931	0.865018	0.874276	0.875945	0.928009	0.929221	0.941611	0.967503	0.980527	0.991715	0.996107	0.979366
0.849049	0.854115	0.878321	0.869339	0.877596	0.877154	0.930508	0.930436	0.94565	0.967156	0.97751	0.986885	0.99077	0.988223
0.840173	0.842917	0.867701	0.858725	0.864473	0.870624	0.923832	0.924025	0.939716	0.958319	0.965524	0.981819	0.981373	0.998561

(c) Extract of Similarity Array for case 11, Damaged Case, ΔT, White-noise force. Actual Array size is 98x97.

Figure 51: Extract of similarity array for cases 2, 7 and 11

Appendix B

Experimental cantilever beam results

The time domain responses, CWT and their corresponding WTMM decay lines at the location of 300^{th} pixel from the fixed end of the cantilever beam, for intact states (cases 3, 4, 5 and 6) and damaged states (cases 8, 9 and 10) using optical measurements are shown in figures 52, 53 and 54 respectively. The time domain responses, their corresponding CWT and WTMM decay lines for case 1 have been shown in figure39 while for cases 2, 7 and 11 in figure 41 in section 7.4. Similarly the time domain responses, CWT and their corresponding WTMM decay lines at the location of approximately 300^{th} pixel from the fixed end of the cantilever beam using measurements from an accelerometer for intact cases (cases 1 to 6) are shown in figure 55 and 56 and for damaged cases (cases 7 to 11) in figures 57 and 58 respectively. Extracts of the "Similarity Array" for cases 1, 2, 7 and 11 at the location of 300^{th} pixel from the fixed end of the cantilever beam are also shown in figure 59. As mentioned in section 5.5, each k^{th} column of the j^{th} row of these 2-dimensional arrays, contain the similarity value between the k^{th} WTMM decay line in the current time range with the j^{th} WTMM decay line in the previous time range.

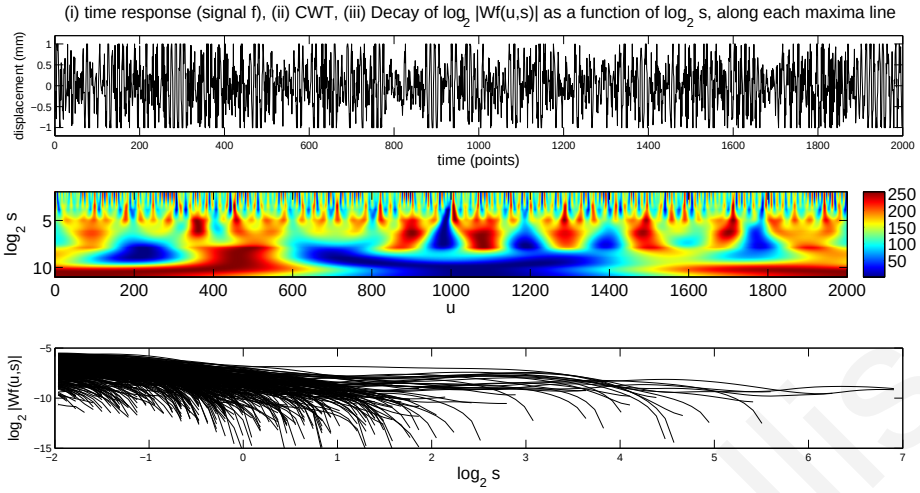

(a) (Case 3) Intact, Constant T, White-noise force (i) time response, (ii) CWT, (iii) WTMM decay lines

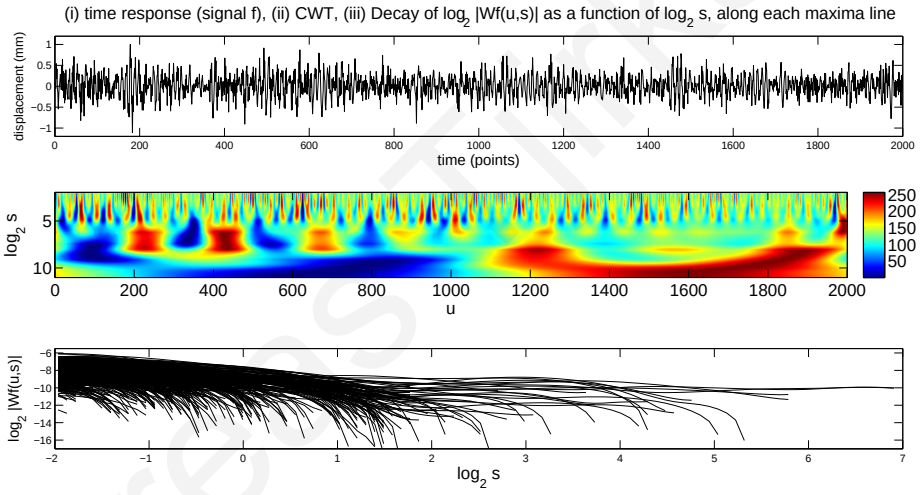

(b) (Case 4) Intact, ΔT, Pink-noise force (i) time response, (ii) CWT, (iii) WTMM decay lines

Figure 52: Cantilever beam location of 300^{th} pixel from fixed-end of the beam (i) time domain response, (ii) CWT and (iii) WTMM Decay lines for cases 3, 4 (intact cases) - optical measurements

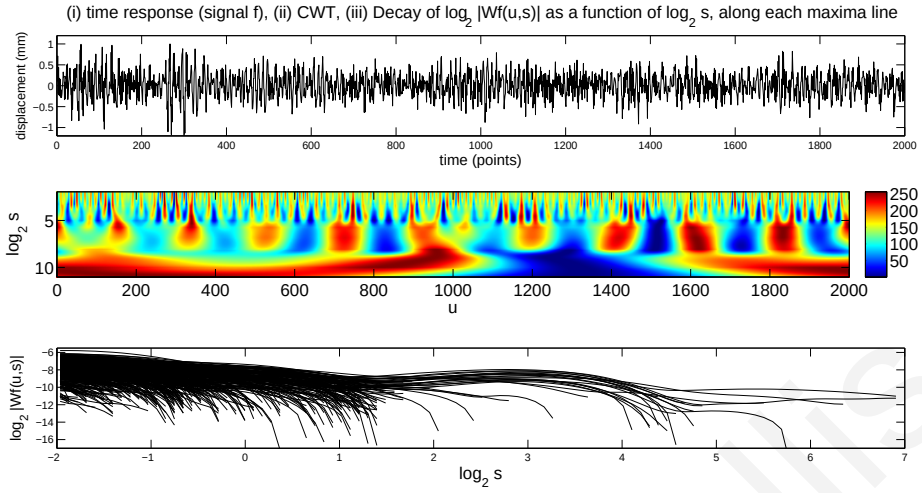

(a) (Case 5) Intact, Constant T, Pink-noise force different realisation (i) time response, (ii) CWT, (iii) WTMM decay lines

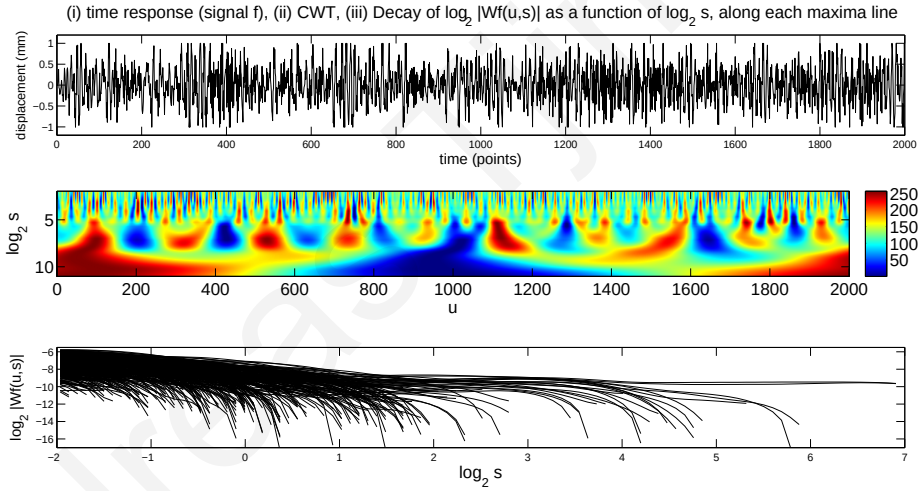

(b) (Case 6) Intact, ΔT, White-noise force (i) time response, (ii) CWT, (iii) WTMM decay lines

Figure 53: Cantilever beam location of 300^{th} pixel from fixed-end (i) time domain response, (ii) CWT and (iii) WTMM Decay lines for cases 5, 6 (intact cases) - optical measurements

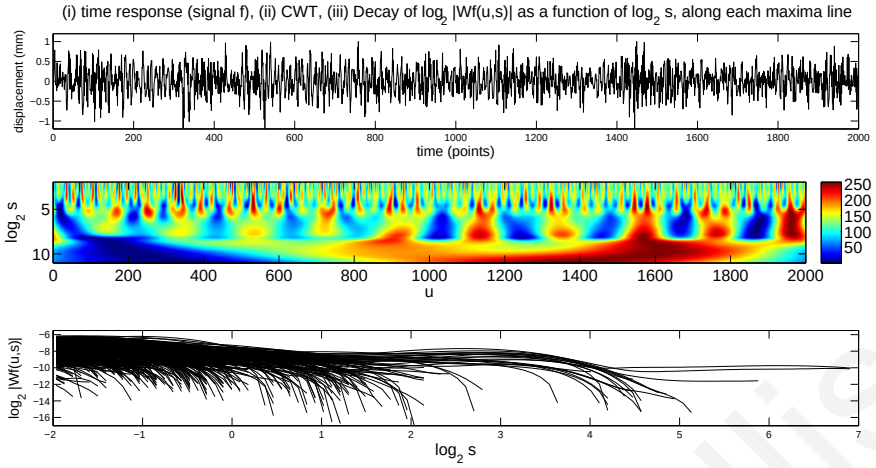

(a) (Case 8) Damaged, Pink-noise Δf realisation (i) time response, (ii) CWT, (iii) WTMM decay lines

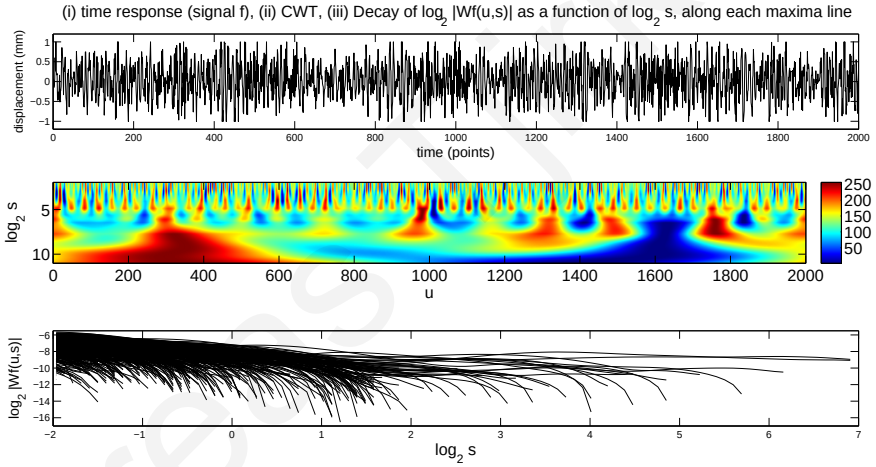

(b) (Case 9) Damaged, White-noise force (i) time response, (ii) CWT, (iii) WTMM decay lines

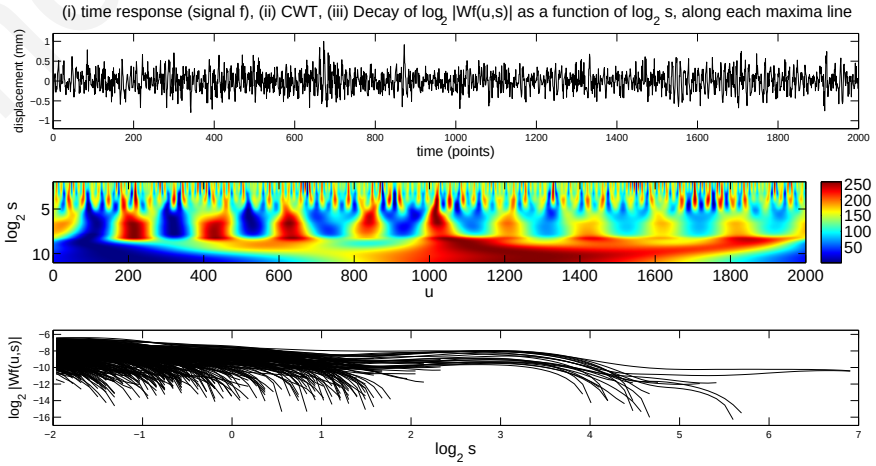

(c) (Case 10) Damaged, ΔT, Pink-noise force (i) time response, (ii) CWT, (iii) WTMM decay lines

Figure 54: Cantilever beam location of 300^{th} pixel from fixed-end (i) time response, (ii) CWT and (iii) WTMM DLs for cases 8, 9 and 10 (damaged cases) - optical measurements

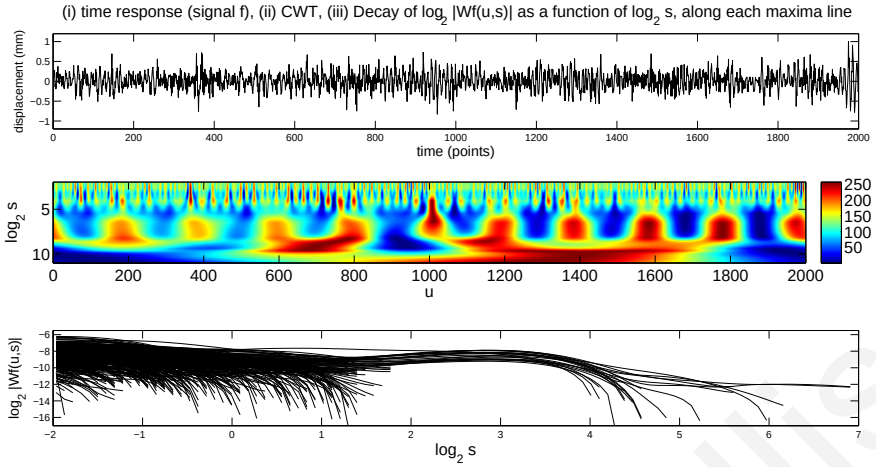

(a) (Case 1) Intact, Pink-noise force (i) time response, (ii) CWT, (iii) WTMM decay lines

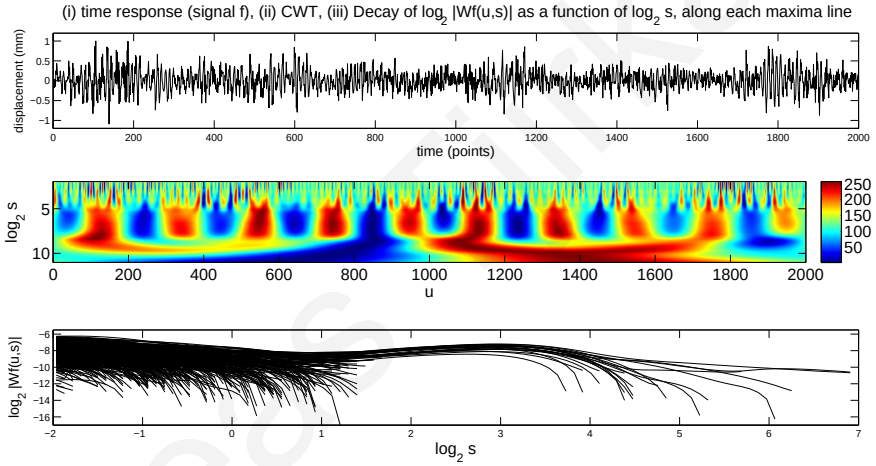

(b) (Case 2) Intact, Pink-noise Δf realisation (i) time response, (ii) CWT, (iii) WTMM decay lines

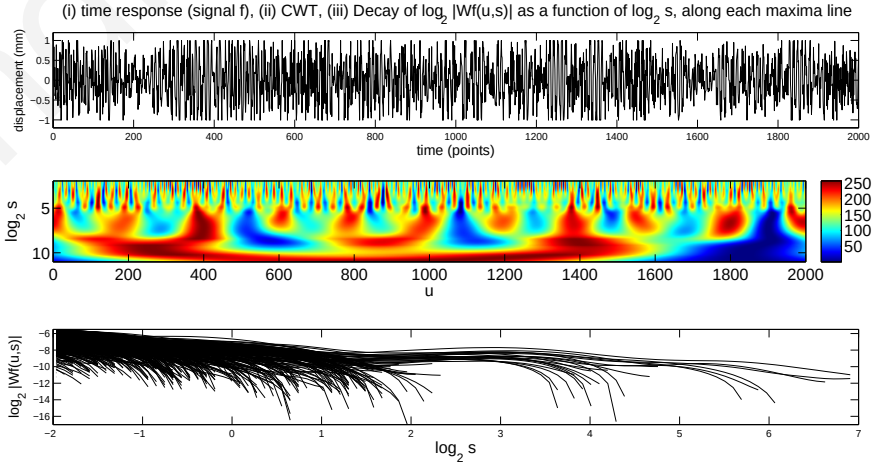

(c) (Case 3) Intact, White-noise force (i) time response, (ii) CWT, (iii) WTMM decay lines

Figure 55: Cantilever beam location of 300^{th} pixel from fixed-end (i) time response, (ii) CWT and (iii) WTMM Decay lines for cases 1 to 3 (intact cases) - accelerometer

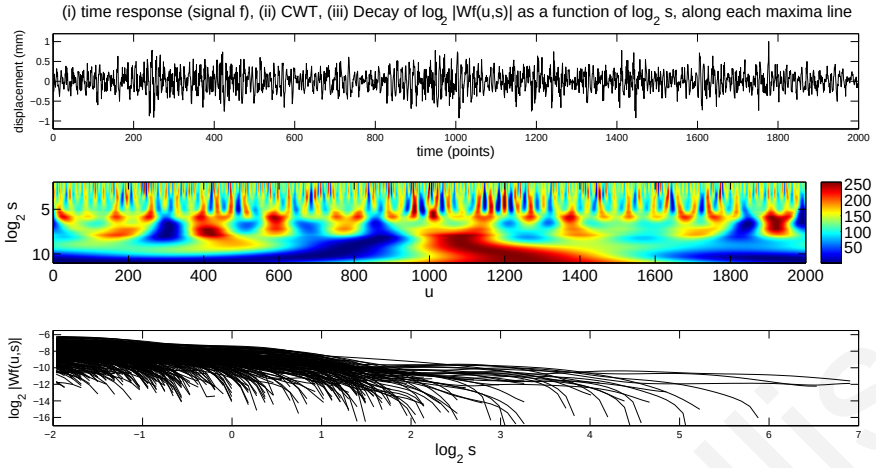

(a) (Case 4) Intact, ΔT, Pink-noise force (i) time response, (ii) CWT, (iii) WTMM decay lines

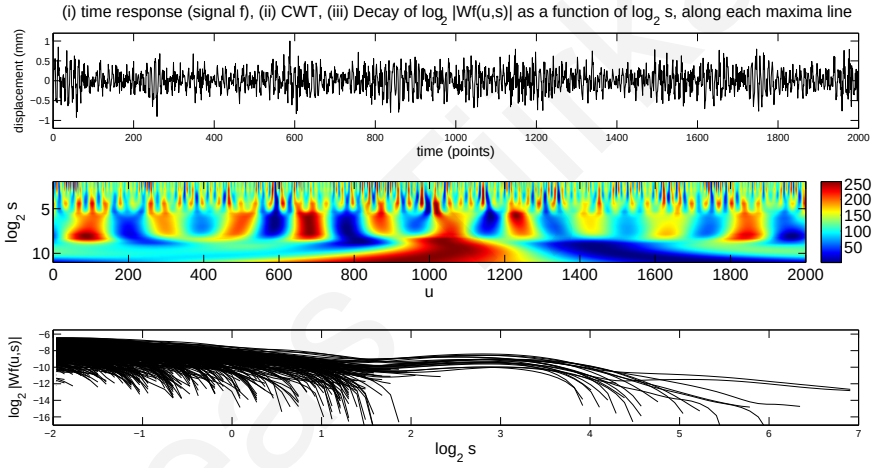

(b) (Case 5) Intact, Pink-noise Δf realisation (i) time response, (ii) CWT, (iii) WTMM decay lines

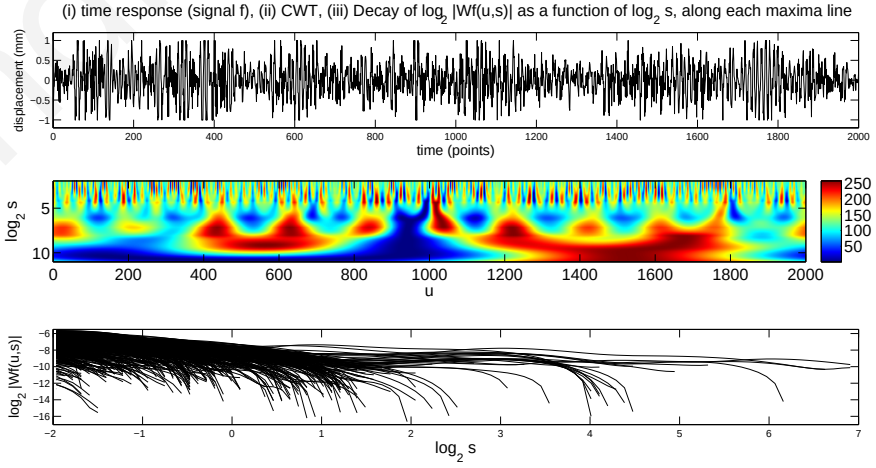

(c) (Case 6) Intact, ΔT, White-noise force (i) time response, (ii) CWT, (iii) WTMM decay lines

Figure 56: Cantilever beam location of 300^{th} pixel from fixed-end (i) time response, (ii) CWT and (iii) WTMM Decay lines for cases 4 to 6 (intact cases) - accelerometer

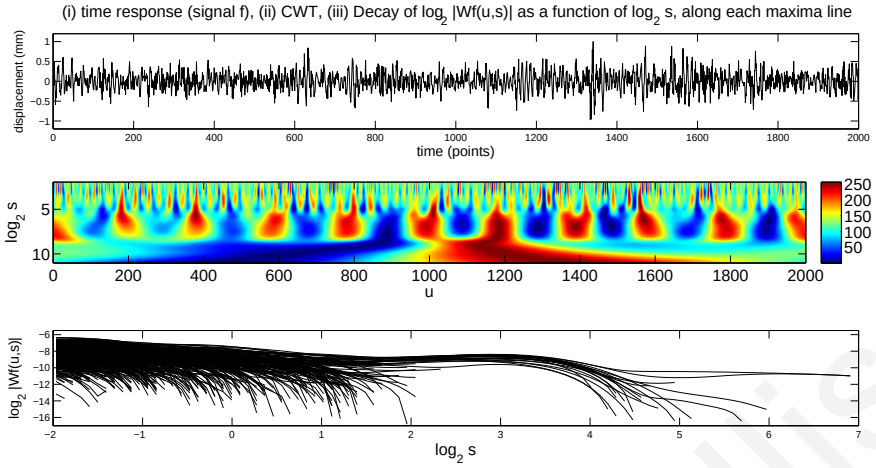

(a) (Case 7) Damaged, Pink-noise force (i) time response, (ii) CWT, (iii) WTMM decay lines

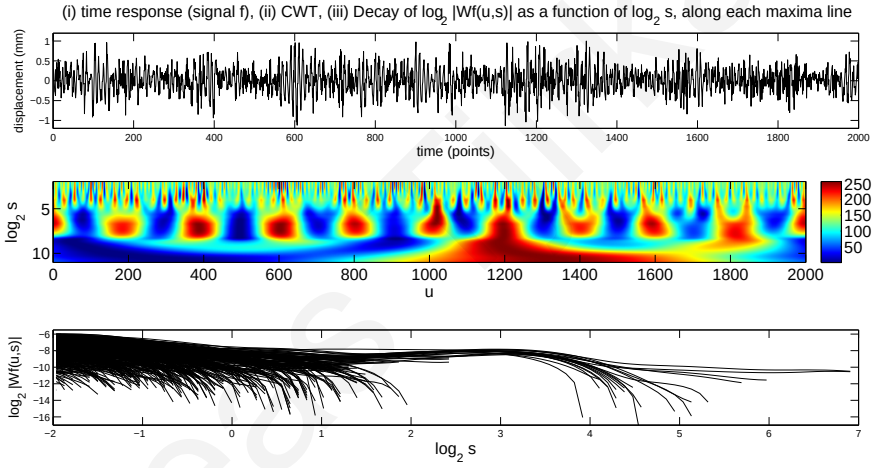

(b) (Case 8) Damaged, Pink-noise Δf realisation (i) time response, (ii) CWT, (iii) WTMM decay lines

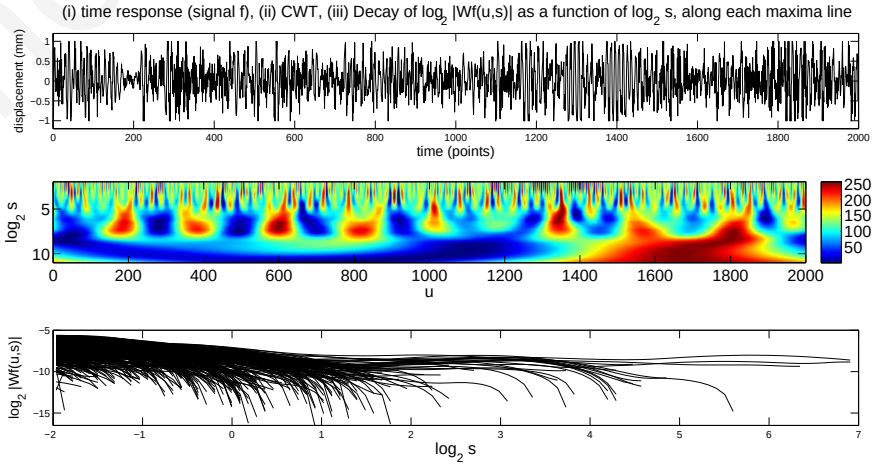

(c) (Case 9) Damaged, White-noise force (i) time response, (ii) CWT, (iii) WTMM decay lines

Figure 57: Cantilever beam location of 300^{th} pixel from fixed-end (i) time response, (ii) CWT and (iii) WTMM Decay lines for cases 7 to 9 (damaged cases) - accelerometer

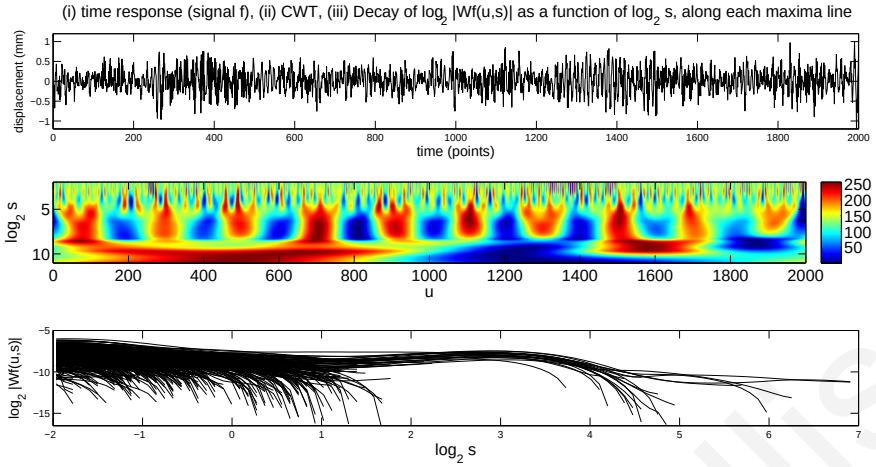

(a) (Case 10) Damaged, ΔT, Pink-noise force (i) time response, (ii) CWT, (iii) WTMM decay lines

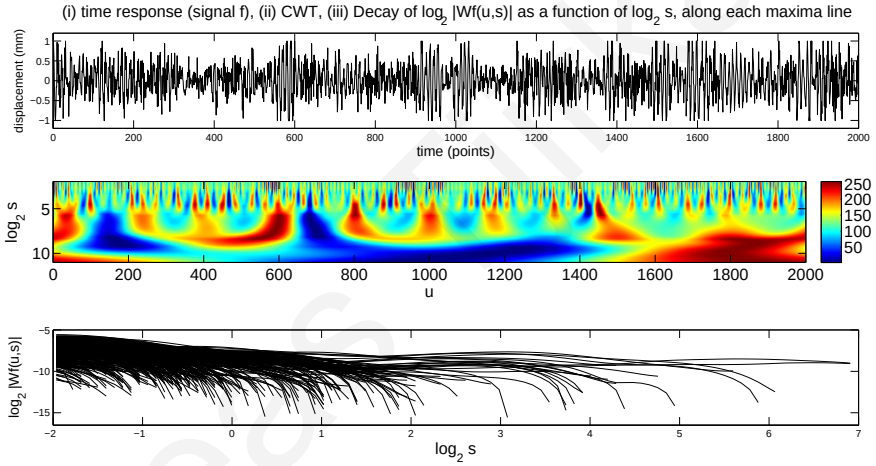

(b) (Case 11) Damaged, ΔT, White-noise force (i) time response, (ii) CWT, (iii) WTMM decay lines

Figure 58: Cantilever beam location of 300^{th} pixel from fixed-end (i) time response, (ii) CWT and (iii) WTMM Decay lines for cases 10 and 11 (damaged cases) - accelerometer

0.987761	0.991719	0.972892	0.945957	0.922796	0.917676	0.828036	0.827568	0.823128	0.810506	0.817163	0.814601	0.806551	0.799933
0.990088	0.993845	0.971565	0.943532	0.917194	0.911023	0.819234	0.818887	0.813896	0.801629	0.807999	0.805169	0.797187	0.790695
0.920241	0.91766	0.96074	0.97015	0.975746	0.973909	0.870881	0.871422	0.866164	0.849504	0.862225	0.838411	0.830258	0.832403
0.892632	0.891089	0.930987	0.940782	0.983413	0.994917	0.878429	0.878168	0.873132	0.854327	0.868165	0.835718	0.828231	0.833745
0.87068	0.880431	0.899829	0.910946	0.954647	0.959139	0.907376	0.904005	0.894972	0.876378	0.883541	0.851403	0.84698	0.846307
0.852091	0.860304	0.882786	0.892226	0.936081	0.943689	0.916526	0.911629	0.906169	0.883887	0.894294	0.854443	0.849361	0.854157
0.8503	0.861363	0.88171	0.885716	0.932368	0.937868	0.92799	0.926993	0.916072	0.897478	0.904898	0.874786	0.869561	0.867167
0.846991	0.853434	0.8769	0.885489	0.928539	0.935848	0.928597	0.922401	0.91845	0.896513	0.906842	0.866063	0.861198	0.8677
0.839848	0.852313	0.866296	0.873721	0.917106	0.920743	0.947578	0.940463	0.932694	0.911804	0.917789	0.879353	0.876106	0.877128
0.839932	0.853027	0.865157	0.872292	0.915939	0.918512	0.951816	0.945205	0.936752	0.917221	0.922445	0.883939	0.881041	0.882012
0.817358	0.825831	0.84631	0.847557	0.891018	0.897053	0.96849	0.962156	0.954748	0.933424	0.942305	0.895906	0.891966	0.898558
0.814112	0.812844	0.847254	0.843409	0.885051	0.893153	0.975531	0.969007	0.965741	0.946695	0.957988	0.916306	0.910725	0.920647
0.785007	0.789667	0.813309	0.811243	0.846928	0.853791	0.95964	0.962574	0.977586	0.993966	0.997023	0.953127	0.952154	0.955797
0.780753	0.781121	0.811333	0.807327	0.842644	0.851044	0.950157	0.951791	0.968014	0.982293	0.986572	0.963273	0.961925	0.96457

(a) Extract of Similarity Array for case 1, Intact Case, Pink-noise force. Actual Array size is 44x44.

0.987761	0.991719	0.972892	0.945957	0.922796	0.917676	0.828036	0.827568	0.823128	0.810506	0.817163	0.814601	0.806551	0.799933
0.990088	0.993845	0.971565	0.943532	0.917194	0.911023	0.819234	0.818887	0.813896	0.801629	0.807999	0.805169	0.797187	0.790695
0.920241	0.91766	0.96074	0.97015	0.975746	0.973909	0.870881	0.871422	0.866164	0.849504	0.862225	0.838411	0.830258	0.832403
0.892632	0.891089	0.930987	0.940782	0.983413	0.994917	0.878429	0.878168	0.873132	0.854327	0.868165	0.835718	0.828231	0.833745
0.87068	0.880431	0.899829	0.910946	0.954647	0.959139	0.907376	0.904005	0.894972	0.876378	0.883541	0.851403	0.84698	0.846307
0.852091	0.860304	0.882786	0.892226	0.936081	0.943689	0.916526	0.911629	0.906169	0.883887	0.894294	0.854443	0.849361	0.854157
0.8503	0.861363	0.88171	0.885716	0.932368	0.937868	0.92799	0.926993	0.916072	0.897478	0.904898	0.874786	0.869561	0.867167
0.846991	0.853434	0.8769	0.885489	0.928539	0.935848	0.928597	0.922401	0.91845	0.896513	0.906842	0.866063	0.861198	0.8677
0.839848	0.852313	0.866296	0.873721	0.917106	0.920743	0.947578	0.940463	0.932694	0.911804	0.917789	0.879353	0.876106	0.877128
0.839932	0.853027	0.865157	0.872292	0.915939	0.918512	0.951816	0.945205	0.936752	0.917221	0.922445	0.883939	0.881041	0.882012
0.817358	0.825831	0.84631	0.847557	0.891018	0.897053	0.96849	0.962156	0.954748	0.933424	0.942305	0.895906	0.891966	0.898558
0.814112	0.812844	0.847254	0.843409	0.885051	0.893153	0.975531	0.969007	0.965741	0.946695	0.957988	0.916306	0.910725	0.920647
0.785007	0.789667	0.813309	0.811243	0.846928	0.853791	0.95964	0.962574	0.977586	0.993966	0.997023	0.953127	0.952154	0.955797
0.780753	0.781121	0.811333	0.807327	0.842644	0.851044	0.950157	0.951791	0.968014	0.982293	0.986572	0.963273	0.961925	0.96457

(b) Extract of Similarity Array for case 2, Intact Case, Pink-noise Δf realisation. Actual Array size is 44x42.

0.991305	0.982288	0.929418	0.887307	0.867962	0.849634	0.853854	0.840667	0.827142	0.821419	0.816138	0.801916	0.800971	0.802674
0.992708	0.983713	0.924314	0.880443	0.860189	0.84147	0.845373	0.831765	0.818489	0.812458	0.806826	0.792734	0.791694	0.793497
0.935423	0.923424	0.98017	0.951106	0.924316	0.906405	0.904727	0.884877	0.884259	0.867332	0.854263	0.848913	0.829807	0.840228
0.913194	0.898864	0.974895	0.973681	0.940641	0.923012	0.915963	0.892577	0.896273	0.875677	0.858824	0.856896	0.831702	0.843661
0.900557	0.891244	0.946772	0.980624	0.981027	0.958949	0.947962	0.921346	0.9159	0.896004	0.878288	0.869135	0.855305	0.856155
0.882025	0.86923	0.926124	0.968236	0.993392	0.975171	0.958607	0.929439	0.930601	0.908688	0.887751	0.884533	0.861692	0.865908
0.883943	0.875354	0.926078	0.956005	0.98563	0.979233	0.971792	0.945156	0.938572	0.917608	0.899716	0.888484	0.874872	0.876767
0.874342	0.863238	0.91707	0.961475	0.984383	0.984743	0.967286	0.939087	0.941657	0.921287	0.900232	0.8988	0.875191	0.879598
0.868817	0.863164	0.906352	0.944182	0.971997	0.986471	0.988001	0.958561	0.954017	0.934159	0.913478	0.905826	0.891254	0.88849
0.868973	0.862702	0.905102	0.942748	0.971741	0.985455	0.989497	0.962132	0.957854	0.938371	0.917971	0.910092	0.895993	0.893399
0.843497	0.836997	0.878004	0.922303	0.940432	0.953015	0.974373	0.978069	0.981434	0.958531	0.934506	0.932513	0.908726	0.91181
0.831884	0.829937	0.870856	0.914282	0.92807	0.939235	0.961776	0.981947	0.987843	0.968919	0.948613	0.950264	0.923953	0.932716
0.799	0.807396	0.829017	0.870884	0.885934	0.898244	0.921211	0.944463	0.954726	0.97923	0.995704	0.990093	0.978354	0.968252
0.790719	0.803105	0.82494	0.866177	0.878359	0.890676	0.913785	0.936187	0.945397	0.970384	0.985326	0.999218	0.988172	0.976896

(c) Extract of Similarity Array for case 7, Damaged Case, Pink-noise force. Actual Array size is 44x39.

0.996894	0.997894	0.968567	0.932949	0.926423	0.915418	0.844196	0.837806	0.817022	0.820981	0.827858	0.819377	0.814898	0.811086
0.997582	0.99796	0.965336	0.927151	0.920094	0.90951	0.835706	0.828783	0.808221	0.812009	0.81892	0.810457	0.805537	0.801742
0.936885	0.942926	0.974665	0.982999	0.986026	0.967806	0.897694	0.891586	0.872087	0.871836	0.863788	0.864048	0.868043	0.854766
0.907394	0.915666	0.947666	0.978046	0.987209	0.988109	0.909763	0.901841	0.884049	0.88106	0.867365	0.871162	0.878214	0.861022
0.884548	0.886721	0.916847	0.951633	0.960807	0.96031	0.939549	0.916979	0.902313	0.89726	0.892706	0.890085	0.885917	0.871907
0.865897	0.872694	0.900677	0.934787	0.952898	0.943152	0.9516	0.932744	0.918941	0.911784	0.898333	0.901308	0.905401	0.886676
0.868393	0.876281	0.902015	0.933149	0.946553	0.936696	0.962203	0.9405	0.922508	0.918122	0.915647	0.912344	0.90638	0.892224
0.860545	0.867985	0.893294	0.928356	0.948046	0.937193	0.961499	0.944184	0.932073	0.924691	0.909588	0.913552	0.919377	0.900566
0.85449	0.858336	0.882108	0.918573	0.934149	0.92532	0.980315	0.953588	0.94253	0.934773	0.927683	0.926066	0.923228	0.907272
0.853841	0.857593	0.880143	0.917223	0.932196	0.924478	0.982739	0.957082	0.946479	0.939121	0.932704	0.930922	0.925953	0.911129
0.832451	0.844044	0.860515	0.894598	0.916761	0.90141	0.985955	0.980946	0.970552	0.961641	0.946872	0.950272	0.952734	0.932867
0.831806	0.848263	0.860148	0.891437	0.913751	0.897401	0.973644	0.991201	0.980838	0.975114	0.957335	0.962196	0.969279	0.951845
0.80192	0.814517	0.822232	0.856872	0.872342	0.865595	0.933773	0.967182	0.972064	0.981983	0.971468	0.986901	0.987745	0.989768
0.799174	0.814734	0.820685	0.853421	0.869367	0.861658	0.925377	0.961678	0.962953	0.973356	0.963042	0.977278	0.981711	0.999571

(d) Extract of Similarity Array for case 11, Damaged Case, ΔT, White-noise force. Actual Array size is 44x43.

Figure 59: Extract of similarity array for cases 1, 2, 7 and 11 for the 300^{th} location from the fixed end of the cantilever beam - optical measurements

Appendix C

Results using Holder Exponent Analysis

The Holder Exponent (HE) at a particular time point in a signal is obtained using equation 12 of section 3.4. This is repeated for each time point of the wavelet modulus, obtaining the Holder Exponent for all the time points in a time range. A comparison between the Holder Exponents of two time ranges is achieved using equation [73],

$$\Delta HE = |HE_{current} - HE_{previous}| \tag{49}$$

The absolute difference of the Holder Exponents between the sine wave with and without the artificial singularity is illustrated graphically in figure 60, whereas that for the ARMA/ARIMA model with changes in parameters from C_1 to C_2 and A_1 to A_2 in figure 61. From the plot of the absolute difference of Holder Exponents using the sine wave example, it can be seen that at the location of the singularity the absolute value of the difference between the Holder Exponents is significant, thus the HE analysis can be used to indicate the presence of the singularity. The plot of the absolute difference of the Holder Exponents using the ARMA/ARIMA model, illustrates that when the parameter changes from C_1 to C_2, with both time ranges being stationary, there is no significant value of absolute difference of the Holder Exponent between the two time ranges. However, when the ARMA model parameter changes from A_1 to A_2, resulting in a transition of the time range from stationary to non-stationary, there are a number of significant values of absolute difference of the Holder Exponenet between the two time ranges.

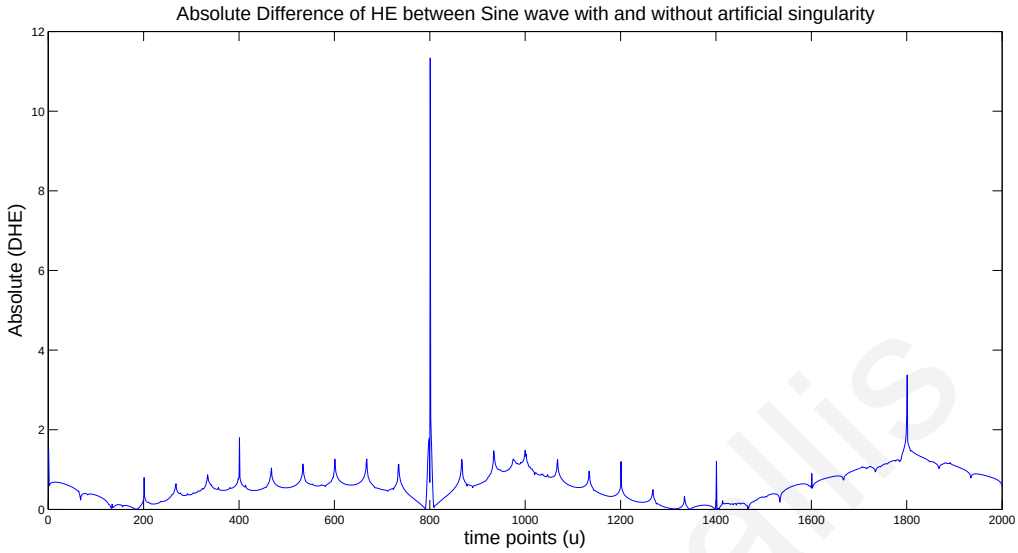

Figure 60: $|\Delta HE|$ values between time ranges of a sine wave with and without an artificial singularity

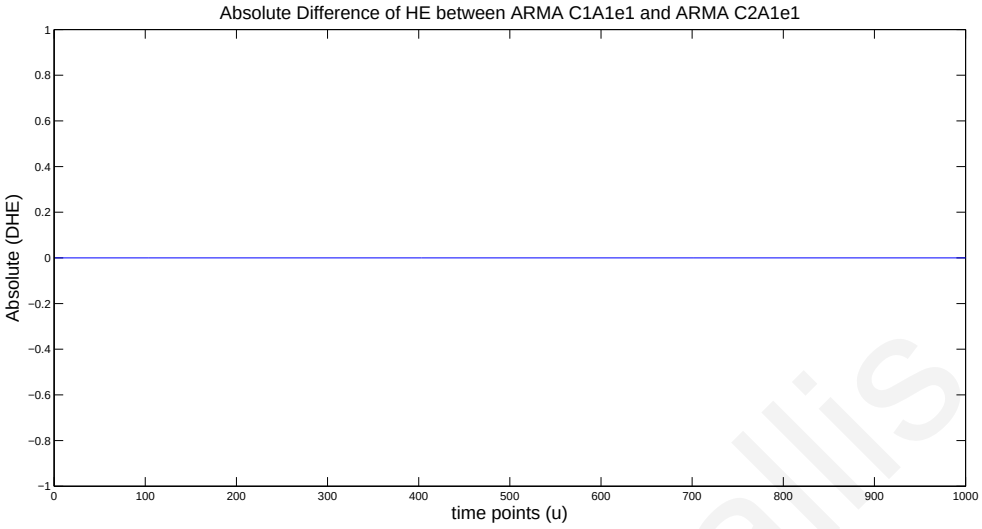

(a) $|\Delta HE|$ values between time ranges of ARMA model with parameters (C_1, A_1, e_1) and (C_2, A_1, e_1)

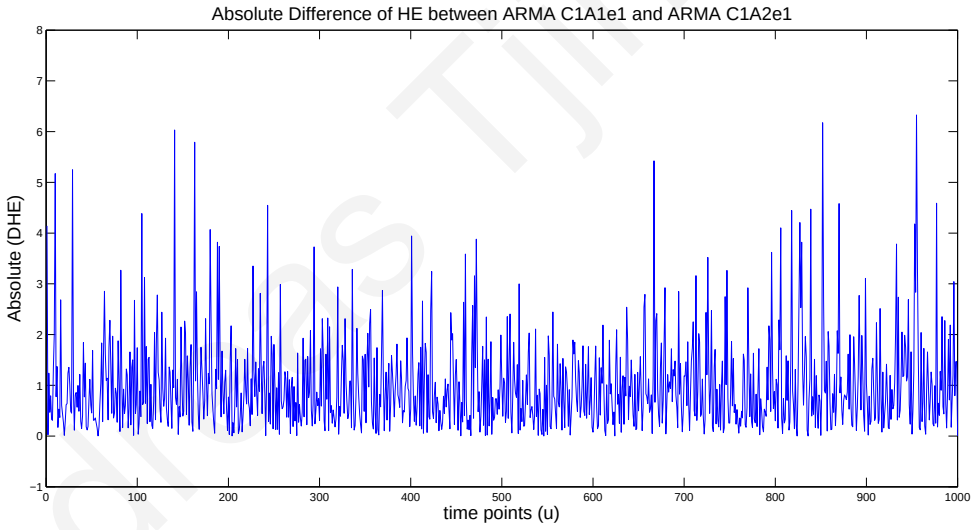

(b) $|\Delta HE|$ values between time ranges of ARMA model with parameters (C_1, A_1, e_1) and (C_1, A_2, e_1)

Figure 61: Absolute Difference of Holder Exponent values between time ranges of ARMA and ARIMA models.

The comparison of the absolute value of the difference of the Holder Exponents between the time ranges of the 3 DOF simulation system under Cases 2, 3, 4, 7 and 11 with Case 1, as referred to in table 3 in section 6.1, is also obtained and illustrated graphically in figures 62 and 63.

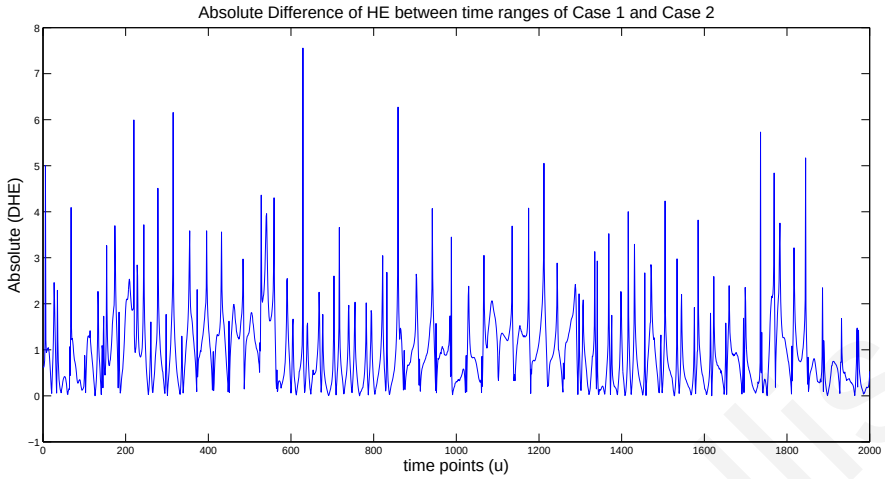

(a) $|\Delta HE|$ values between time ranges of Case 1 and 2 (changes due to change in force realisation)

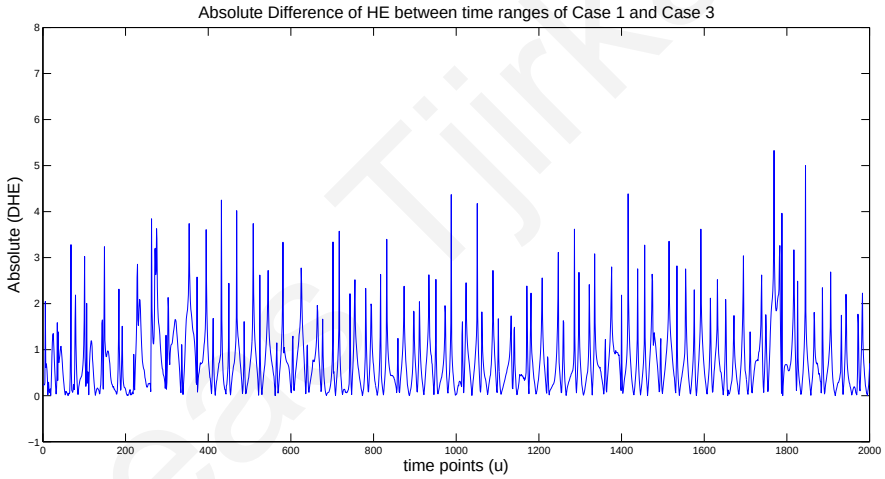

(b) $|\Delta HE|$ values between time ranges of Case 1 and 3 (changes due to Δf from pink to white noise)

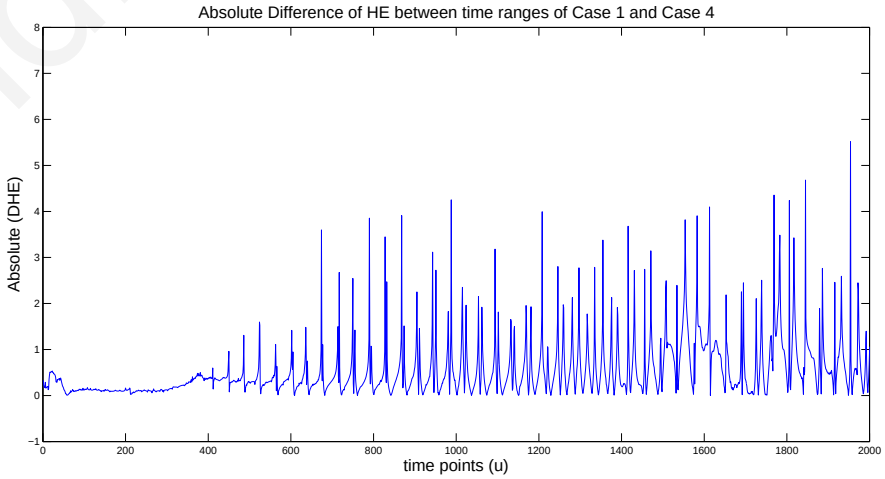

(c) $|\Delta HE|$ values between time ranges of Case 1 and 4 (changes due to temperature variability)

Figure 62: Absolute Difference of Holder Exponent values between time ranges of the 3 DOF simulation system in an intact state, under different cases.

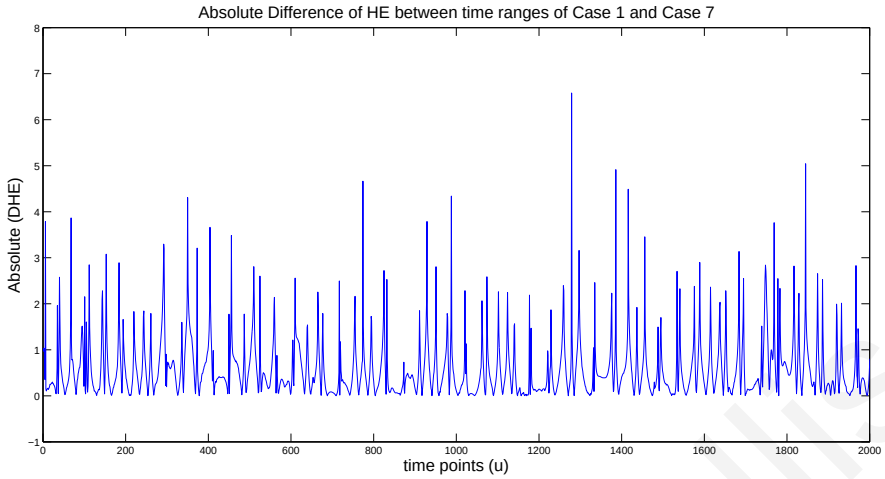

(a) $|\Delta HE|$ values between time ranges of Case 1 and 7 (changes due to damage)

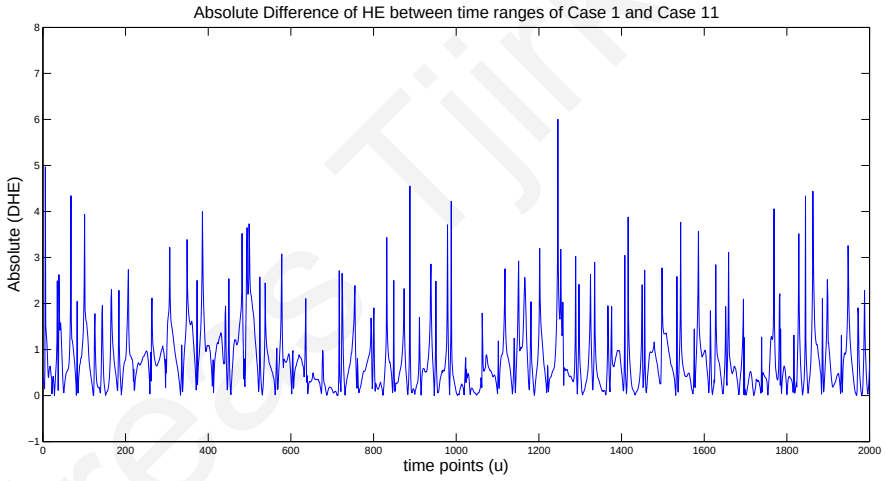

(b) $|\Delta HE|$ values between time ranges of Case 1 and 11 (changes due to damage, forcing conditions and temperature variability)

Figure 63: Absolute Difference of Holder Exponent values between time ranges of the 3 DOF simulation system in a damaged state, under different cases.

From these plots it can be observed that there is a change in the Holder Exponents between time ranges, due to the presence of singularities as a result of a change in the force realisation, change in the forcing conditions, temperature variability, damage or a combination of these changes. This implies that the Holder Exponent analysis, cannot be used to identify the presence of damage under varying enviromental and/or operational conditions directly.

Bibliography

[1] Doebling W. S., Farrar R. C., Prime B. M., and Shevitz W. D. Damage identification and health monitoring of structural and mechanical systems from changes in their vibration characteristics: Literature review. Technical Report LA-13070-MS, May 1996.

[2] Huang Lu. *Refined Boundary Effect Evaluation Method for on-site damage inspection of structures*. PhD thesis, University of Missouri - Columbia, 2005.

[3] Collacott R. A. *Structural integrity monitoring*. Chapman and Hall, New York, NY, 1985.

[4] Cornwell J. P., Farrar R. C., Doebling W. S., and Sohn H. Environmental variability of modal properties. *Experimental Techniques*, pages 45–48, Nov/Dec 1999.

[5] Sohn H. Effects of environmental and operational variability on structural health monitoring. *Philosophical Transactions of the Royal Society*, A365:539–656, 2007.

[6] Worden K., Sohn H., and Farrar R. C. Novelty detection in a changing environment: Regression and interpolation approaches. *Journal of Sound and Vibration*, 258(4):741–761, 2002.

[7] Cross E. J., Worden K., and Chen Q. Cointegration: a novel approach for the removal of environmental trends in structural health monitoring data. *Proceedings of the Royal Society*, A467(2133):2712–2732, 2011.

[8] Cross E. J. and Worden K. Cointegration and why it works for shm. *Journal of Physics: Conference Series 382, IOP Publising*, 2012.

[9] Douka E., Loutridis S., and Trochidis A. Crack identification in beams using wavelet analysis. *International Journal of Solids and Structures*, 40(Issues 13-14):3557–3569, 2003.

[10] Gentile A. and Messina A. On the continuous wavelet transforms applied to discrete vibrational data for detecting open cracks in damaged beams. *International Journal of Solids and Structures*, 40:295–315, 2003.

[11] Mallat S. *A Wavelet Tour of Signal Processing,* 2^{nd} *edition*. London, UK Academic Press, 1999.

[12] Mallat S. and Hwang W. L. Singularity detection and processing with wavelets. *IEEE Transactions on Information Theory*, 38:617–643, 1992.

[13] Hasse M. and Widjakusuma J. Damage identification based on ridges and maxima lines of wavelet transform. *International Journal of Engineering Science*, 41:1423–1443, 2003.

[14] N. A. Robertson, Farrar R. C., and Sohn H. Singularity detection for structural health monitoring using holder exponents. *Mechanical Systems and Signal Processing*, 17(6):1163–1184, 2003.

[15] Worden K., Cross E. J., Kyprianou A., and Antoniadou I. Multiresolution approach to cointegration for enhanced shm of structures under varying conditions - an exploratory study. *Mechanical Systems and Signal Processing. DOI 10.1016 j.ymssp.2013.10.012*, 2013.

[16] Farrar R. C. and Worden K. An introduction to structural health monitoring. *Philosophical Transaction of the Royal Society*, A365:303–315, 2007.

[17] Kam T. Y. and Lee T. Y. Identification of crack size via an energy approach. *Journal of Nondestructive Evaluation*, 13:1–11, 1994.

[18] Dawson B. Vibration condition monitoring techniques for rotating machinery. *The Shock and Vibration Digest (London: SpingerLink)*, 8(3), 1976.

[19] Cartz L. *Nondestructive Testing: Radiography Ultrasonics Liquid Penetrant Magnetic Particle Eddy Current*. Asm International 1995 3^{rd} edition, 1995.

[20] Deraemaeker A., Reynders E., De Roeck G., and Kullaa J. Vibration-based structural health monitoring using output-only measurements under changing environment. *Mechanical Systems and Signal Processing*, 22:34–56, 2008.

[21] Limongelli M. P. Frequency response function interpolation for damage detection under changing environment. *Mechanical Systems and Signal Processing*, 24:2898–2913, 2010.

[22] Oh C. K. and Sohn H. Damage diagnosis under environmental and operational variations using unsupervised support vector machine. *Journal of Sound and Vibration*, 325:224–239, 2009.

[23] Lim J. L., Kim M. K., Sohn H., and Park C. Y. Impedance based damage detection under varying temperature and loading conditions. *NDTE International*, 44:740–750, 2011.

[24] Surace C. and Worden K. Novelty detection in a changing environment: A negative selection approach. *Mechanical Systems and Signal Processing*, 24:1114–1128, 2010.

[25] Figueiredo E., Todd M. D., Farrar C. R., and Flynn E. Autoregressive modeling with state-pace embedding vectors for damage detection under operational variability. *International Journal of Engineering Science*, 48:822–834, 2010.

[26] Kim S. B. and Sohn H. Instantaneous reference-free crack detection based on polarization characteristics of piezoelectric materials. *Smart Materials and Structures*, 16:2375–2387, 2007.

[27] An Y. B. and Sohn H. Instantaneous crack detection under varying temperature and static loading conditions. *Structural Control and Health Monitoring*, 17:730–741, 2010.

[28] Sohn H., Dutta D., and An Y. K. Temperature independent damage detection in plates using redundant signal measurements. *Journal of Nondestructive Evaluation*, 30:106–116, 2011.

[29] Kim M. K., Kim E. J., An Y. K., Park H. W., and Sohn H. Reference-free impedance-based crack detection in plates. *Journal of Sound and Vibration*, 330:5949–5962, 2011.

[30] Ewins D. J. Modal testing: Theory, practice and application. *2nd edition, ISBN: 0-86-380218-4, Research Studies Press Ltd., England*, 2000.

[31] Migliori A., Bell T. M., Dixon R. D., and Strong R. Resonant ultrasound non-destructive inspection. Technical Report LA-UR-93-225, 1993.

[32] Farrar C. R., Darling T., and Migliori A. Microwave interferometers for remote non-contact vibration measurements. *Mechanical Systems and Signal Processing*, 13(Part 2):241–253, 1999.

[33] Luzi G., Monserrat O., and Crosetto M. Real aperture radar interferometry as a tool for buildings vibration monitoring: limits and potentials from an experimental study. *AIP Conference Proc. 10^{th} International Conference on Vibration Measurements by Laser and Noncontact Techniques*, pages 309–317, 2012.

[34] Martelli M. *Exploiting the Laser Scanning Facility for Vibration Measurements*. PhD thesis, Imperial College, London, 2001.

[35] Sharma V. K. *Laser Doppler Vibrometer for Efficient Structural Health Monitoring*. PhD thesis, School of Aerospace Engineering Georgia Institute of Technology, 2008.

[36] Patsias S. and Staszewski W. J. Damage detection using optical measurements and wavelet. *Structural Health Monitoring*, 1(1):5–22, 2002.

[37] Helfrick M., Pingle P., Niezrecki C., and Avitabile P. Optical non-contact vibration measurement of rotating turbine blades. *Proceedings of the IMAC-XXVII*, 2009.

[38] Maia N. M. M. and Silva J. M. M. *Theoretical and Experimental Modal Analysis*. Taunton: Research Studies Press Ltd, 1997.

[39] Melchers R. E. *Structural Reliability Analysis and Prediction*. John Willey and Sons 2^{nd} edition., 1999.

[40] Doebling S. W., Farrar C. R., and Prime M. B. A summary review of vibration-based damage identification techniques. *Shock and Vibration Digest*, 205:631–645, 1999.

[41] Patsias S. *Extraction of Dynamic Characteristics from Vibrating Structures using Image Sequences*. PhD thesis, University of Sheffield, 2000.

[42] Richardson M. H. Is it a mode shape or an operating deflection shape? *Sound and Vibration Magazine 30th Anniversary Issue*, 1997.

[43] Pai P. F. and Young L. G. Damage detection of beams using operational deflection shapes. *International Journal of Solids and Structures*, 38:3161–3192, 2001.

[44] Di Maio D., Zang C., and Ewins D. J. Identification of damage location using operational deflection shape. *XXV IMAC Conference*, pages 1–13, 2007.

[45] Tian Z. and Yu L. Lamb wave structural health monitoring using frequency-wavenumber analysis. *AIP Conference Proceedings*, 1511:302–309, 2012.

[46] Haroon M. and Adams D. E. Time and frequency domain nonlinear system characterization for mechanical fault identification. *Nonlinear dynamics*, 50(3):387–408, 2007.

[47] Heyns P. S. Structural damage assessment using response-only measurements. *Structural Damage Assessment Using Advanced Signal Processing Procedures. Proceedings of DAMAS 1997.*, pages 213–223, 1997.

[48] Sohn H. and Farrar C. R. Statistical process control and projection techniques for damage detection. *European COST F3 Conference on System Identification and Structural Health Monitoring. Madrid*, pages 105–114, 2005.

[49] Amir A. M. K. H. *Vibration-based Damage Detection and Health Monitoring of Bridges*. PhD thesis, North Carolina State University, 2010.

[50] Fasel T. R., Gregg S. W., Johnson T. J., Farrar C. R., and Sohn H. Experimental modal analysis and damage detection in a simulated three story building. *Proceedings of the 20th International Modal Analysis Conference - IMAC Los Angeles CA*, pages 590–595, 2002.

[51] Sohn H., Farrar C. R., Hunter N. F., and Worden K. Structural health monitoring using statistical pattern recognition techniques. *Journal of Dynamic Systems Measurement and Control*, 123(4):706–711, 2001.

[52] Sohn H., Farrar C. R., Hunter N. F., and Worden K. Applying the lanl statistical pattern recognition paradaigm for structural health monitoring to data from a surface-effect fast patrol boat. Technical Report LA-13761-MS, 2001.

[53] Sohn H. and Farrar C. R. Damage diagnosis using time series analysis of vibration signals. *Smart materials and structures*, 10(3):446–451, 2001.

[54] Hou Z., Noori M., and Amand R. St. Wavelet-based approach for structural damage detection. *Journal of Engineering Mechanics*, 126(7):677–683, 2000.

[55] Staszewski W. J. and Tomlinson G. R. Application of the wavelet transform to fault detection in a spur gear. *Mechanical System and Signal Processing*, 8(3):289–307, 1994.

[56] Wang S., Hu Y., Chu D., Liu M., and Qiuzhi G. High-speed cinematography in the investigation of nonlinear oscillation of vibration mill. *Processings of SPIE*, 2899:611–616, 1996.

[57] Cross E. J. *On Structural Health Monitoring in Changing Environmental and Operational Conditions*. PhD thesis, The University of Sheffield, 2012.

[58] Manson G. Identifying damage sensitive, environment insensitive features for damage detection. *Proceedings of the Third International Conference on Identification in Engineering Systems Swansea Wales*, 2002.

[59] Johansen S. *Likelihood-based Inference in Cointegrated Vector Autoregressive Models*. Oxford University Press, 1995.

[60] Vetterli M. and Kovacevic J. Wavelets and subband coding. *Prentice Hall*, 1995.

[61] Jaffard S., Meyer Y., and Ryan D. R. Wavelets: tools for science and technology. *SIAM*, 2001.

[62] Meyer Y. Wavelets: Algorithms and applications. *Society of Industrial and Applied Mathematics. Philadelphia*, pages 13–31, 1993.

[63] Graps A. An introduction to wavelets. *IEEE Computational Science and Engineering*, 2(2):50–61, 1995.

[64] Grossman A. and Morlet J. Decomposition of hardy functions into square integrable wavelets of constant shape. *SIAM J. Math. Anal*, 15(4):723–736, 1984.

[65] Walker S. J. *A Primer on Wavelets and Their Scientific Applications*. Chapman and Hall/CRC, Second Edition, 2008.

[66] Misiti M., Misiti Y., Oppenheim G., and Poggi J-M. *MATLAB Wavelet Toolbox 4 User's Guide*. The Mathworks, March 2008.

[67] Walker J. S. *A Primer on Wavelets and their Scientific Applications*. Chapman and Hall/CRC; 2 edition, 2008.

[68] Mathworks. *MATLAB Getting Started Guide R2011b*. September 2011.

[69] Hambaba A. and Huff A. E. Multiresolution error detection on early fatigue crack in gears. *IEEE Aerospace Conference Proceedings*, 6:367–372, 2000.

[70] Peng Z. K., He Y., Chen Z., and Chu F. Identification of the shaft orbit for rotating machines using wavelet modulus maxima. *Mechanical Systems and Signal Processing*, 16:623–635, 2002.

[71] Do N. B., Green S. R., Schwartz T. A., and Farrar R. C. Structural damage detection using the holder exponent. *2003 IMAC-XXI: Conference & Exposition on Structural Dynamics*, 2002.

[72] Yan B., Goto S., and Miyamoto A. Damage detection using the lipschitz exponent estimated by the wavelet transform: applications to vibrations modes of a beam. *International Journal of Solids and Structures*, 39(7):1803–1816, 2002.

[73] Tjirkallis A., Kyprianou A., and Vessiaris G. Structural health monitoring under varying environmental conditions using wavelets. *Key Engineering Materials*, 569-570:1218–1225, 2013.

[74] Ogaja C. and Rizos J. W. Principal component analysis of wavelet transformed gps data for deformation monitoring. *Proceedings of IAG Scientific Meeting Budapest Hungary*, 2001.

[75] Yan B., Goto S., and Miyamoto A. Time-frequency analysis based on methods for modal parameter identification of bridge structure consideration uncertainty. *Proceedings of the 2nd International Workshop on Structural Health Monitoring of Innovative Civil Structures Winnipeg Canada*, pages 453–464, 2004.

[76] Hubbard B. *The World According to Wavelets: The Story of a Mathematical Technique in the Making*. A. K. Peters / CRC Press; 2nd edition, 1998.

[77] Hamilton J. D. *Time Series Analysis*. Princeton University Press Princeton, New Jersey, 1994.

[78] Fein H. Holographic interferometry: Nondestructive tool. *The Industrial Physicist*, 3(3):37–39, 1997.

[79] Inman J. D.l. *Vibration Testing and Experimental Modal Analysis*. Engineering Vibration; 2nd edition. Prentice Hall, 2001.

[80] Stanbridge A. B. and Ewins D.J. Modal testing using a scanning laser doppler vibrometer. *Mechanical Systems and Signal Processing*, 13(2):255–270, March 1999.

[81] Marion A. *Introduction to Image Processing*. Chapman and Hall U.K., 1991.

[82] Hecht E. Theory and problems of optics: Schaums outline series. *Mc Graw Hill International*, 1975.

[83] Sonka M., Hlavac V., and Boyle R. *Image Processing Analysis and Machine Vision*. Thomson Engineering 3rd edition, 2007.

[84] Steinmetz K. Practical use of high speed cameras for research and development within the automotive industry - yesterday and today. *Processings of SPIE*, 13(Part 2):824–828, 1994.

[85] Spyrou S., Davison J. B., and Burgess I. W. Experimental and analytical studies of steel t-stubs at elevated temperatures in abnormal loading on structures: Experimental and numerical modelling. *E & FN Spon London*, pages 306–316, 2000.

[86] Canadian Photonic Labs Inc. *High Speed Catalogue*. Mega Speed, 2007.

[87] Shannon C. E. Communication in the presence of noise. *Processing of the Institute of Radio Engineers*, 37(1):10–21, 1949.

[88] Benedetto J. and Frazier M. *Wavelets: Mathematics and Applications*. CRC Press, 1994.

[89] Tang Y. Y. *Wavelet theory approach to pattern recognition*. World Scientific, 2009.

[90] Jain R., Kasturi R., and Schunck G. B. *Machine Vision*. McGraw-Hill Science/Engineering/Math 1^{st} edition, 1995.

[91] Marr D. and Hildreth E. Theory of edge detection. *Proceedings of Royal Society of London, B207*, B207:187–217, 1980.

[92] Canny J. A computational approach to edge detection. *IEEE Transactions On Pattern Analysis and Machine Intelligence*, 8(6):679–698, November 1986.

[93] Mallat S. and Zhong S. Characterization of signals from multiscale edges. *IEEE Transactions on Pattern Analysis and Machine Intelligence*, 14(7):710–732, 1992.

[94] Jain A. K. Fundamentals of digital image processing. *Prentice-Hall Inc, USA*, 1989.

[95] Guttormsen T., Andersen A., Holst J., Keilow M., and Kjhr E. Edge detection and its implementation in c++. *Aalborg, University*, 2008.

[96] Roberts L. G. Machine perception of three-dimensional solids. *In Tippett J. T. editor Optical and Electro-Optical Information Processing MIT Press Cambridge MA.*, pages 159–197, 1965.

[97] Lindeberg T. Scale-space theory: A basic tool for analysing structures at different scales. *Journal of Applied Statistics. Supplement on Advances in Applied Statistics*, 21(2):224–270, 1994.

[98] Burt P. J. and Adelson E. H. The laplacian pyramid as a compact image code. *IEEE Transactions of Communications*, COM-31(4):532–540, 1983.

[99] Mallat S. Zero-crossings of a wavelet transform. *IEEE Transactions of Informations Theory*, 37(4):1019–1033, 1991.

[100] Bovik Al. *Handbook of image and video processing*. Elsevier Academic Press, 2nd edition, 2005.

[101] Nagel H. H. Overview on image sequence analysis, nato advanced study institute on image sequence and dynamic scene analysis. *Image sequence processing and dynamic scene analysis, edition T.S. Huang, Berlin, Springer*, pages 1–39, 1983.

[102] Aggawal J. K. and Marting W. N. Dynamic scene analysis. *Image Sequence Processing and Dynamic Scene Analysis. NATO ASI Series*, 2:40–73, 1983.

[103] Walton J. S., Nalodka E. C., William R. A., Darling R. S., Fung S., and Gleason J. T. Over-the-road video-based measurement of suspension kinematics. *SAE Technical Paper Series*, 891143, 1989.

[104] Campbell J. Y., Lo A. W., and Mackinlay A. C. *The econometrics of financial markets*. Princeton University Press New Jersey, 1997.

[105] Wren T. L., Do P. K., Rethlefsen S. A., and Healy B. Cross-correlation as a method for comparing dynamic electromyography signals during gait. *Journal of Biomechanics*, 39:2714–2718, 2006.

[106] Kyprianou A. and Staszewski W. On the cross-wavelet: Interpretation and application to doffing oscillator,. *Journal of Sound and Vibration*, 228(1), 1999.

[107] Yarlagadda R. K. *Analog and Digital Signals and Systems*. Springer New York Dordrecht Heidelberg London, 2010.

[108] Yates R. D. and Goodman D. J. *Probability and Statistic Processes*. John Wiley New York, 1999.

[109] Peng Z. K., Chu F. L., and Tse W. P. Singularity analysis of the vibration signals by means of wavelet modulus maximal method. *Mechanical Systems and Signal Processing*, 21:780–794, 2005.

[110] National Instruments. *LabVIEW User Manual*. April 2003.

[111] Harvey Y. D. and Todd D. M. Cointegration as a data normalization tool for structural health monitoring applications. *Health Monitoring of Structural and Biological Systems, Processing Of SPIE*, 8348, 2012.

[112] Bruel & Kjaer. *LDS Permanent Magnets Product Data*. LDS Group, 2012.

[113] Omega Engineering Inc. *ACC 101, ACC 102, ACC103, ACC 301 Accelerometers User's Guide*. 2009.

[114] Starck J-L., Murtagh F., and Bijaoui A. *Image and Data Analysis: The Multiscale Approach*. Cambridge University Press, 1998.

[115] Tsai R. Y. A versatile camera calibration technique for high-accuracy 3d machine metrology using off-the shelf tv cameras and lenses. *IEEE Journal or Robotics and Automation*, RA-3(4):323–344, 1987.

[116] Flir Systems. *ThermaCAM Researcher User's Manual*. Flir Systems Professional edition. Version 2.8 SR-1, 2004.

[117] Arneodo A., Decoster N., and Roux S. G. A wavelet-based method for multifractal image analysis. i. methodology and test applications on isotropic and anisotropic random rough surfaces. *European Physical Journal B*, 15:567–600, 2000.

[118] Decoster N., Roux S. G., and Arneodo A. A wavelet-based method for multifractal image analysis. ii. applications to synthetic multifractal rough surfaces. *European Physical Journal B*, 15:739–764, 2000.